SURFACE DOSE ENHANCEMENT USING LOW-Z ELECTRON/PHOTON BEAMS

by

Cathryn A. M. Parsons

Submitted in partial fulfilment of the requirements
for the degree of Master of Science

at

Dalhousie University
Halifax, Nova Scotia
December 2014

DEDICATION PAGE

This thesis is dedicated to my family and friends.
Thank you for supporting me throughout this process.

TABLE OF CONTENTS

LIST OF TABLES

LIST OF FIGURES

ABSTRACT

Advances in linear accelerator technology has lead to the development of a linac which incorporates an in-air target assembly, making it possible to investigate novel treatments using multiple target designs. One such novel treatment uses multiple low-Z targets to enhance surface dose, replacing the use of synthetic tissue equivalent material (bolus). This treatment technique will decrease the common dosimetric and set up errors prevalent in using physical treatment accessories like bolus. A standard Monte Carlo model of a Varian Clinac linear accelerator was modified to incorporate a low-Z target in the electron beam. Simulations were performed using beryllium, carbon, aluminum, and copper as potential low-Z targets, in which they were placed in the secondary target position. The energies used were 2.5 and 4 MeV. The results determined carbon to be the target material of choice. Simulations of 15, 30 and 60% R_{CSDA} carbon beams were propagated through slab phantoms. The resulting PDDs were weighted and combined with a standard 6 MV treatment beam to assess feasibility of surface dose enhancement. Using combinations of 15, 30, 60% R_{CSDA} beams operated at 2.5 and 4 MeV in combination with a standard 6 MV treatment beam the surface dose was shown to be enhanced to within 80-100% the dose at d_{max}. Physical versions of the experimental targets were installed into a 2100C Varian Clinac (Varian Medical Systems Inc., Palo Alto, CA). The bending magnet shunt current was adjusted with the 4 MeV scattering foil in the beam-line, allowing mean energy selections of 2.5 and 4 MeV with the 2100C. Electron energy was determined through comparison of Monte Carlo modeled depth dose curves with experimentally measured data. The modeled low-Z beams were successfully validated using machined versions of the targets. Water phantom measurements and slab phantom simulations show excellent correlation to within 5%. This study presents a viable option for surface dose enhancement without the use of an external modifier.

LIST OF ABBREVIATIONS USED

AEIT	Approximate efficiency improving technique
Al	Aluminum
BMAG	Bending magnet
Be	Beryllium
C	Carbon
CM	Component module
CPE	Charged particle equilibrium
Cu	Copper
CSDA	Continuously slowing down approximation
CT	Computed tomography
DICOM	Digital imaging and communications in medicine
D_{max}	Maximum dose
d_{max}	Depth of maximum dose
ECUT	Electron transport cut-off energy
EFD	Electron field diodes
EGS	Electron gamma shower
EPID	Electronic portal imaging device
HU	Hounsfield units
HV	High voltage
keV	Kiloelectron volt

kV	Kilovolt
Linac	linear accelerator
MC	Monte Carlo
MeV	Megaelectron volt
MLC	Multileaf collimator
MU	Monitor unit
MV	Megavoltage
NIST	National Institute of Standards and Technology
NRC	National Research Council of Canada
NSCC	Nova Scotia Cancer Center
OAR	Organ at risk
PCUT	Photon transport cut-off energy
PDD	Percent depth dose
PFNV	Pulse forming network voltage
R_{50}	Depth of 50% PDD
R_{90}	Depth of 90% PDD
R_{CSDA}	Continuously slowing down approximation range
RF	Radiofrequency
R_{max}	Maximum range
RNG	Random number generator
R_p	Practical range
SBS	Selective bremsstrahlung splitting

SSD	Source-to-surface distance
TLD	Thermoluminescent dosimeter
W	Tungsten
Z	Atomic number

ACKNOWLEDGEMENTS

The completion of this work would not have been possible without the guidance and understanding of my supervisor, Dr. Robin G. Kelly. I would like to extend to him my sincerest thanks and admiration. I am grateful for your patience, caring, and support over the last few years.

I would like to thank David Parsons and Dr. James L. Robar for sharing their knowledge of low-Z targets and Monte Carlo simulations with me. Your expertise was vital to the success of this project. Thank you to Dave, especially, since I'm sure I annoyed him with all my questions, that's what little sisters are for after all.

Thank you to David Pepper who spent countless hours with me during the experimental phase of this work. Even though the C fought back, we were able to get exceptional results, which would not have been easy without you.

Other important contributors to this work are Ian Porter, who fabricated the target holders used, and Machining Solutions Inc. in Ontario, who machined our carbon targets. You have my utmost thanks.

Thank you to all the medical physicists and dosimetrists at the NSCC who've shared their knowledge with me and made this a wonderful experience. I would also like to thank my friends, especially Jess and Maria, who've given me support when I've needed it the most.

Lastly, but certainly not least, I would like to thank my parents, for always encouraging me to follow my heart and go after what I want.

CHAPTER 1 INTRODUCTION

1.1 DEMOGRAPHICS OF CANCER IN CANADA

Cancer is a debilitating disease marked by uncontrolled abnormal cell growth with the ability to infiltrate and disrupt normal tissue. In 2014, the annual statistics released by The Canadian Cancer Society estimated that 191 300 new cases of cancer will be diagnosed in Canada, which will result in 76 600 cancer mortalities[1]. In Canada, cancer is the leading cause of death at 30%, even greater than mortalities due to heart disease, which currently accounts for 20% of all deaths in Canada[1]. In particular, Nova Scotia has one of the highest new incidence estimates per capita in 2014 (see Figure 1.1). According to the statistics, geographic variation in incidence rates may be due to differences in risk factors such as unhealthy diet, smoking, obesity, and physical inactivity, as well as different provincial/territorial programs or procedures for diagnosis and early detection of cancer. Breast cancer incidence rose in the 1990s due to increased mammography screening.

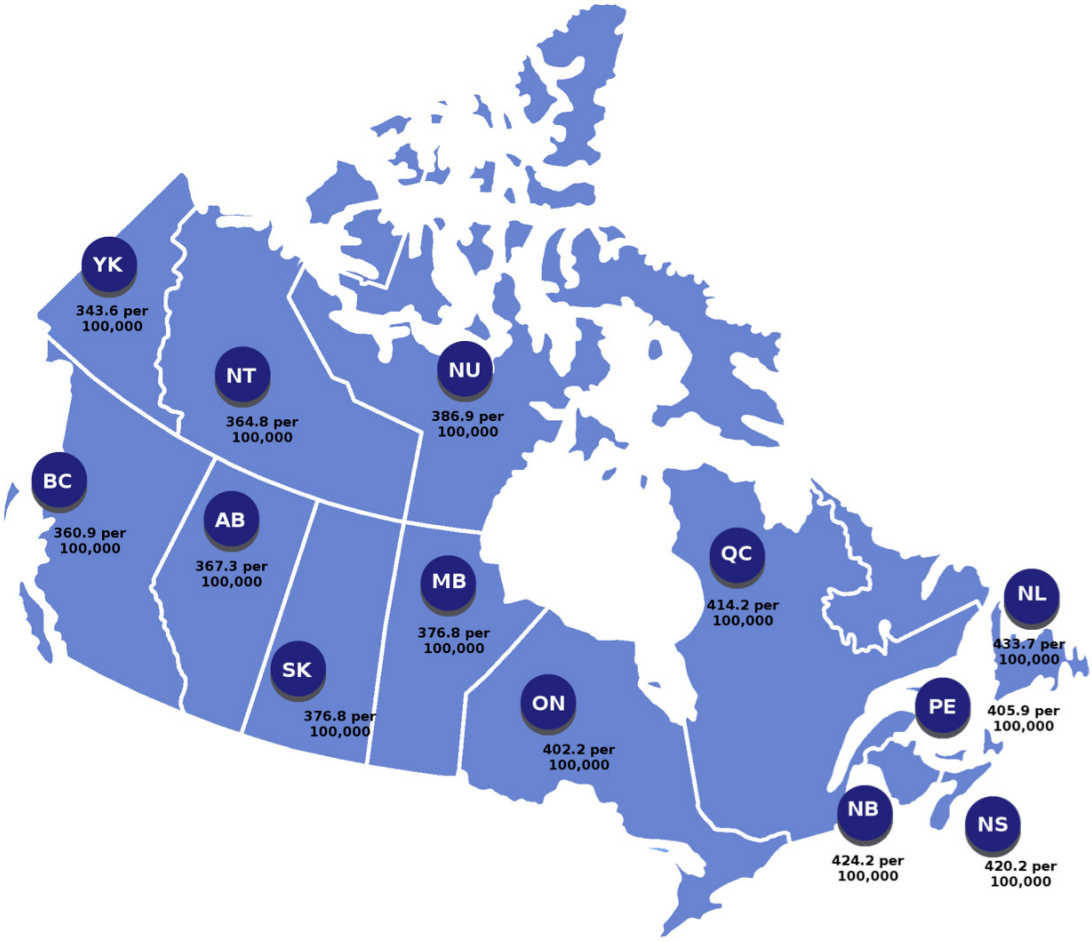

Figure 1.1: Estimated new cases and incidence rates across Canada. Adapted from the Canadian Cancer Society 2014 Statistics[1].

1.2 Breast Cancer Treatment

In Nova Scotia breast cancer is the most prevalent type of cancer for women (25.3% of new cases). Breast cancer is typically treated using surgery, radiation therapy, chemotherapy, or some combination there of. The treatment chosen depends on the extent of the disease and its histology. Breast cancer patients typically receive radiation therapy after lumpectomy or mastectomy (partial or total removal of the breast tissue).

Breast cancer is a very aggressive disease, 80% of patients recur within 5 years[2], thus treatment has to be aggressive as well. Radiation therapy uses ionizing radiation to deliver a predetermined dose to a defined target volume, while limiting the dose to the surrounding healthy tissue. Radiation therapy helps to decrease loco-regional recurrence and late complications by eradicating residual microscopic cancerous cells from the original site and lymph nodes. Recurrence is likely to occur in the same quadrant as the original tumour (80%)[2], therefore sufficient coverage of this region is essential.

1.2.1 Post-mastectomy Treatment & Surface Dose Consideration

In advanced cases (T3/T4 tumours, four or more lymph nodes involved), post-mastectomy radiation therapy is very important for loco-regional control as these patients in particular are at a high risk of recurrence[2, 3]. In these cases, both the chest wall and supraclavicular nodes are treated in either 16 or 25 fractions (4240 or 5000 cGy for chest wall, 4000 or 4500 for the supraclavicular nodes, respectively) using 6 MV beams.

The chest wall requires 95% dose coverage to 95% of the planning target volume (PTV), while organs-at-risk (OARs), including heart, lungs, liver, and contralateral breast, must be shielded while achieving this goal. Moderate to high doses (60 – 40 Gy) to large volumes of the heart (30 – 100%) increases the risk of pericarditis and radiation induced ischemic heart disease[4]. The PTV for chest wall patients includes the topmost layer of the patient's tissue, as microscopic abnormal cells are likely to remain in this tissue after surgery (Figure 1.2).

1.3 Surface Dose Enhancement Techniques

Since 6 MV beams require 1.5 cm of absorbing material before maximum dose is reached, a tissue equivalent material (commonly referred to as Bolus) is placed on the patient for half of the 16 or 25 fractions to ensure adequate skin dose coverage

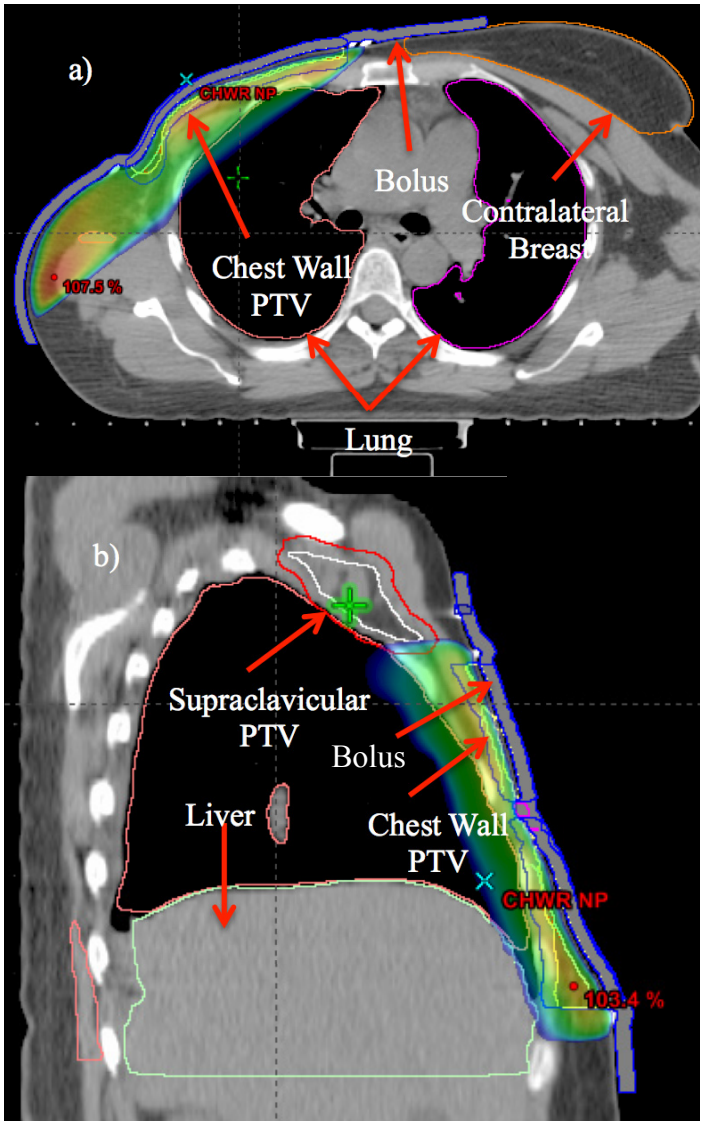

Figure 1.2: Isodose map of chest wall patient. a) Axial view showing chest wall PTV, bolus (superficial blue covering), lung (pink and purple), and contralateral breast (orange). b) Sagittal view showing isodose covering of chest wall PTV, bolus (superficial blue covering), lung (pink), liver (green), and supraclavicular PTV (red).

(see Figure 1.3). Electron beams may also be used to increase surface dose, although techniques that do not require daily imaging, such as an *enface* technique, there is an increased risk of geographic miss of the tumour or excessive lung/heart irradiation[2]. Bolus is still used in these cases.

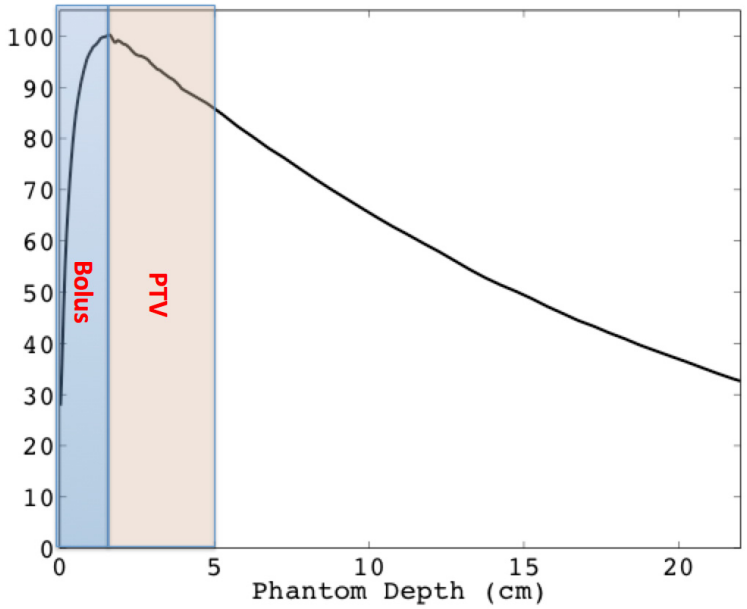

Figure 1.3: Percent depth dose curve of 6 MV radiation beam. PTV location is denoted by beige rectangle, where 95-100% dose is required. Build up of dose occurs within bolus material (blue rectangle) to achieve chest wall PTV requirements.

The skin-sparing property of megavoltage radiotherapy is a noted advantage for treatment of deep-seated tumours, though not ideal for treating superficial regions in breast chest wall patients. Dose enhancement at the patient's surface is achieved using several techniques developed over time, such as, use of a scattering layer to substitute as the skin surface.

Surface dose is mainly due to electron contamination from the flattening filter, secondary collimation, beam modifiers, air, and secondary electrons created as the

primary beam passes through the patient. The last component is strictly dependent on beam energy, beam angle, field size, source-to-surface distance (SSD), and absorbing media. Increasing the beam energy and decreasing the field size can decrease the surface dose. Whereas, increasing the surface dose can be achieved through the following methods: electron beams, beam spoilers, brass mesh, and various types of tissue equivalent bolus materials. Each of these methods are discussed below

Electron beams have a finite range in tissue, allowing delivery of the desired dose to the target volume and a high surface dose, while sparing distal organs. However, electron beams present a challenge as they may contribute to unnecessary healthy tissue dose: junction regions present dosimetric hot and cold spots; surgical defects lead to dose heterogeneity[5].

Beam spoilers are used to enhance surface dose by increasing the number of secondary electrons that are incident on the patient, and by shifting the position of D_{max} towards the surface. Spoilers are typically sheets of low atomic number material, whose thickness is dependent on the beam energy and the desired shift in d_{max}, placed a specified distance from the patient surface. As the beam passes through the spoiler, medium energy secondary electrons are created causing an increase of the scatter component of electrons and photons[6]. The advantage of beam spoilers is their ability to increase dose at the surface and shallow depths while maintaining skin sparing due to the displacement from the patient[6]. Spoilers are typically used to supplement the surface dose from higher energy photon beams[7]. Using a spoiler, the surface dose can be increased by 10% and 15% for a 10 MV and 18 MV beam, respectively[8]. However,

when used to treat breast cancer patients, the dose received by the contralateral breast increased dramatically, up to 15% of the prescribed dose in one study[8] and increased the max dose to over 100% in another[9].

High-Z, mesh bolus, such as brass, placed on the patient effectively enhances surface dose. A high component of low energy electrons are produced within the mesh and deposit dose superficially. The mesh has a high conformity to the patient's surface and does not significantly add to dose at depth[10]. This enables a single plan to be made rather one accounting for no modifier and another with modifier. While presenting an effective method of surface dose enhancement, there is a risk of neutron activation within the mesh when using high-energy photon beams. This may increase the skin dose to the patient, as well as to the hands of the therapist handling the bolus[11]. Mesh was found not to be comparable to tissue-equivalent bolus in the treatment of superficial disease. The mesh under dosed the first 5 mm of depth, and is therefore not suitable to treat microscopic disease in the initial millimeters of skin[12].

The conventional method for surface dose enhancement is to add a layer of tissue equivalent bolus material whose thickness will vary based upon the energy of the beam. Bolus material used in a clinical environment must be tissue equivalent, non-toxic, flexible enough to conform to surface contours of patients, easily manufactured/produced, durable, cost effective, and can provide adequate homogeneous dose delivery to the target volume[13, 14]. There are many forms of bolus commercially and locally available. Typical forms of bolus include wet gauze, paraffin and beeswax, Aquaplast (WFR-Aquaplast and Qfix Systems, Avondale, PA), and

Superflab (Eckert & Ziegler BEBIG, Seneffe, Belgium). Bolus, unlike mesh, can significantly increase the superficial surface dose, in some cases from 44 – 80%[15]. Bolus effectively enhances surface dose by mimicking the patient's tissue, causing the build-up region to occur within the synthetic material and thus shifting the point of maximum dose build-up towards the surface of the patient. Bolus was used as early as the 1920s[14], and is commonly used in the treatment of head and neck as well as breast cancers.

Water has been used as a bolus material; however, it is not practical or comfortable for all applications as it is difficult to contain in a specified shape[14]. As an alternative to water, wet gauze is commonly used, however, research has found that the level of water saturation, and hence the physical density, is hard to regulate resulting in errors in the planned dose delivered to the patient. The required level of precision is challenging to reproduce in a clinical setting and may not be time efficient. Paraffin and beeswax are traditional bolus materials that can be moulded into any shape needed. For wax to be malleable, it must be at high temperatures, making it unable to be moulded directly on the patient. Wax bolus must be poured into a plaster mould of the patient contour[14], this requires time and must be done each time the patient contour changes throughout treatment. Commercial product such as Jeltrate Plus (DENTSPLY, Mount Waverley, Australia) improve upon the use of wax as a bolus material[14].

Aquaplast (WFR-Aquaplast and Qfix Systems, Avondale, PA) is a solid material that becomes mouldable after submersion in hot water. It is typically used to make immobilization masks, though it also takes on the properties of a bolus material as dose

will build-up within the mask, thereby increasing surface dose[16]. Other bolus materials can be fused with the mask to enhance the effect[14]. Another commonly used bolus is Superflab (Eckert & Ziegler BEBIG, Seneffe, Belgium), a soft synthetic gel sheet with a specific density of 1.02 g/cm^3 (water is 1.0 g/cm^3)[14]. Superflab offers convenience as it can be washed and does not dry out, making it suitable for reuse. Being malleable, it conforms relatively well to patient contours. All bolus types discussed above have pros and cons; the choice of bolus material is very dependent on the situation and location of radiation delivery.

1.4 Clinical Problems with Current Surface Dose Enhancement

All forms of bolus require placement of an external physical moderator on the patient's surface. By introducing an external moderator into treatment, the risk due to human error is increased.

The treatment planning system cannot accurately model the bolus material at the interface between the patient's skin and the bolus itself. There are several reasons for this; however, the main issue is the existence of air gaps between the patient's anatomy and the bolus material. Research has shown that relative dose distribution at the surface changed dramatically as the air gap between the bolus and patient surface is increased, especially when involving small fields[17, 18] (Figure 1.4). Introducing an air gap between two like media affects the build up of backscattered electrons. Air has a lower atomic number than tissue, and tissue equivalent material, thus as the interface between bolus and the air gap is approached, the component of backscattered

electrons decreases until it decays to zero at the interface since negligible backscattering is contributed by air. The component of forward moving electrons generated in the bolus begins to decay beyond the interface, and new electrons are generated by photon interactions in air. Thus, gaps result reduction in dose at the surface, which cannot be predicted or accounted for during the treatment planning process.

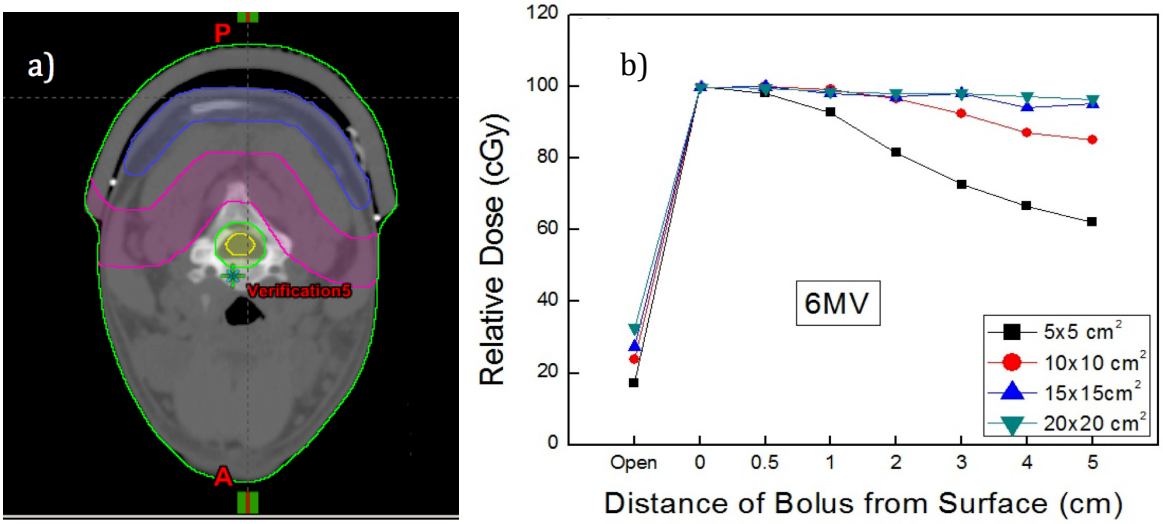

Figure 1.4: A) CT scan of patient and applied bolus, showing a significant air gap. B) Relative surface dose for a 5 x 5 cm^2, 10 x 10 cm^2, 15 x 15 cm^2, and 20 x 20 cm^2 6 MV beam, showing the effect on surface dose as air gap is increased. Adapted from Khan *et al.* 2013[19].

Beyond the planning and delivery errors caused and the presence of air gaps, bolus is an add-on material, which must be placed by the radiation therapist prior to each treatment fraction. This act alone increases the probability of human error. A recent study by the Radiotherapy Incident and Safety Committee in Ontario took a census of all errors/incidents recorded within cancer centers in 2011/12[20]. The breakdown of the reported incidents is shown in Figure 1.5. Among the reported

incidents, 18% were caused by the addition of treatment accessories. Of that 18%, almost half (48%) were due to the misuse and misplacement of bolus. The majority of these incidents involved a dose deviation of less than 5% of the prescription dose, which was avoidable if properly used.

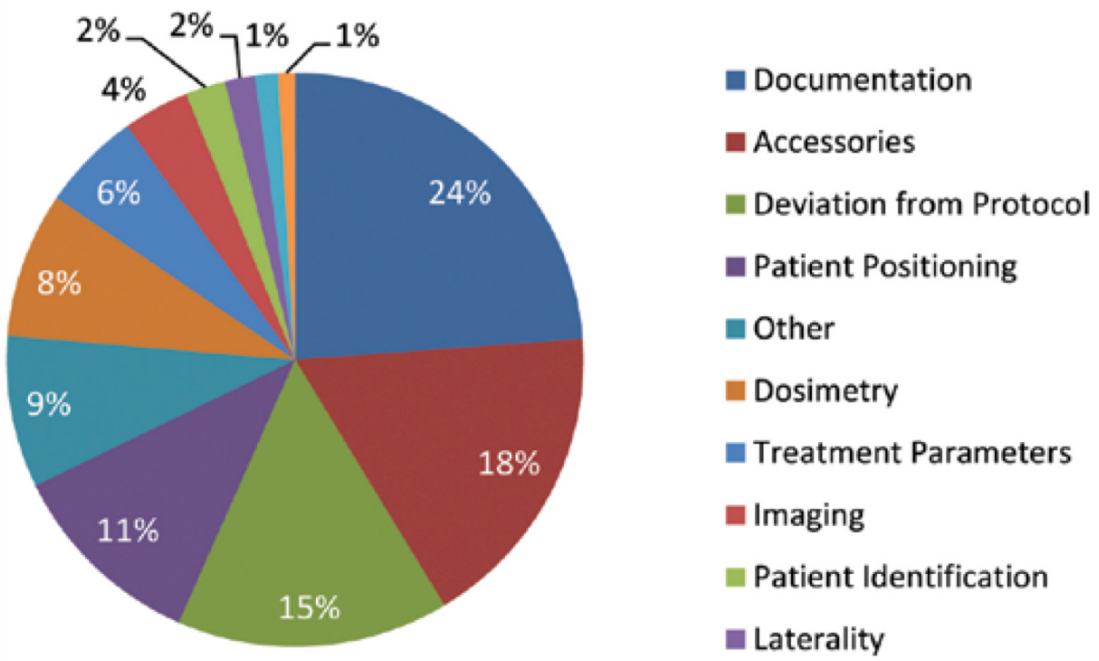

Figure 1.5: Chart showing the distribution of reported radiation incidents in Ontario cancer centers in 2011/12. Adapted from Clarke, B.G. 2013[20].

Once an external accessory, such as bolus, is added to a patient's plan there is potential for avoidable dosimetric errors to occur such as those described above. This work developed based on the elimination of external accessories for surface dose enhancement (and unnecessary incidents), through the use of the linac and treatment planning software alone.

1.5 Surface Dose Enhancement using Low-Z Targets

The goal of this research was to develop a method to enhance surface dose without the use of add-on materials, and instead use low atomic number targets and low energy beams with a linear accelerator to enhance surface dose.

Prior research involving low-Z targets focused on their use with contrast-enhanced radiation therapy (CERT). This involved administering high-Z contrast media (iodine, Z = 53, or gadolinium, Z = 64) that would accumulate in the tumour, increasing its effective atomic number. By increasing the tumour's atomic number, dose absorption could be selectively augmented through increasing the photon interaction cross section because of the Z-dependence of the photoelectric effect (Z^4 to $Z^{4.8}$ dependence)[21]. This has traditionally been done using photon beams within the superficial or orthovoltage energy range[21]. However, studies have previously determined a method of using linear accelerators for CERT by removing the flattening filter[22]. To use a linac for CERT the low energy photons must be preserved in the beam, since low energy photons that interact through the photoelectric effect, the high-Z flattening filter would effectively remove them from the beam. By removing this component, CERT could be explored using a linac. This earlier study discovered that dose enhancement could be increased from 8.4% to 23.1% by using a 2 MV beam rather than 18 MV[22]. Further enhancement was seen using aluminum and beryllium targets (60% CSDA thickness) and a polystyrene filter (see Figure 1.6), as a result of the increased lower energy photon population. The thinner target caused an increase in the

contaminant electron population; the polystyrene filter removed the electron component without affecting the photon beam, as it is a low-Z material.

.

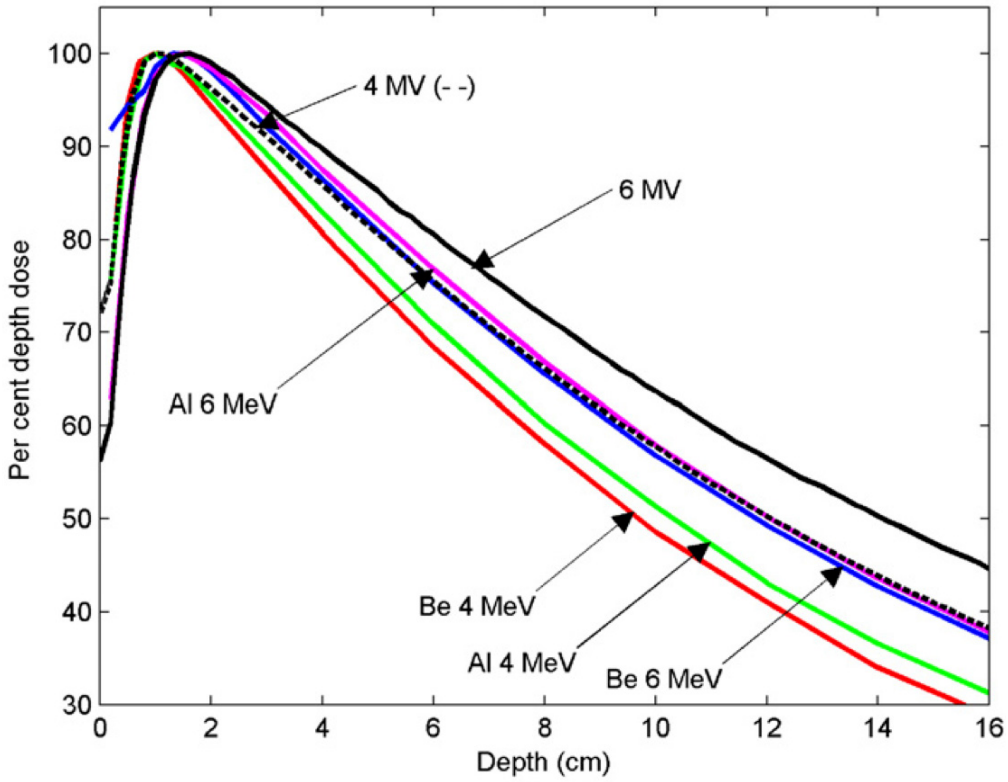

Figure 1.6: A) measured PDD curves for low-Z CERT beams compared to nominal 4 and 6 MV beams. Modified from Robar, 2006[21]. Used with permission.

With the polystyrene filter removed the electron contamination component was collected during measurement, producing intriguing results. The electron contamination component within the beam showed an initial spike in the dose distribution observed in the first 1 – 1.5 cm of depth (see Figure 1.7), indicating that the mean energy of the electrons within the beam was ≃2 MeV. After the initial spike, dose drastically decreases to 10% of D_{max} for the Be curves, and 40 to 50% of D_{max} for Al. These results indicate a high concentration of low energy electrons, which deposit their energy superficially. This

is especially true of the Be depth dose, since the electron dose falloff occurred within the first centimeter. These beams are ideal candidates to use for surface dose enhancement, as they will not significantly contribute to dose beyond the first centimeter.

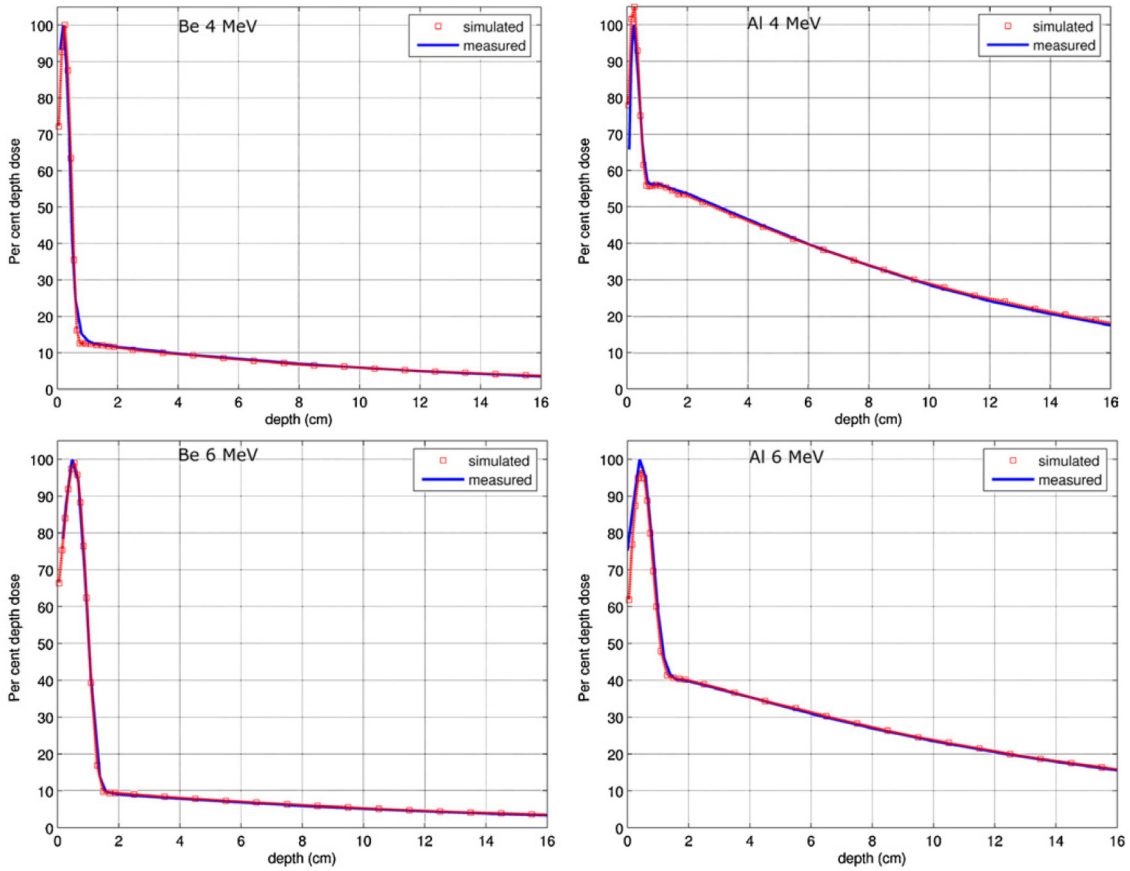

Figure 1.7: Four CERT beams collect without polystyrene electron filter in Robar, 2006. Used with permission.

In 2009, a paper on low-Z targets used to improve image contrast was published on research from Dalhousie University. The aim of the first paper was to quantify the effects on MV image contrast by using low-Z targets and an EPID, accomplished using both MC simulation and experimental measurement[23]. The research focused around beryllium (Be, Z=4) and aluminum (Al, Z=13) targets with energies of 6 and 4 MeV. It was

shown that the population of 25 – 150 keV photons increased with decreasing maximum energy, thereby improving contrast by a factor ranging from 1.6 ± 0.1 to 2.8 ± 0.2, and very low energies (<25 keV) contribute more to patient dose rather than image contrast[23]. The spectra for Be showed the bulk of the photon spectra being <30 keV[23].

The idea of using low-Z beams for therapy followed the release of the new TrueBeam (Varian Medical Systems Inc., Palo Alto, CA) linear accelerator platform by Varian Medical Systems. Previous linear accelerators housed the target under vacuum, and were equipped with only two photon targets, 6 and 18 MV being the most common (typical energies offered range from 4 – 22 MV). The TrueBeam platform features an accessible in-air target and variable target arm housing five target positions (see Figure 1.8). The fifth target position is a low-Z target intended for imaging use, and was released in TrueBeam 2.0. These developments opened the possibility of developing a low-Z target for the purpose of enhancing surface dose, since the target could be easily accessible, and with the variable target arm, new non-cylindrical target designs could be considered for the first time.

Some of the previous groundwork that was performed for imaging must be repeated with the focus instead on therapeutic uses. No prior research focused on the use of low-Z targets to specifically enhance surface dose, thus a selection of target materials, thicknesses and incident energies must be investigated to determine the optimal target composition to further this idea toward clinical use.

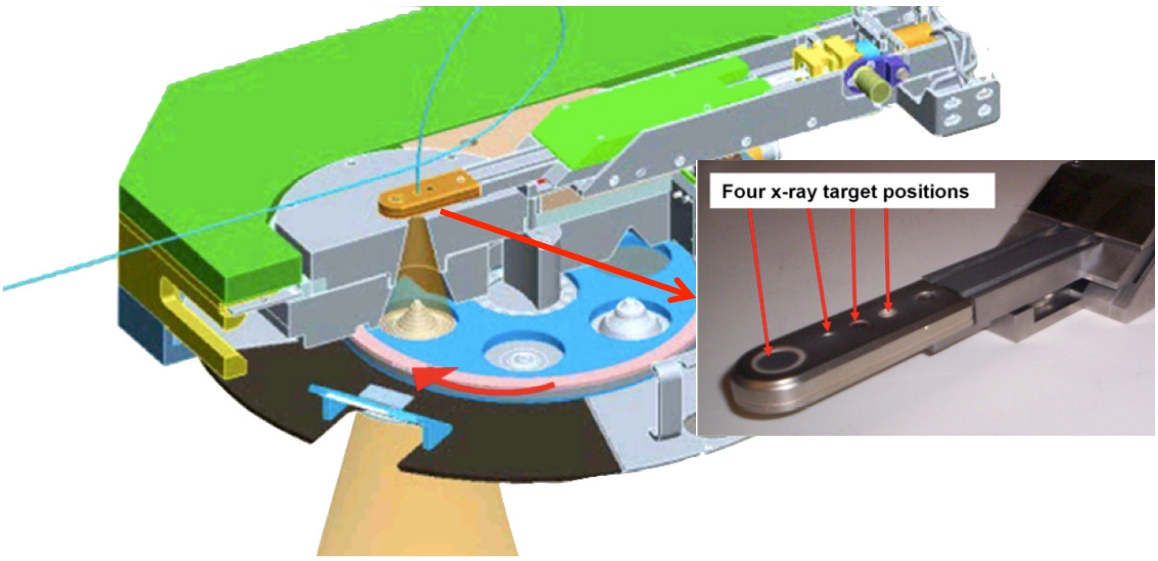

Figure 1.8: Diagram showing the in air target assembly of Varian TrueBeam (Varian Medical Systems Inc., Palo Alto, CA) machine. The target arm is featured in the inset and shows the four possible target positions. Adapted from the TrueBeam manual[24].

The project was designed to investigate low energy beam characteristics of four low-Z elements: beryllium (Be, Z = 4), carbon (C, Z = 6), Aluminum (Al, Z = 13), and Copper (Cu, Z = 29). These elements were decided upon based on a literature review of relevant publications, which centered on the use of low-Z targets for portal imaging techniques. Low-Z targets, in conjunction with a lower energy electron beam, increases the low energy photon population and thus improves image contrast – a much-desired aspect in portal imaging[23, 25–27]. Publication of photon spectra was the focus of the literature review, as this would be used to choose our target elements. In 1998, Tsechanski *et al.* and Ostapiak *et al.* published low-Z spectra with promising results featuring Be, C, Al, Cu, and Titanium (Ti). Since the goal of the project was to investigate the practicality of a mixed composition target, with a sloped or step function design, various materials with unique spectral peaks in the low-energy region were desired. The novel target arm design in TrueBeam may allow fine control of its position, thus a sloped

or step function target design would allow a variable thickness target that could be used to tailor patient plans. From Figure 1.9 it can be seen that Be and C have prominent peaks with the lowest energy; with respect to dose deposition these elements would encourage a high degree of very superficial dose, followed by Al, Ti, and Cu.

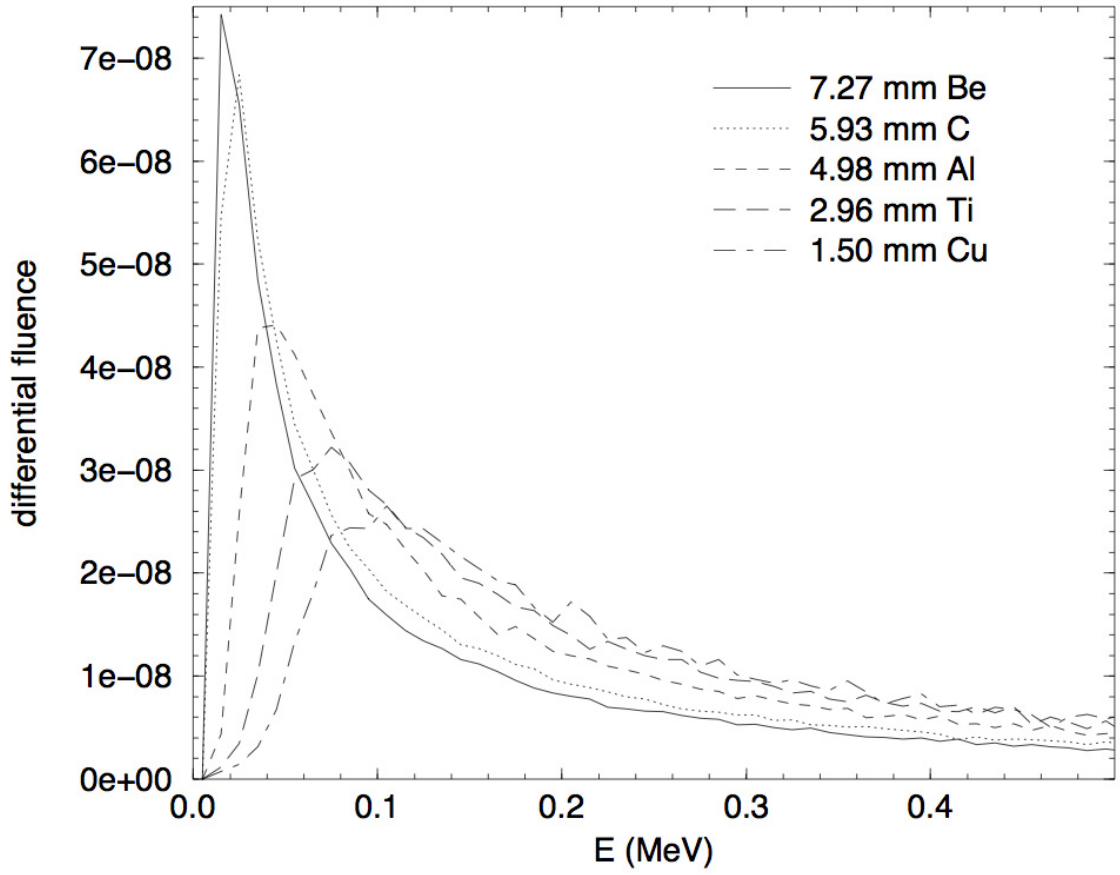

Figure 1.9: Photon fluence at isocenter versus energy as presented in Tsechanski et al. (1998). This represents the low energy spectrum of interest for various materials. Each target thickness reflects 'mass-equivalency' to 1.50 mm of Cu.

Publications by Orton and Robar (2009), and Parsons and Robar (2012), were vital in choosing the beam energies to be used throughout the research, which were 4 MeV and 2.5 MeV (see Figure 1.10 and Figure 1.11). The former was chosen as it is a standard energy available on most clinical machines in operation today, and the latter

was chosen since it was close to the lowest stable energy achieved in previous research done at Dalhousie University[27]. Orton and Robar (2009) showed a comparison of Be and Al at 4 and 6 MeV, which highlights the effect of incident electron energy on low energy photon fluence (see Figure 1.10). Another point of note in Figure 1.10 is the inclusion of the spectra of a therapeutic 6 MeV beam.

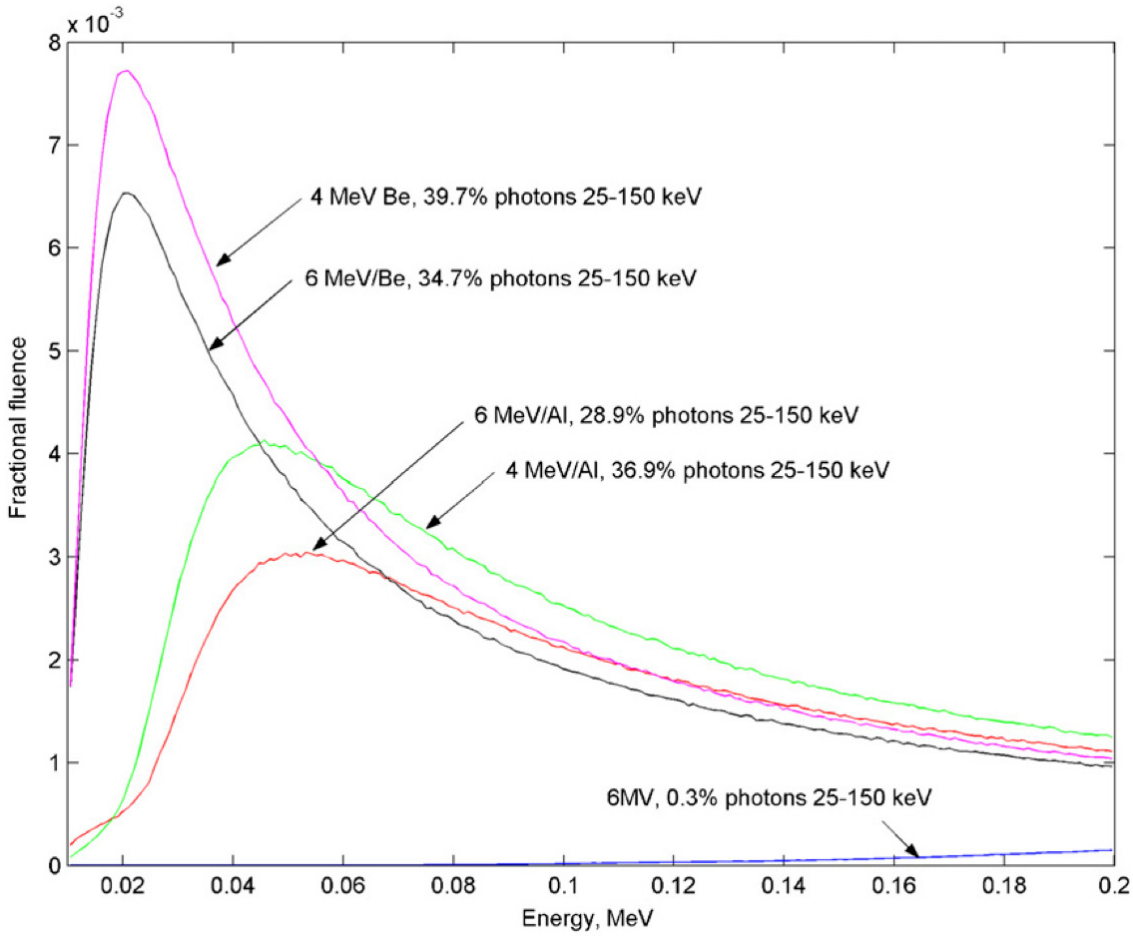

Figure 1.10: Calculated photon fluence versus energy for 6 MV therapy beam, 6 & 4 MeV Al, and 6 & 4 MeV Be as presented in Orton and Robar (2009). The beam was scored upon exit of the accelerator head.

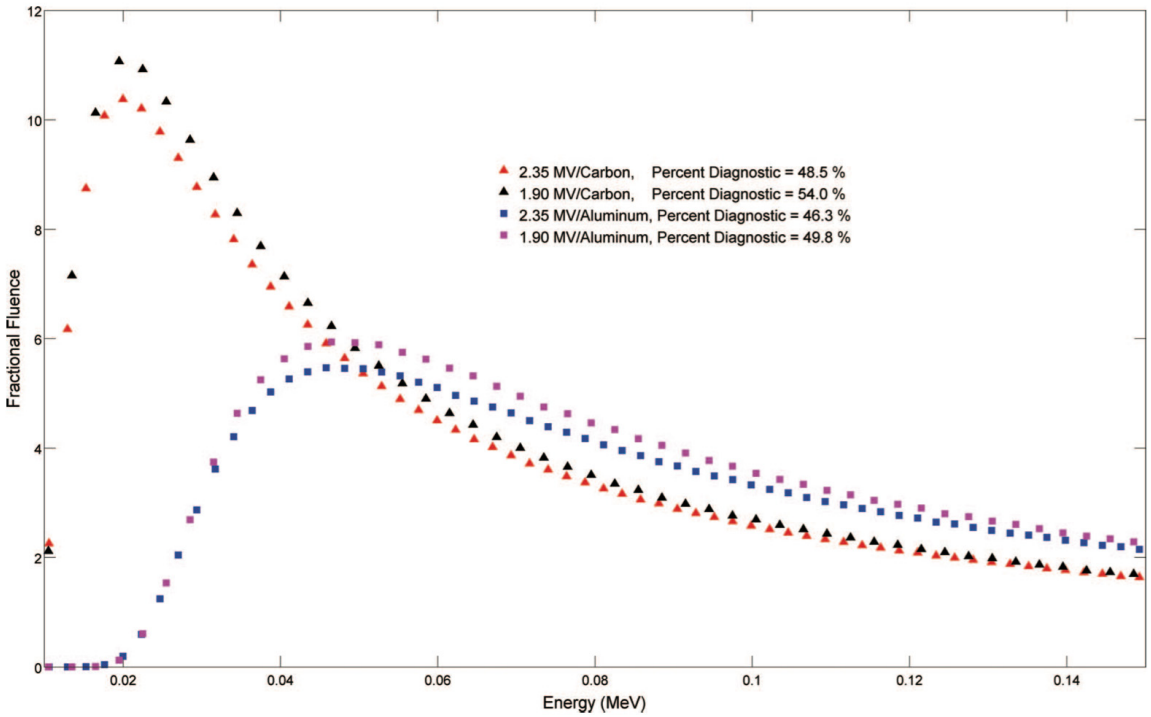

Figure 1.11: Calculated photon fluence versus energy for 2.35 & 1.90 MV C, and 2.35 & 1.90 MV Al, as shown in Parsons and Robar (2012). Only the low energy (diagnostic) range is displayed.

The literature review led to the design of the project. Materials selected were Be, C, Al, and Cu; the thicknesses of each target were 15, 30, and 60% CSDA range; and the incident energies investigated were 2.5 and 4 MeV. The goals of the research contained herein will be to determine: (i) the optimal composition of the low-Z target that will effectively increase surface dose, (ii) how target thickness affects the percent depth dose curves of the generated beams, and (iii) whether combinations of various low-Z beams are capable of producing a uniform dose distribution at the surface when used in conjunction with a standard 6 MV therapeutic beam. The last goal will focus on using the target composition determined in (i) and the PDDs determined in (ii) for the varying target thicknesses.

CHAPTER 2 RADIOLOGICAL PHYSICS, RADIATION BEAM GENERATION & DETECTION

To understand the procedures and undertakings in this work, a background in the physical concepts of radiological physics, beam generation, and detection are presented within herein.

2.1 Charge Particle Interactions with Matter

Charged particles, such as electrons, are surrounded by a Coulomb electric force field, hence, will interact with any charged particle they come into proximity with, including other electrons and the nucleus of atoms. These interactions typically only involve transfers of small portions of the electron's initial kinetic energy (for the case of an electron interacting with an atom at a distance). This is often described by the "continually slowing down approximation" (CSDA) where the charged particle is assumed to lose its kinetic energy in a gradual process similar to how a block sliding across the floor will lose its kinetic energy to the force of friction. The interactions are classified by the size of the classical impact parameter, b (the distance between the path of a particle and the center of the field with which it interacts), in relation to the atomic radius, a. Three interaction types are dominant for $b >> a$, $b \sim a$, and $b << a$ respectively[28].

2.1.1 Soft Collisions (*b* >> *a*)

These collisions occur when an electron passes an atom at a substantial distance (Figure 2.1). The interaction is initiated by the electric field of the electron, which distorts the electric field of the atom as a whole, exciting the atom to a higher energy level. Sometimes the atom may be ionized, which results in ejection of a valence electron. The overall energy transferred to the atom is on the order of a few eV. Due to the likelihood of large distances (*b*) between the incoming charged particle and atoms within the absorbing medium, these interactions are the most probable type of interaction. Soft collisions account for approximately half of the energy transferred to the absorbing medium[28, 29].

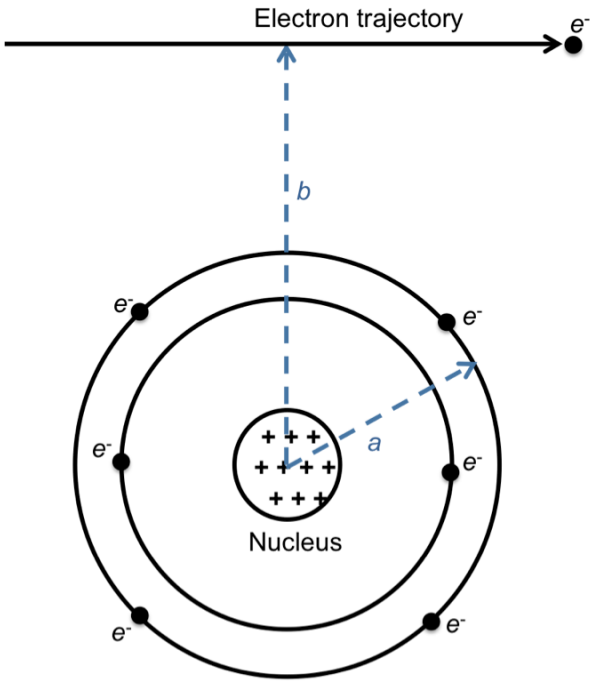

Figure 2.1: Diagram showing conditions for soft collisions, where *a* is the atomic radius, *b* is the impact parameter and e^- is an electron.

2.1.2 Hard Collisions ($b \sim a$)

Hard collisions occur when the impact parameter, *b,* is on the same order as the atomic radius, *a* (Figure 2.2). With these collisions it is likely that the incident electron will interact with a single atomic electron. The atomic electron is ejected from the atom with significant kinetic energy, and is referred to as a delta (δ) ray. As the δ-ray is also a charged particle it will deposit kinetic energy along a separate path from the primary charged particle, called a spur. These collisions occur less frequently than soft collisions, but the fraction of the incident particle's initial energy transferred in hard collisions is comparable to that transferred in soft collisions. If the incident electron strikes an inner shell electron causing it to be ejected, characteristic x-rays and/or Auger electrons will be emitted. These particles will be discussed in the next section.

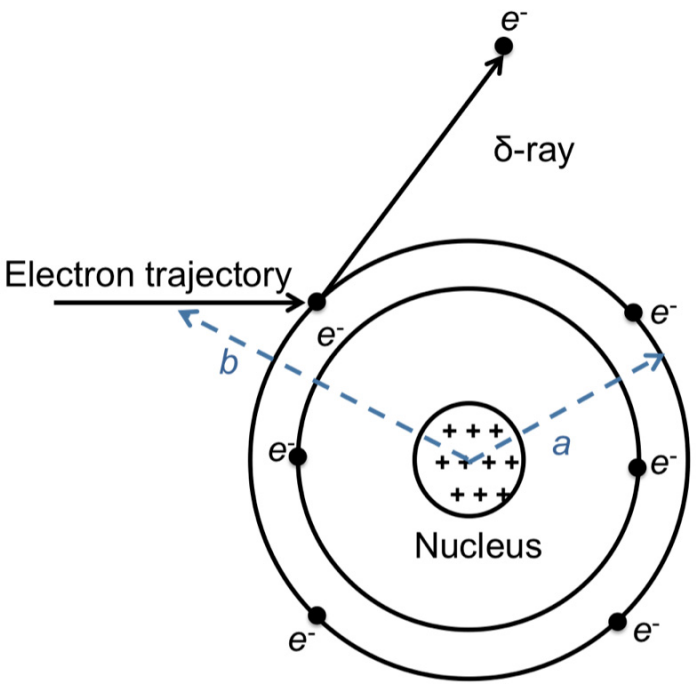

Figure 2.2: Diagram showing conditions for hard collisions, where *a* is the atomic radius, *b* is the impact parameter, and e^- is an electron.

2.1.3 Radiative Collisions ($b << a$)

These collisions take place when the impact parameter is considerably smaller than the atomic radius. This allows the Coulomb-force field to interact directly with the electric field of the nucleus (Figure 2.3). In the majority of these interactions (98 – 97 %) the electron scatters elastically, not emitting an x-ray, nor exciting the nucleus. While not a means to transfer energy within the absorbing media (only a small amount of kinetic energy is lost to conserve momentum), this collision type serves to deflect the electron. This is one of the reasons electrons do not follow a straight path within an absorbing media. The elastic scattering cross-section per atom is proportional to Z^2, thus higher-Z materials efficiently scatter electron beams.[28] Hence the use of thin foils of high-Z material to construct scattering foils.

In the remaining 2 – 3 % of these collisions, an inelastic radiative interaction transpires through which an x-ray is emitted. The electron is still deflected, but in the process can transfer up to 100 % of its kinetic energy to the emitted photon, causing the electron to slow down in the process. These photons are known as bremsstrahlung photons, which is German for 'braking radiation'. The atomic cross section for this interaction is proportional to Z^2, and depends on the inverse square of the mass of the colliding particle for a given velocity; thus, this interaction is only significant for electrons and positrons. In low-Z materials, bremsstrahlung production is insignificant for energetic electrons below 10 MeV.[28]

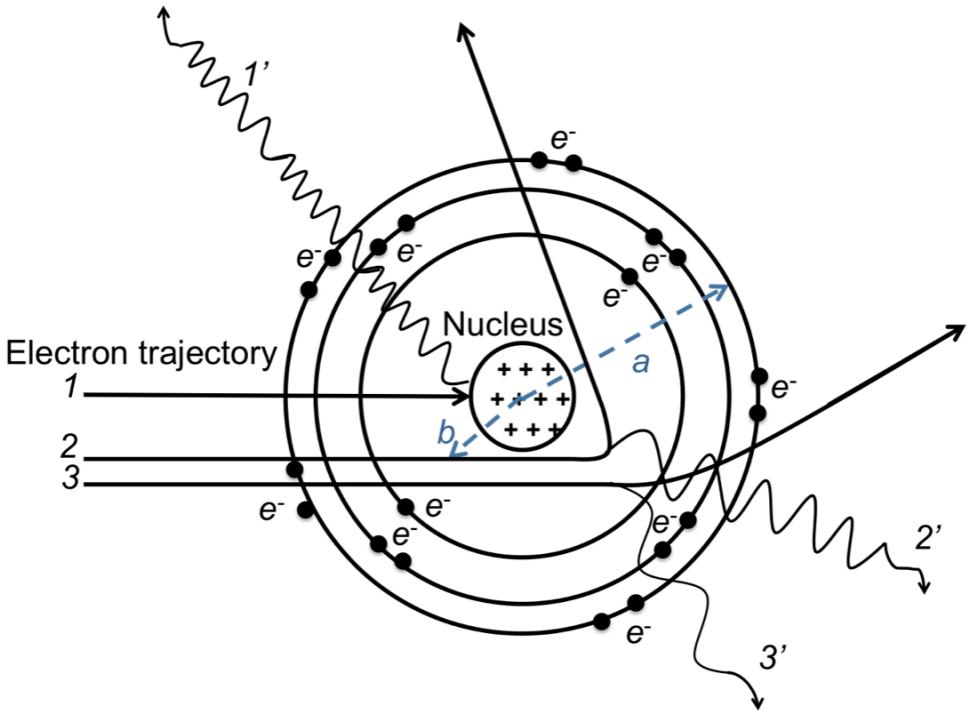

Figure 2.3: Diagram showing possible outcomes of inelastic radiative interactions with the nuclear field, where *a* is the atomic radius, *b* is the impact parameter, and e^- is an electron. In 1) the electron transfers all of its kinetic energy to the photon (1') as it collided with the nucleus. In 2) the electron trajectory was between the nucleus and the inner most shell causing it to scatter at a large angle as well as transferring a significant portion of kinetic energy to the x-ray (2'). In 3) the electron passes near the edge of the nuclear field, bending the trajectory and losing a small amount of kinetic energy to the radiated photon (3').

2.1.4 Stopping Power

Stopping power is the kinetic energy loss by an electron per unit length x, and represents the inelastic energy losses of an electron passing through a medium of density ρ.

$$(S/\rho)_{total} = \frac{1}{\rho}\frac{dE_K}{dx}\ (MeV \cdot \frac{cm^2}{g}) \tag{2.1}$$

Where E_K is the kinetic energy of the electron and S/ρ is the stopping power. The mass stopping power is subdivided into collisional and radiative stopping powers, which

allows for the determination of the portion of the charged particle's energy lost in hard and soft collision events versus radiative events (bremsstrahlung):

$$(S/\rho)_{total} = (S/\rho)_{col} + (S/\rho)_{rad} \tag{2.2}$$

The collisional stopping power is important for dose calculations, the total is used in electron range calculations, and both the radiative and total stopping powers are used to calculate the radiation yield/bremsstrahlung efficiency. Mass stopping power values, total, collisional, and radiative for various energies and media have been calculated and tabulated by the National Institute of Science and Technology (NIST)[30]. The mass collisional and radiative stopping powers for a selection of elements used within this work are shown in Figure 2.4.

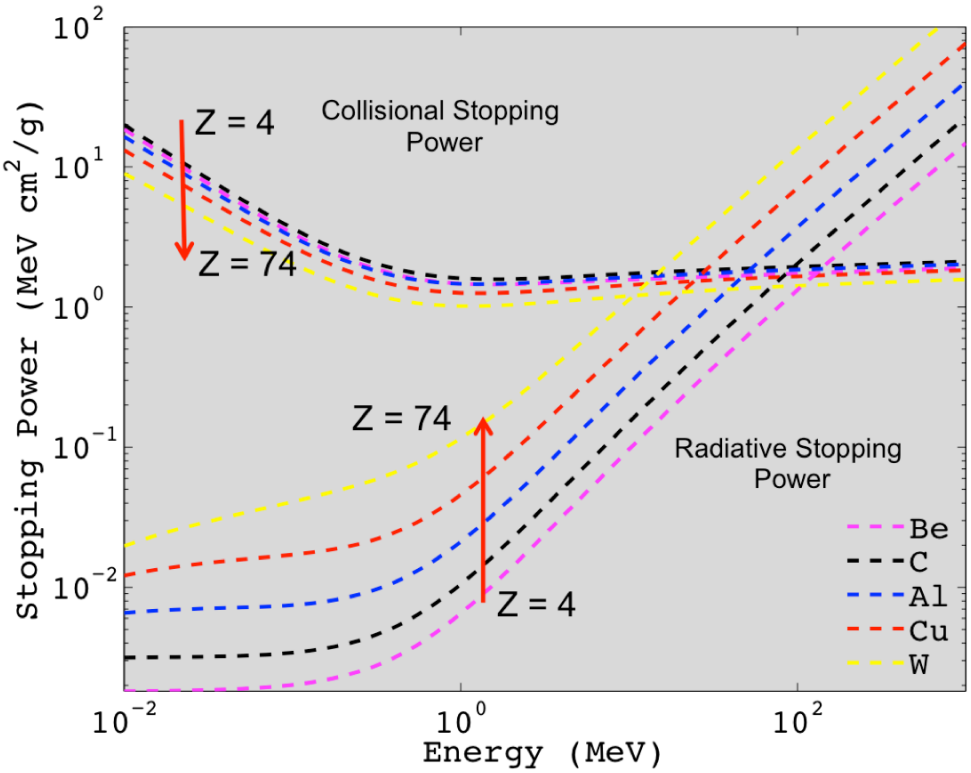

Figure 2.4: Mass collisional (upper curves) and radiative (lower curves) stopping power curves are displayed versus energy for beryllium (Z = 4), carbon (Z = 6), aluminum (Z = 13), copper (Z = 29), and tungsten (Z = 74). Both axes are logarithmic.

Collisional interactions are dominant within the low energy spectrum, while the radiative component increases above 511 keV due to increased bremsstrahlung production. Heavier (higher Z) materials have a higher radiative stopping power, and a lower collisional stopping power (Figure 2.4). The above figure also illustrates that the mass radiative stopping power is dependent on Z and E_K, which is also evident in the value's equation:

$$(S/\rho)_{rad} = \alpha r_e^2 Z^2 \frac{N_A}{A} E_i B_r \quad (2.3)$$

Where α is the fine structure constant (~ 1/137), r_e is the classical electron radius (2.818 fm), N_A is Avogadro's number (6.022 x 10^{23}), A is the atomic mass, E_i is the initial total energy ($E_K + m_e c^2$), and B_r is a slowly varying function of Z and E_i.

The mass stopping power (rate of energy loss per gram per square centimeter MeV·g^{-1}·cm^{-2}) is lower in high atomic number materials than low atomic number materials and this is due to high atomic number materials having a high number of tightly bound electrons unavailable for inelastic interaction, as well as having fewer electrons per gram than lower atomic number materials.

The rate of radiative interactions is proportional to the electron energy and the square of the atomic number of the medium. Thus, bremsstrahlung production is more efficient for higher beam energies and higher atomic number materials[29].

Electrons begin to scatter significantly as soon as they enter a medium due to interactions with the Coulomb forces of the atoms within the material. The mean energy of the beam decreases as it propagates through the medium and its angular spread increases. High atomic number materials have a higher interaction cross-section.

2.1.5 Range (CSDA)

The CSDA range is an important concept for this project as it was used on multiple occasions for calculations and theory. An electron of a specific energy can only travel so far into a medium, this is known as the electron's range, which is dependent on the particle's kinetic energy, mass, charge, and the atomic composition of the absorption media. Electrons, since they are light charged particles, have significant angular deflections from elastic scattering due to hard collisions with the nuclei of atoms within the media. Due to the degree of scatter, it can be difficult to determine the mean path length of the electron, as demonstrated as the path length C in Figure 2.5.

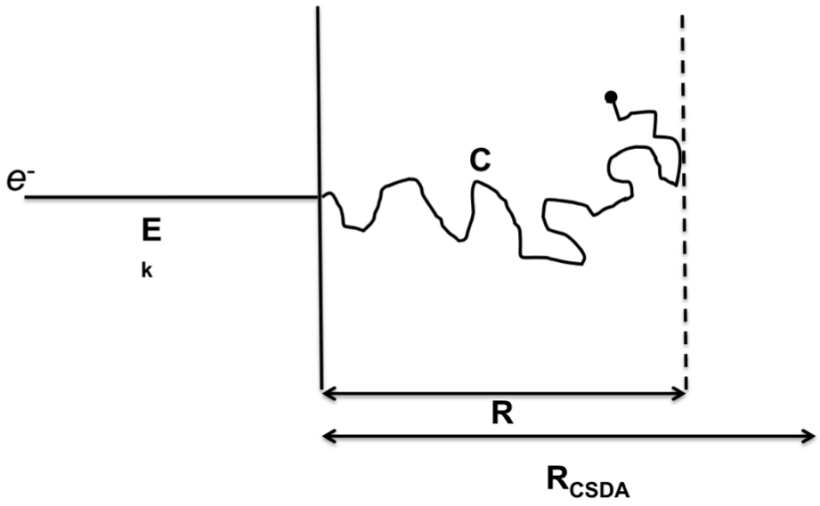

Figure 2.5: Illustration of an electron's tortuous path through a medium, demonstrating the concept of range and CSDA range. Range (R) is the projected displacement of the electron in the direction of the incident electron, whereas CSDA range is the total distance of the mean free path of the electron (total length of path C).

To compensate for this, a term coined the continuous slowing down approximation (CSDA) was proposed. The idea behind this concept is as follows: Electrons are surrounded by a Coulomb electric field which will interact with an electron

or nucleus of every atom it encounters; since each of these interactions transfer miniscule amounts of the electron's kinetic energy, the particle loses it's energy continuously and slowly along the entirely of its track. The CSDA range is an approximation of the average path length traveled by the electron as it comes to rest. It is a calculated quantity using the electron's initial kinetic energy and the reciprocal of the total stopping power:

$$R_{CSDA} = \int_0^{E_o} \left(\frac{S}{\rho}(E_K)\right)^{-1} dE_K \quad (2.4)$$

The R_{CSDA} values for various energies and media have been calculated and tabulated by the National Institute of Science and Technology (NIST)[30]. The parameter is commonly used to determine the correct thickness of a target material to be used in a clinical linear accelerator for a specific energy.

2.2 Photon Interactions with Matter

Photons interact with matter via orbital electrons or nuclei. However, they interact through four main interaction types, Compton scattering, photoelectric effect, pair production and Rayleigh scattering.

As photons interact, their energy is attenuated though the transfer of energy to atoms within the absorbing material with which they interact. The proportion of energy transferred depends on the interaction type, the photon energy and the atomic number (Z) of the absorbing media. Rayleigh scattering is solely an elastic event and only deflects the photon through small angles with negligible energy losses. The three

remaining interactions dominant different energy ranges for varying atomic numbers, which is displayed in Figure 2.6. The lines drawn within the figure indicate where the two interaction types have equal probability of occurrence. Within this work the main interactions of concern will be the photoelectric effect and Compton scattering

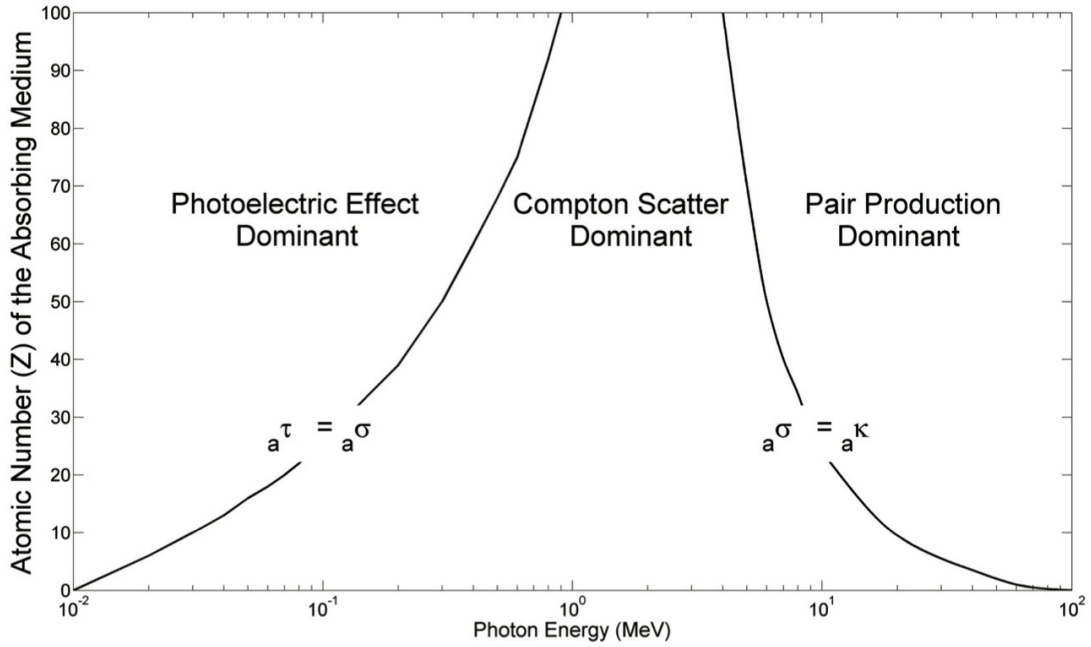

Figure 2.6: Atomic cross section for photoelectric effect, Compton effect, and pair production, as a function of photon energy and atomic number of absorbing media[28, 31].

2.2.1 Compton Scattering

Compton, or incoherent scattering, occurs when a photon, of energy hv, interacts with an atomic electron, which has a binding energy much less than that of the incident photon, i.e. an electron in the outer shells. This type of electron is designated a *free* electron, and is assumed to be stationary at the time of the collision. In the interaction, the photon transfers some of its energy to the free electron, which is then ejected from

the atom at an angle θ with energy E_K[28, 29]. The photon is scattered with reduced energy, hν', at an angle ϕ. This interaction is shown in Figure 2.7.

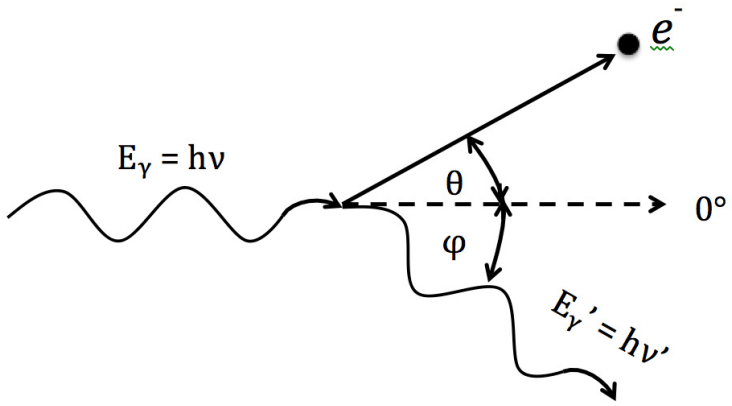

Figure 2.7: Diagram of the Compton effect. A photon of energy E_ν, strikes an unbound stationary electron, which scatters at angle θ relative to the incident photon. The photon scatters at angle ϕ with energy E_ν, as both momentum and energy are conserved in this interaction.

The scattered photon has energy hν':

$$h\nu' = h\nu \frac{1}{1+\varepsilon(1-\cos\varphi)} \tag{2.5}$$

where ε is the incident photon's energy, which is normalized to the rest mass of an electron ($h\nu/m_e c^2$). The ejected electron has energy E_K, given as:

$$E_K = h\nu \frac{\varepsilon(1-\cos\theta)}{1+\varepsilon(1-\cos\theta)} \tag{2.6}$$

The angles are related through:

$$\cot\theta = (1+\varepsilon)\tan\left(\frac{\varphi}{2}\right) \tag{2.7}$$

Thus for higher incident photon energies, the electron will scatter at smaller angles. For ϕ = 0, no energy is transferred to the electron, and a photon is emitted instead[28, 29]. The Compton interaction cross section per electron is given by the Klein Nishina formula:

$$\sigma_e = 2\pi r_e^2 \left[\frac{1+\varepsilon}{\varepsilon^2}1+2\left(\frac{2(1+\varepsilon)}{1+2\varepsilon}-\frac{\ln(1+\varepsilon)}{2\varepsilon}\right)+\frac{\ln(1+2\varepsilon)}{2\varepsilon}-\frac{1+3\varepsilon}{(1+2\varepsilon)^2}\right] \tag{2.8}$$

The Compton mass attenuation coefficient is given as:

$$\frac{\sigma}{\rho} = \frac{N_A}{A}\sigma_e \ \ (\frac{cm^2}{g}) \tag{2.9}$$

Where ρ is the density of the absorbing media, N_A is Avogadro's number, and A is the mass number. Therefore, for most materials, the Compton mass attenuation coefficient is independent of the atomic number[28, 29].

2.2.2 Photoelectric Effect

The photoelectric effect occurs when a photon of energy hν is incident on a tightly bound orbital electron within an atom. The entire energy of the photon is absorbed and transferred to the electron, allowing it to be ejected with kinetic energy equal to hν - E_B, where E_B is the binding energy of the electron. This is depicted in Figure 2.8. The photoelectric effect typically occurs within the K, L, M, or N shells of the atom, and can only occur if the incident photon's energy is greater than that of the binding energy of the emitted electron. Momentum is conserved in the collision, though the atom recoils with negligible kinetic energy[28, 29].

A vacancy is created when the electron is ejected from the atom, leaving it in an excited state. An outer shell electron can fill the vacancy with the emission of a characteristic x-ray. A cascade effect can take place if the atom absorbs the characteristic x-rays, releasing Auger electrons[28, 29].

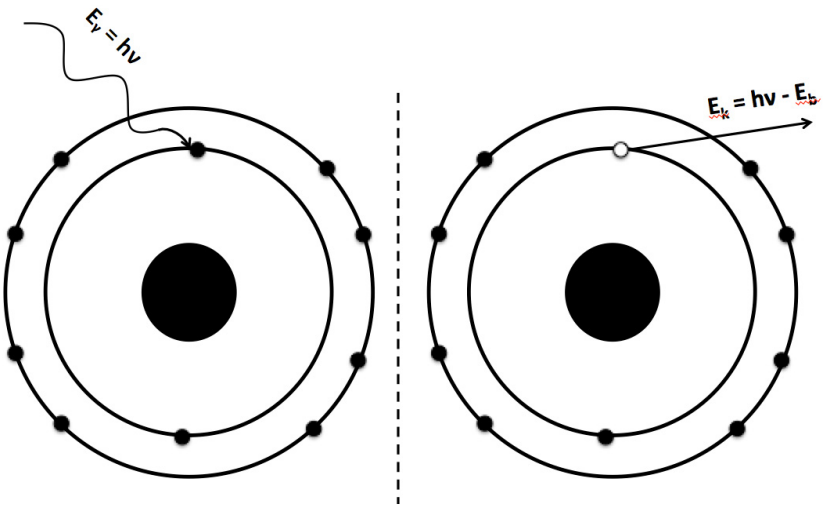

Figure 2.8: Diagram of the photoelectric effect. A photon of energy E_γ, strikes an electron that is bound to an atom. The photon transfers all energy to the electron, which leaves with kinetic energy equivalent to that of the incident photon minus the binding energy between it and the atom.

The cross section is proportional to Z^4 and inversely proportional to $(h\nu)^3$, for interactions above the k shell[28, 29]. Interactions within the k shell are proportional to Z^4 up to $Z^{4.8}$, depending on incident photon energy, and are inversely proportional to energy[28, 29]. The photoelectric mass attenuation coefficient is:

$$\frac{\tau}{\rho} \approx \propto \left(\frac{Z}{h\nu}\right)^3 \quad \left(\frac{cm^2}{g}\right) \tag{2.10}$$

Thus, photoelectric effect mass attenuation is proportional to Z^3, meaning more interactions will occur in higher atomic number materials at a given energy[28, 29]. This interaction type is the dominant process used for x-ray imaging.

2.2.3 Pair Production

Pair production can occur if the energy of the photon exceeds $2m_ec^2$ (1.02 MeV), the rest mass of the electron-positron pair. The photon interacts with the electromagnetic

field of the nucleus, giving up all of its energy, to created charged particles[28, 29]. If the photon is in excess of the rest mass energy of the electron-positron pair, this energy the remainder of the energy is split between the pair as kinetic energy. The total energy of the pair is hν – 1.022 MeV. The process is demonstrated in Figure 2.9.

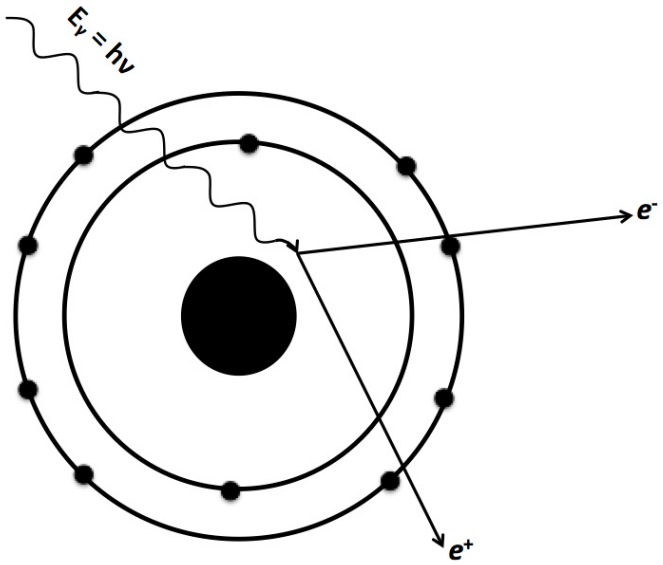

Figure 2.9: Diagram of the pair production occurring in Coulomb force field of an atom. A photon of energy E_γ vanishes, producing an electron, positron pair. Momentum is conserved.

The energy is most often split evenly between the electron-positron pair, though any distribution can occur. The mean kinetic energy of the pair is:

$$\overline{E_K} = \frac{1}{2}(h\nu - 2m_e c^2) \tag{2.11}$$

The mass attenuation coefficient is given as:

$$\frac{\kappa}{\rho} = \frac{N_A}{A}\kappa_a \cong \frac{N_A}{A}\frac{1}{137}r_e{}^2 Z^2 P(\varepsilon, Z) \quad (\frac{cm^2}{g}) \tag{2.12}$$

where r_e is the classical electron radius, and P(ε,Z) is a function of the photon energy and the atomic number of the absorber. Thus, the atomic cross section is proportional

to Z^2 of the medium. The mass coefficient is linearly Z dependent since Z/A is approximately constant for all elements except for hydrogen[28, 29].

Eventually the positron will undergo an annihilation event once it has expended all its kinetic energy through collision interactions. Typically, annihilation occurs with a free and stationary electron. The event results in two photons, each with energy equivalent to $m_e c^2$, and scatter almost in opposing directions. In-flight annihilation occurs infrequently, 2% of annihilation interactions. This type differentiates from annihilation as the electron is still tightly bound to an atom, or is an in-flight free electron[28, 29]. In the tightly bound scenario, the nucleus recoils and only one photon results, in the latter scenario, the resulting photons will leave with two different energies[28, 29].

2.2.4 Rayleigh Scattering

Rayleigh scattering, or coherent scattering, is an interaction in which photons are elastically scattered by bound electrons. Since the photon loses no energy and momentum is conserved by recoil of the atom the interaction is elastic. The photon is typically only scattered by a small angle. The interaction is most probable with low energy photons and high Z materials. The atomic cross section is:

$$\eta_a \approx \left(\frac{Z}{h\nu}\right)^2 \tag{2.13}$$

The mass attenuation coefficient is:

$$\frac{\eta}{\rho} \approx \frac{Z}{(h\nu)^2} \quad \left(\frac{cm^2}{g}\right) \tag{2.14}$$

This interaction type contributes little to the total mass attenuation coefficient[28, 29].

2.2.5 Attenuation Coefficient

Within a medium, the mass attenuation coefficient (μ/ρ), electron cross-section (μ_e), and atomic cross sections (μ_a) are the sum of individual interaction cross sections which a photon may undergo during attenuation within a medium:

$$\mu_e = \eta_e + \tau_e + \sigma_e + \kappa_e \ (cm^{-1}) \quad (2.15)$$

$$\mu_a = \eta_a + \tau_a + \sigma_a + \kappa_a \ (cm^{-1}) \quad (2.16)$$

$$\frac{\mu}{\rho} = \frac{\eta}{\rho} + \frac{\tau}{\rho} + \frac{\sigma}{\rho} + \frac{\kappa}{\rho} \quad \left(\frac{cm^2}{g}\right) \quad (2.17)$$

The mass attenuation coefficient and its components are displayed in Figure 2.10, for carbon, and is plotted as a function of energy.

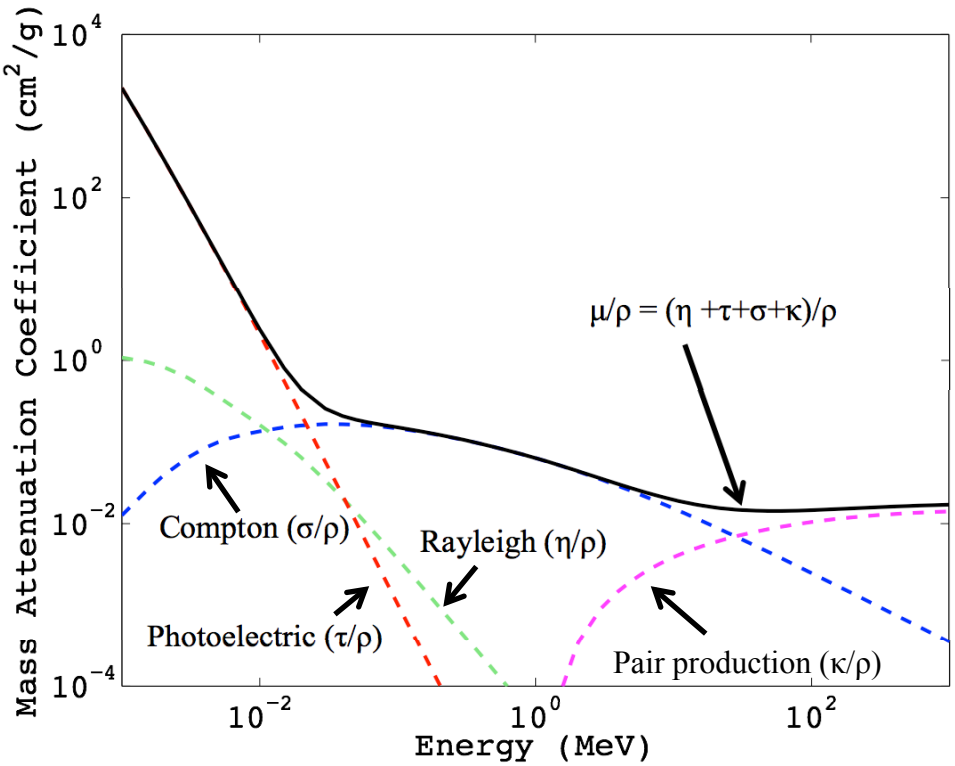

Figure 2.10: Mass attenuation coefficient versus photon energy from 1 keV to 100 MeV for carbon. The individual interaction coefficients are also shown for Rayleigh (η/ρ), photoelectric (τ/ ρ), Compton (σ/ρ) and pair production (κ/ρ). Data was obtained from the National Institute of Standards and Technology (NIST), Washington, DC[30].

2.3 Electron and Photon Beam Characteristics

A photon beam propagating through a patient or phantom will deposit dose differently than if it were traversing through air. In air, the beam is governed by the inverse square law. In other media it is affected by the inverse square law, as well as attenuation and scattering of the photon beam that will occur inside the media.

2.3.1 Electron Beam Characteristics

Electrons are an important treatment modality in radiation therapy due to their different characteristics from photon beams (that are mainly used to treat superficial tumours (< 5cm)). They are characterized in the same manner as photon beams, collecting dose readings along the central axis of the radiation beam, although the shape of the resulting PDD has marked differences. These differences are demonstrated in Figure 2.11. Electron beams have a high surface dose, the build up region does not have a steep gradient, dose distribution falls off after d_{max}, and levels off to a low dose component that is referred to as the bremsstrahlung tail. The bremsstrahlung tail is due to x-ray production in the linac head, in the air between the patient and exit window, and in the patient/medium itself (< 1% for 4 MeV, < 4% for 20 MeV).

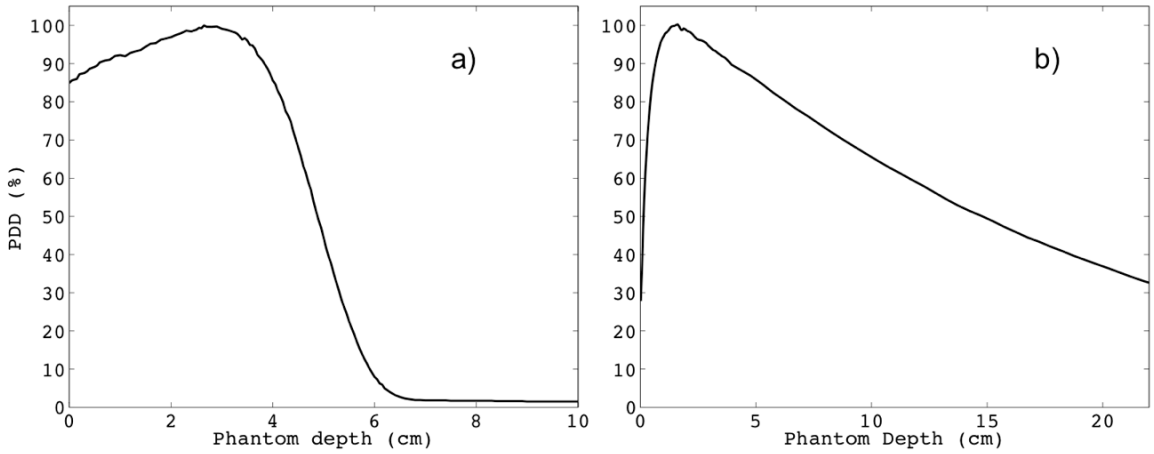

Figure 2.11: PDD central axis curves in water for a) 12 MeV electron beam, and b) 6 MV photon beam. Both are taken with 10 x 10 cm^2 field size and SSD of 100 cm.

To produce an electron beam, the target and flattening filter are removed from the beam-line and in their place a scattering foil is placed in the flattening filter position. Electrons entering a medium interact through the Coulomb force interactions discussed in section 2.1. With elastic collisions, the electrons change direction or their energy is redistributed, but kinetic energy is not lost. Inelastic collisions cause a loss in kinetic energy, producing ionizations or a conversion of portions of electrons' energy into photon or excitation energy; these interactions cause direct dose deposition. Therapeutic electron beams average an energy loss of 2 MeV/cm in water and water equivalent materials, such as tissue. The rate of energy loss depends on the energy of the beam as well as the electron density of the medium[29].

The electron beam is characterized by five main parameters: the depth at which the PDD achieves a value of 90% beyond d_{max} (R_{90}), the depth at which the PDD achieves a value of 50% beyond d_{max} (R_{50}), the depth where the tangent through the inflection point intersects the max dose (R_q), the depth where the tangent of the inflection point

intersects the extrapolation of the bremsstrahlung tail (R_p), and the point where the electron curve disappears into the bremsstrahlung tail (R_{max}). These points are shown on a generic electron PDD in Figure 2.12. All values are measured in cm or g/cm^2. The range/penetration depth (R_p) of the beam increases with beam energy and is generally half of the beam energy, i.e. a 6 MeV beam has an R_p of 2.9 cm, an 8 MeV has an R_p of 4.0 cm. R_{90} is known as the therapeutic range of an electron beam, and is typically equivalent to *E*/4 in cm, where *E* is the electron beam energy. R_{50}, the beam quality index, and R_q are used in equations to determine the mean energy at the phantom surface and the electron dose gradient, respectively. R_{max} is the largest penetration depth within the medium.

The build up region in electron beams is significantly higher than that of photon beams due to the scattering interactions that the electrons undergo with the atoms in the absorption medium. The electrons enter the medium parallel, then begin to scatter, diverting from their original path, causing the electron fluence along the central axis to increase. Secondary electrons created in collision interactions also contribute to the dose build up. The surface dose increases with electron beam energy, unlike the surface dose of photon beams. The dose deposition falls off rapidly after d_{max} because of scattering and the continuous loss of energy of the electron beam from interactions with the absorption medium.

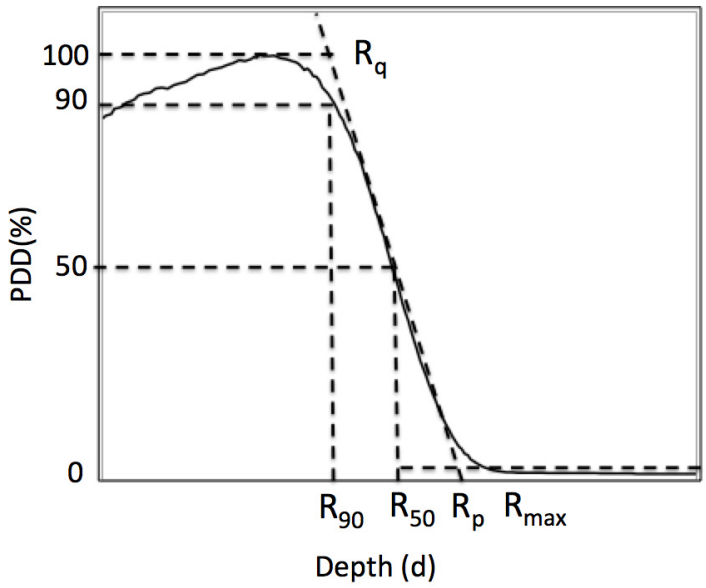

Figure 2.12: Dose deposition of a MeV electron beam through a homogenous tissue equivalent patient phantom. R_{max} is the point where the electron curve disappears into the bremsstrahlung tail.

2.3.2 Photon Beam Characteristics

To characterize a photon beam, a typical measurement performed is a reading along the central axis of the photon beam as it passes through the phantom. This allows several important features of the dose distribution to be identified. These features include the surface dose (D_S), the build-up region (occurs between d_s and d_{max}), maximum dose (D_{max}), the depth of maximum dose (d_{max}), the dose falloff as it passes through the phantom, and the dose at the point the beam exits the phantom (D_{ex}). Each of these parameters is displayed in Figure 2.13.

The graphical representation of the dose along the central axis as a function of depth through the patient is an important beam characteristic called the percentage

depth dose (PDD) distribution, where D_{max} is normalized to 100%. The PDD can be used to identify the energy of a beam, and the type of beam.

$$PDD = 100\left({}^{D_n}/_{D_{max}}\right) \tag{2.18}$$

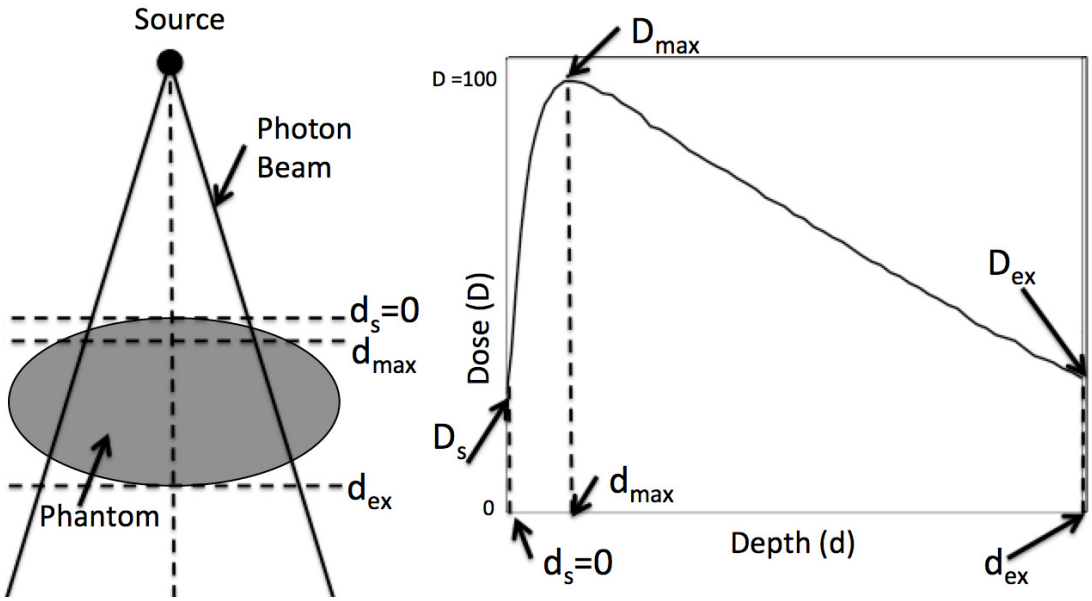

Figure 2.13: Dose deposition of a megavoltage photon beam through a homogenous tissue equivalent patient phantom. D_s is the dose at the surface, D_{max} is the maximum dose, D_{ex} is the surface dose at the beam exit point, d_s, d_{max} and d_{ex} are the distances within the phantom that each of these dose points occur, respectively. The resulting curve is referred to as a percentage depth dose (PDD) distribution.

The surface dose for a megavoltage photon beam is significantly lower than the maximum dose, which occurs at d_{max}, though it is also nonzero. The surface dose is nonzero due to three main sources of dose deposition: scattered photons from collimators, flattening filter, and air; backscattered photons originating within the patient; and electrons produced by photons interacting in air or with any shielding used on the patient[29].The surface dose depends greatly on the energy and field size of the beam. Higher energy beams contribute lower surface dose, though surface dose

increases as field size increases. The effect field size has on surface dose is due to the contribution of scatter from the head of the machine to the deposited dose. The effect of energy will be discussed in a further section.

The build-up region exists due to the range of secondary charged particles created in the patient from photon interactions. As secondary charged particles are created within the medium there will be a forward moving and backscattered component. The backscattered component increases gradually with depth, and will not be equivalent to the forward component until equilibrium is reached at d_{max}, which is approximately equal to the range of the secondary charged particles. This balance of forward and backscattered electrons results in low dose at the surface, which increases to a maximum at equilibrium (d_{max}).

The depth at which D_{max} is reached, d_{max}, is dependent on the beam energy and, minimally, the field size. Higher beam energies are more penetrating, thus will propagate further through the phantom before CPE is reached. The opposite is true for beams of lower energy. Examples of the variation of d_{max} with photon beam energy are shown in Table 2-1.

Table 2-1: Depths of D_{max} for a variety of photon beams. The field size for each is 5 x 5 cm^2.

	4 MV	6 MV	10 MV	18 MV	25 MV
d_{max} (cm)	1	1.5	2.5	3.5	5

2.4 Beam Generation in a Linear Accelerator

Radiation therapy is delivered by clinical linear accelerators, generally known as linacs. Developed in the 1940's and 50's, linacs have since become highly precise instruments for the treatment of cancer. Medical linacs can accelerate electrons from 4 MeV to 25 MeV through the use of microwave radiofrequency (RF) waves with a frequency between 10^3 MHz and 10^4 MHz. Modern linacs operate at two photon energies, 6 and 18 MV, and several electron energies (6, 9, 12, 16, 22 MeV). There is a rich history for these devises, though for the purposes of this work, the focus of this section will be on the inner workings of the accelerator modeled and used during this research, depicted in Figure 2.14.

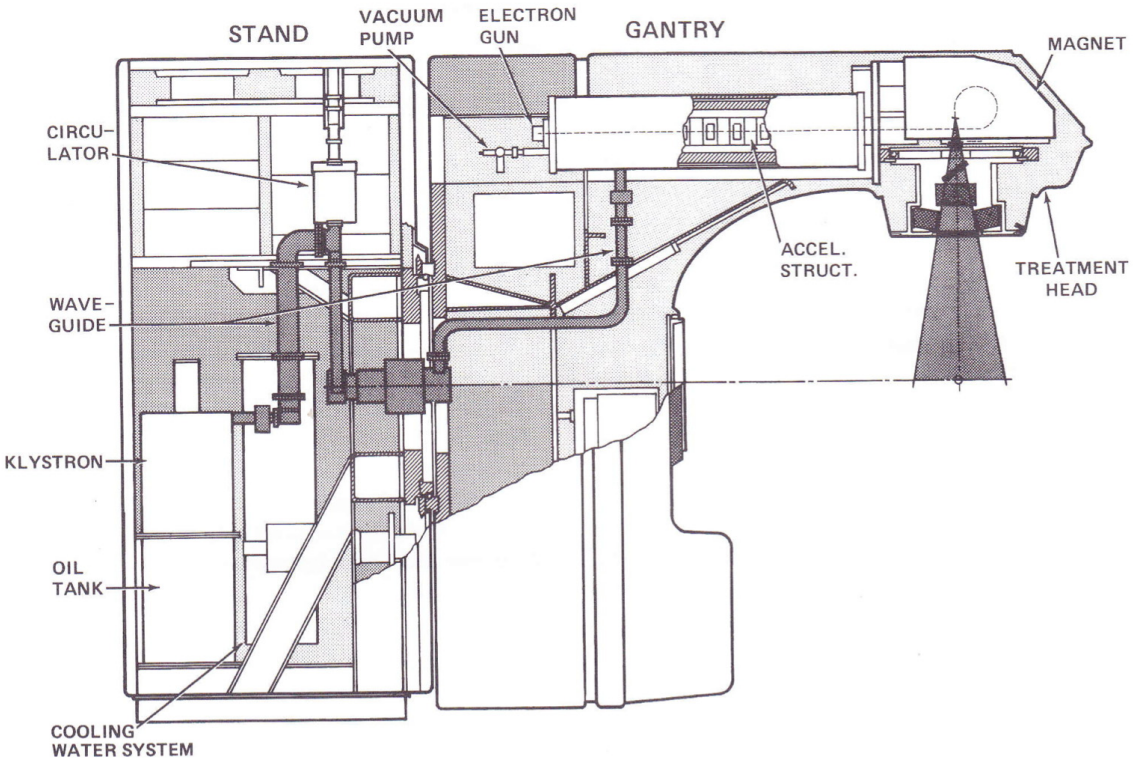

Figure 2.14: Schematic of a clinical linear accelerator[32]

The main component of the injection system is the source of electrons, the electron gun. The electron gun in Varian linacs, which are in use at the NSCC, is a triode design composed of a heated cathode, a grid, and a perforated grounded anode. Upon heating the cathode, electrons are thermionically emitted. They are focused into a pencil beam and accelerated towards the perforated anode, through which they exit into the accelerating waveguide. This component will be discussed in more detail in the following sections.

The RF power generation is produced by a klystron, though earlier and other models may have used a magnetron. The klystron operates in the S-band (2856 MHz). The RF waves are transferred to the accelerating waveguide, thereby accelerating the electrons injected by the electron gun through gains in kinetic energy.

The accelerating waveguide is an evacuated cylindrical waveguide composed of cavities separated by irises at equal intervals. Focusing coils encases the waveguide. The coils form a solenoid that produces a magnetic field parallel to the axis of the waveguide. This serves to limit the electron beam diameter, ensuring no loss of beam through collisions with the waveguide. Steering coils are positioned at each end, forming an orthogonal dipole moment, which can be used to deflect the electron beam horizontally and vertically. These can be used for beam angle correction at the entrance and exit of the waveguide.

The auxiliary system includes many components that are not directly involve in beam transport, but are vital for operation of the linac. This includes the vacuum

pumping system, water-cooling, air-pressure system, and shielding against radiation leakage.

The waveguide is placed orthogonal to the linac head, as the waveguide must reach specified lengths to accelerate electrons to specified high energies. Thus, the beam must be bent in order to be incident on the target housed in the head of the linac. This is achieved through the use of three achromatic magnets, together referred to as the bending magnet, which will effectively rotate the beam through 270°. The current to the bending magnet can be adjusted to select the electron energy that will exit the bending magnet. This will be discussed in the following section.

Upon exit of the bending magnet the beam is incident upon a thick target (110% of the R_{CSDA}) housed within the linac head. This interaction produces bremsstrahlung and characteristic x-rays, generating the desired photon beam. The photon beam produced at these high energies are forward peaked, thus a flattening filter is placed in the beam-line. The flattening filter is specifically designed for each photon energy to ensure a flat profile of the central 80% region of the beam at a depth of 10 cm in water with a source-to-surface distance (SSD) of 100 cm for a 40 x 40 cm^2 field, or the largest field possible.

Upon exit of the flattening filter, the beam will then travel through dual ionization chambers, which monitor the delivered dose from the beam. These ionization chambers are referred to as monitor chambers. The monitor chambers are calibrated at each center such that 1 MU (monitor unit) is equivalent to 1 cGy delivered to a water phantom at a specified depth. At the NSCC, the monitor units are calibrated such that 1

MU = 1 cGy at a depth of 5 cm with a 10 x 10 cm^2 field at 95 cm SSD. The monitor chambers may also be used to monitor beam flatness and symmetry, allowing correction of these parameters by actively steering the beam through a feedback loop. There are two monitor chambers as a fail-safe, one is designated the primary while the other serves as a secondary backup in case the primary fails. The read out from the chambers is used in software to terminate the beam as soon as the prescribed number of MUs (dose) has been reached.

The radiation beam undergoes three layers of collimation to minimize exposure to the healthy tissue and maximize dose to the target volume. The primary collimation occurs immediately after the target, defining the maximum possible radiation field. The primary collimator consists of a tungsten slab with an evacuated conical aperture with a maximum radius of 20 cm at the end of the collimator. The shape of the radiation field is defined by the secondary and tertiary collimation. Secondary collimation is composed of two sets of tungsten blocks, referred to as jaws, oriented orthogonal to each other. The jaws allow square or rectangular fields, with a maximum of 40 x 40 cm^2. The edges of the jaws are parallel with the radiation beam at all angles, thus move in an arc within the linac head. Tertiary collimation is achieved by the multileaf collimator (MLC) system. The MLC is designed to allow irregular field shapes, which are typically achieved by 120 computer controlled tungsten leaves.

To operate the linac in electron mode the beam line must be modified. The target arm is retracted, and the flattening filter replaced by a scattering foil. Upon exit of the bending magnet the electron beam will travel through the beryllium exit window

and air until incident on the scattering foil, which will scatter the electron beam to allow for coverage of clinical field sizes. The components of the linac head, as well as air, tend to highly scatter the electrons causing a significant penumbra. To compensate for this effect the tertiary collimation is adjusted, the MLC leaves are retracted, the jaws are widened slightly more than the prescribed field size, and an applicator is attached to the linac head. A Cerrobend cutout of the target volume shape can be inserted into the end of the applicator, allowing maximum collimation and shaping of the electron beam.

2.4.1 Bending magnets

In low energy linacs (< 6 MV) the waveguide can be positioned in-line with the target and within the linac head, however, variable medium and high energy linacs have a substantially longer standing waveguide and do not fit within the linac head. The waveguide typically extends into the gantry. For the accelerated electron beam to be incident on the target, the beam must be bent. The bending magnet was designed to deflect the beam 270 °. This serves to ensure incidence on the target, and focuses the beam. Lower energy electrons trace a curve of smaller radius whereas higher energies take on larger curves, Figure 2.19. The achromatic magnet merges every curve so that the beam incident on the target is the same as that entering the magnet. Adjusting the voltage across the bending magnet, the energy of the electron beam exiting the magnet can be tailored[32]. High energies can be shaved off by making them strike the linac walls.

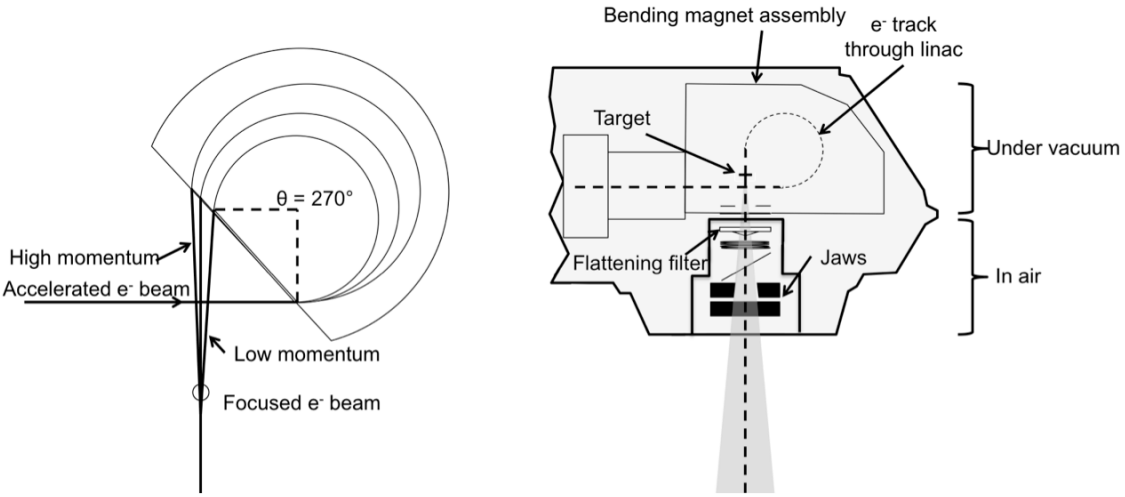

Figure 2.19: Left: Close up view of electron beam entering the bending magnet. Right: cut-away diagram showing how the bending magnet and other components fit within the linac head.

2.5 X-ray Detection

There are many devices and instruments that are used for the detection of radiation, such as thermoluminescent dosimeters (TLD), ionization chambers, semiconductor dosimeters/diodes, organic and inorganic scintillators, and electronic portal imaging devices. In this work ion chambers and diodes were used, and are discussed below.

2.5.1 Ion Chambers

Ion chambers are designed in various shapes and sizes, though all follow the same basic principles. An ion chamber must consist of three main components: a gas filled cavity, a central collecting electrode, and is surrounded by a conductive outer wall. An insulator

separates the electrode and wall. The wall is made of tissue or air equivalent materials (i.e. low atomic number) so that it does not attenuate the electrons or photons. The active volume for typical cylindrical ion chambers ranges between 0.1 and 1 cm^3. With the wall material being graphite and the central electrode being aluminum. A diagram of a typical cylindrical ion chamber is shown in Figure 2.20.

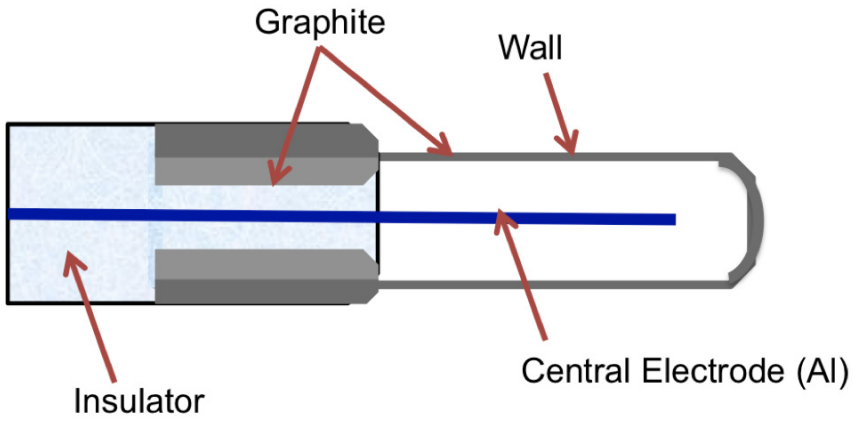

Figure 2.20: Schematic of a typical cylindrical ion chamber. The materials shown here are common to cylindrical ion chambers.

The ion chamber works on basic principles of radiological physics. Secondary electrons are produced when the photon beam (through interactions discussed in previous sections) is incident with matter. These can be produced outside the wall of the chamber, in the wall, or inside the gas filled chamber. Secondary electrons can ionize atoms or molecules as they pass through matter. To detect these ionizations, a potential difference is applied between the wall and central electrodes within the ion chamber. This causes the negative and positive ions to be attracted towards the anode (central electrode) and cathode (wall), respectively. The collected charge is measured by connecting the ion chamber to an electrometer prior to beam initiation. The

electrometer is also responsible for supplying the potential difference to the electrodes within the ion chamber.

2.5.2 Semiconductor Dosimeters

Silicon diodes used for dosimetry are p-n junction diodes. In radiotherapy dosimetry, p-Si dosimeters are preferred[29]. P-Si diodes are produced by taking p-type silicon (silicon doped with boron or aluminum to produce additional holes) and counter-doping the surface with n type silicon (doping with phosphorous or arsenic). P-type is used since it is not as susceptible to radiation damage, and has a smaller dark current[29]. Diodes cannot be used as an absolute dosimeter because they are sensitive to radiation damage over time, and thus they should only be used as a relative dosimeter[29].

When primary or secondary electrons cross the diode, electron-hole (e-h) pairs are created throughout the dosimeter. The charges created in the n-doped silicon diffuse into the depletion layer and are swept across it due to the attraction to the p-type silicon from the intrinsic electric potential. This motion of charge creates a current in the reverse direction of the diode. A diagram of this interaction is shown in Figure 2.21.

Silicon diodes are useful for measuring electron beams and low energy photons because of lower levels of backscatter compared to germanium diodes. They also directly measure the dose distribution of electron beams rather than ionization, which cuts down on post data processing. Diodes are advantageous when measuring high dose

gradient regions, such as photon beam penumbra and build-up regions. They are sensitive to temperature, and so will show variations in dose response.

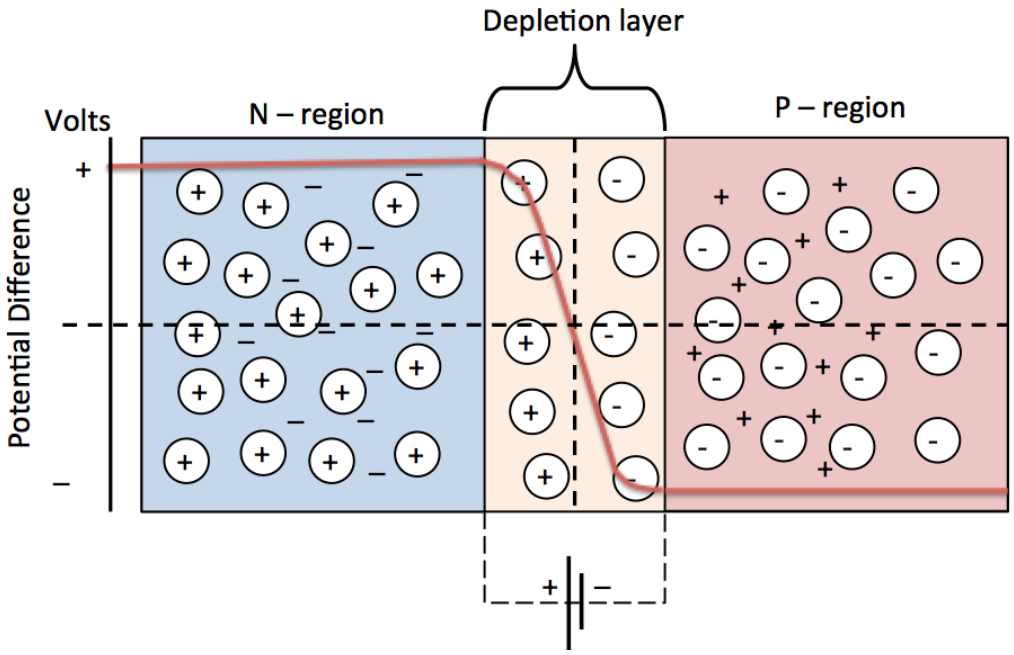

Figure 2.21: Diagram of p-n junction diode showing the n and p doped regions depicted by their respective positive donor ions and negative donor ions, the depletion layer, as well as the individual electrons and holes. An overlay of the potential difference is included to show the intrinsic electric potential and the motion of charge.

CHAPTER 3 MATERIALS AND METHODS

3.1 MONTE CARLO SIMULATIONS OF LOW-Z TARGETS

3.1.1 Beam Energies and Target Materials

The low energy beam characteristics of four low-Z elements were investigated: beryllium (Be), carbon (C), Aluminum (Al), and Copper (Cu). These elements were decided upon based on a literature review of relevant publications (see section 1.5). Ideally the target material should be readily available, easily manufactured, affordable, and safely handled in a clinical environment. The beam energies used throughout the research were 4 MeV and 2.5 MeV. The former was chosen as it is a standard energy available on most clinical linear accelerators in operation today, and the latter was chosen since it was close to the lowest stable energy achieved in previous research done at Dalhousie University[27].

3.1.2 Determination of Target Thicknesses

The mean energy of the target photon spectrum was only a component of our design criteria; target thickness was the other. The thicknesses investigated were based on 60% R_{CSDA} providing optimum fluence of low energy photons[26]. Using 60% as a start point, 30% and 15% were chosen to provide a range of values. Thicknesses were calculated for each material as a percentage of the CSDA range (NIST database[30]) for each element/energy combination. The original data for each value is shown in Table

3-1. By dividing CSDA range (g/cm^2) by density (g/cm^3), a target thickness in cm was determined and is shown in Table 3-2. This data was used for all subsequent Monte Carlo simulations, the main mode of research during this project.

Table 3-1: Density and CSDA range for each element and energy investigated.

Element	Density (g/cm^3)	CSDA range (g/cm^2)	
		2.5 MeV	4 MeV
Be	1.850	1.568	2.563
C	1.700	1.423	2.323
Al	2.702	1.550	2.491
Cu	8.933	1.750	2.772

Table 3-2: Calculated target thickness for each element, energy and % CSDA of interest.

	Full CSDA (cm)		60% CSDA (cm)		30% CSDA (cm)		15% CSDA (cm)	
Element	**2.5 MeV**	**4 MeV**	**2.5 MeV**	**4 MeV**	**2.5 MeV**	**4 MeV**	**2.5 MeV**	**4 MeV**
Be	0.848	1.385	0.509	0.831	0.254	0.416	0.127	0.208
C	0.712	1.168	0.429	0.701	0.215	0.350	0.107	0.175
Al	0.574	0.922	0.344	0.553	0.172	0.277	0.086	0.138
Cu	0.196	0.310	0.118	0.186	0.059	0.076	0.029	0.047

3.1.3 Monte Carlo

Monte Carlo (MC) is a class of computational algorithms that uses random number sampling of known probability distributions to determine the most likely outcome for an

initial set of parameters. For the research presented herein, the MC package used was EGSnrc[33] (Electron Gamma Shower), the gold standard for MC simulation of radiation transport. This package includes the user codes, BEAMnrc[34] and DOSXYZnrc[35], which were used to model the transport of radiation through a simulated linac and dose deposition in phantoms, respectively[33, 36]. These simulations take a significant amount of computational resources as the code is tracking each electron and photon in a simulation involving 10^9 or more electrons. Considering that a secondary electron can undergo 10^6 elastic/inelastic collisions until being absorbed by the media in the simulation, a simulation takes a large amount of computing power and time. Simulations are done in two stages: first, the simulation of the linac and beam-line configuration used during experiments, accomplished using BEAMnrc, and second, using the output from BEAMnrc as input to DOSXYZnrc to see the effects of the modified beam-line on the dose distribution.

BEAMnrc allows the user to define the basic components of a linac head using a generic set of component modules (CMs), define the source characteristics, and control over parameters that affect the efficiency of the simulation. The data resulting from the simulations can be scored anywhere along the beam-line by specifying a plane through which all passing particles are recorded; this is referred to as the phase space. Information such as particle energy, position, direction, weight, charge, and location of the last interaction, is stored for each crossing particle. The phase space can then be used as an input into another BEAMnrc simulation of a lower section of the linac, used with DOSXYZnrc to score dose within a phantom, or analyzed with BEAMdp.

BEAMdp is used to analyze phase space results; it can derive information such as the fluence vs. position, spectral distributions, energy fluence, energy distributions, a list of parameters for a specified number of particles in the phase space, and can be used to combine two discrete phase spaces together. The output from BEAMdp is typically a text document or in a window displaying the information.

Previous research at Dalhousie University made use of MC; specifically modeling and running simulations of Varian Clinac medical accelerators that are present at the Nova Scotia Cancer Center (NSCC) facility[23, 27]. The simulated linac used for this research was modeled to reflect the set-up of validated MC models provided by Parsons and Robar[27]. Differences between the clinical beam-line and the modeled low-Z beam-line used for simulations in this research, such as target location and removed components, are illustrated in Figure 3.1.The accelerator used as the base model for these projects was the Varian 2100EX. A slight modification was made to the model to reflect the discovery that copper is present in the monitoring chambers within the Clinac beam-line.

The CMs used to construct the simulation were FLATFILT, CHAMBER, MIRROR, JAWS, and SLABS to construct the primary collimation/low-Z target, monitor chambers, mirror, jaws, and exit window, respectively. Each CM operates independently from the others, and is centered on the z-axis in-line with the central axis. The user inputs parameters for each CM manually, including position and composition. The location of the phase space is also user-oriented by specifying which CM it is placed after. It must

be placed on the exit side of the CM. The general setup of a BEAMnrc run used in this research is shown in Figure 3.2.

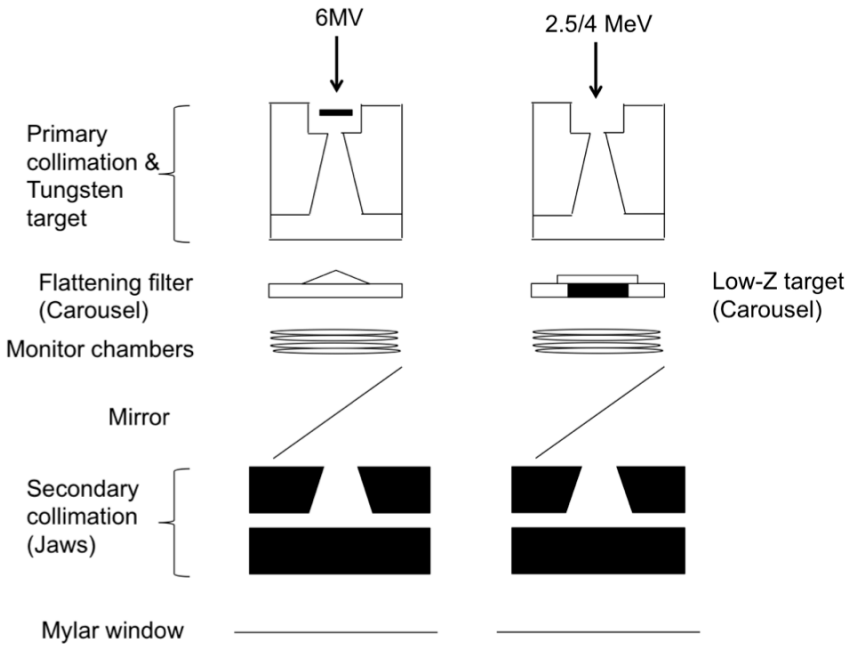

Figure 3.1: Diagram of the original 6MV and modified low-Z beam-line. The 6MV beam-line is in photon mode, target above the primary collimation, flattening filter below in the carousel. The low-Z is in electron mode, primary target retracted, with low-Z target placed in carousel. Reproduced from Orton and Robar (2009)[23].

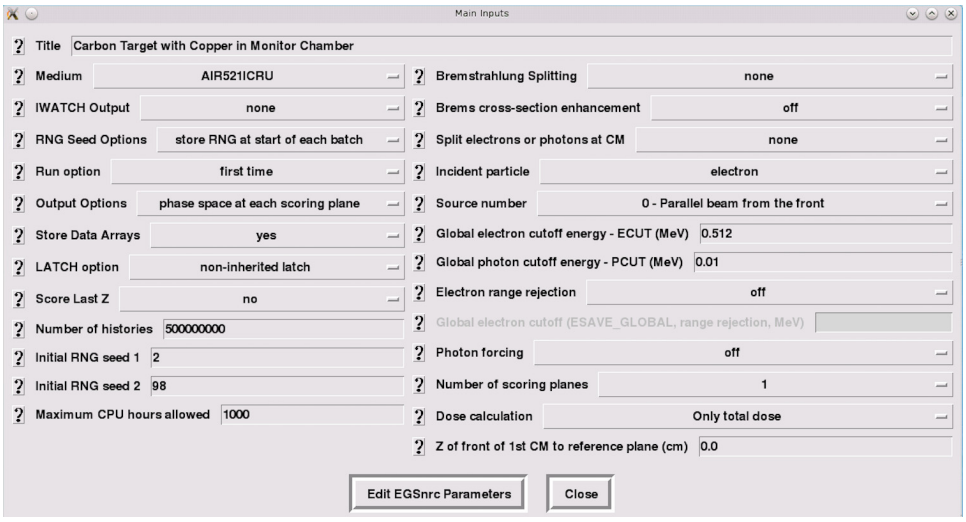

Figure 3.2: Setup of typical BEAMnrc simulation.

The source routine used was ISOURCE = 0, in which a parallel beam of either 2.5 or The source routine used was ISOURCE, in which a parallel beam of either 2.5 or 4 MeV with a 0.1 cm radius was generated at z = 0. The collimation of the linac was set to a 10 x 10 cm^2 field size at isocenter The approximate efficiency improving techniques (AEITs) used were global cut-off energies and the condensed history technique. The electron step algorithm used was PRESTA-II. Range rejection was not used in order to preserve electron precision. The global cut-off energies (PCUT and ECUT) were set at 0.010 MeV and 0.521 MeV, respectively, as low energy electron interactions are important in this work. Bremsstrahlung splitting, a variance reduction technique, was not used as this overwhelmed the electron contribution to the beam. The PEGS4 data file used for both BEAMnrc and DOSXYZnrc was 521icru.pegs4dat; it contains interaction cross-sections for various materials used in radiation therapy. This file allows radiation transport in EGSnrc to occur, and can be modified to include new materials by accessing the source code. The density and interaction cross-sections of carbon were entered this way.

The BEAMnrc simulations were designed for Be, C, Al, and Cu targets of varying thickness with energies of 2.5 and 4.0 MeV, and a total of $1.0x10^9$ – $1.0x10^{10}$ incident electron histories per target material. The variations in histories were dependent on target thickness and the requirement for statistical significance. The scoring plane was placed at the end of the Mylar exit window. For each run, unique initial random number generator (RNG) seeds were used to ensure true randomness when individual phase spaces were added together to create the combined total.

3.2 TARGET DESIGN

3.2.1 Fluence Spectra

The first step in the target design was to obtain the fluence spectra of our beams through MC simulations.

To determine the spectra, each beam-line configuration was run with $1.0x10^9$ – $1.0x10^{10}$ incident electron histories with the phase space collecting data at the end of the Mylar exit window. Using BEAMdp[37], the energy fluence versus position, energy fluence distribution, fluence versus position, and the spectral distribution for each target material and thickness were collected for the 2.5 MeV beam. Photon and electron contributions within each phase space were analyzed separately. The spectra was binned over 200 bins and ranged from 0.01 MeV to 2.5 MeV (the maximum potential energy as was set at the source in BEAMnrc).

The output text file was read into MATLAB through a function developed from previous work at Dalhousie University that would extract the energy and fluence data from the text file. The resulting fluence data were normalized by the area under the curve and could then be compared between materials as well as between differing R_{CSDA}.

3.2.2 Dose Distribution Within a Water Phantom

After the analysis of the resulting low-Z target spectra, the next step in characterizing these beams was to look at the dose distribution they exhibit in a water

phantom. Use of DOSXYZnrc allows the evaluation of dose distributions in a three-dimensional Cartesian geometry. The phantom space is divided into volumetric elements, voxels, that have a user specified dimension and composition. There is also an option to use a CT data set DICOM as a patient phantom. In this option, voxel composition is based on the Hounsfield units (HU) of the CT data. Without changing the source code the phantom used in DOSXYZnrc is limited to 128 x 128 x 128 voxels.

The phantom used in this step was a water slab phantom with dimensions of 20 x 20 x 27 cm^3. The global cut-off energies and PEGs file were kept the same as those used for the BEAMnrc simulations. The source type used was option (2) – Full phase-space source file. The input number of histories in DOSXYZnrc was set to be the actual number of particles registered to be present in the phase space source material. This value was found using BEAMdp. To achieve statistical accuracy in the resulting dose distributions, DOSXYZnrc requires a substantial increase in the number of incident histories than that in the original phase space[38]. To compensate for this, phase space particles in DOSXYZnrc can be recycled. Recycling the phase space was limited to 20x so as to not significantly affect the uncertainty of the dose distribution due to the same particle interacting in the same voxel twice[39]. The voxel size for these simulations were set to 0.2 x 0.2 x 0.05 cm^3, for the first 1 cm depth followed by 0.2 x 0.2 x 0.5 cm^3 for the remainder, to ensure a fine resolution of the z-axis and computational efficiency since the practical range of the beam was approximately 1 cm. It is important to note the trade-off between voxel dimensions and the number of histories required for valid statistics. Smaller voxel size will provide fine spatial resolution of the dose distribution,

at the cost of significantly increasing the histories required in order to maintain the same level of statistical uncertainty, thus discretion must be utilized when choosing voxel size and the avoidance of extraneous voxels is recommended. The output from DOSXYZnrc is a 3ddose file, which was analyzed using code generated within the MATLAB workspace. In MATLAB the 3ddose file was broken down into x-, y-, and z-dimensional data; dose distribution data, and associated error of the data. The resulting data were plotted to show the variations in PDDs of differing R_{CSDA} for each target material.

3.3 Addition of 6MV Therapeutic Beam

From the spectral and PDD data, a choice of carbon as the target material was made (see section 4.1). A BEAMnrc simulation of a standard 6 MV therapeutic beam-line[23, 27], was used and validated against previously obtained data at Dalhousie University. The phantom was changed to a 20 x 20 x 25 cm^3 water slab, with voxel dimensions of 0.2 x 0.2 x 0.05 cm^3 for the first 2 cm, followed by 0.2 x 0.2 x 0.1 cm^3 for the next 2 cm, and finally 0.2 x 0.2 x 0.5 cm^3 for the remainder of the phantom. DOSXYZnrc runs were done for the carbon beams as well as the 6 MV therapeutic beam. The resulting 3ddose files were read into MATLAB to calculate PDD data as before.

The depth dose was then extracted from the resulting absolute dose matrix and normalized to D_{max}. Doses from various low-Z beams were then added to the nominal 6 MV beam by normalizing the distributions and performing a weighted summation. The

resulting variability and functionality of these combinations are described in the next chapter.

3.4 Low-Z Target Beam Production

This research was experimentally verified using physical versions of the carbon targets, which were ordered from Machining Solutions in Ontario, CA. Target holders were machined on-site from aluminum, in order to be placed into a non-clinical Varian 2100C linear accelerator (which has no structural difference from the simulated 2100EX) available and maintained at the NSCC for research purposes. Upon arrival, each target thickness was measured at room temperature using a micrometer and the resulting measurements with the percent error are shown in Table 3-3. The measurement error on the micrometer was ± 0.000254 cm. Each target had a diameter of 4 cm. Targets and target insertion are shown in Figure 3.3.

Table 3-3: Requested and actual thicknesses for ordered carbon targets, as well as % error for 15, 30, and 60 % CSDA.

%CSDA	2.5 MeV MC thickness (cm)	2.5 MeV Thickness (cm)	% Error	4 MeV MC thickness (cm)	4 MeV Thickness (cm)	% Error
15	0.1073	0.10795	0.61	0.1752	0.17755	1.34
30	0.215	0.21666	0.77	0.3504	0.35204	0.47
60	0.4293	0.42850	0.19	0.7008	0.70180	0.14

Figure 3.3: Left: Manufactured carbon targets in their aluminum holders. Right: Low-Z target being installed in the carousel of a Varian 2100 C linac.

The low-Z targets were incorporated into the accelerator by placing three of the series into unused ports of the carousel. A diagram of the carousel and its port positions/contents is shown in Figure 3.4. To reach the carousel, all covers of the head of the linac and one lead shielding-block were removed. Targets were housed with their surface flush to the surface of the carousel, this leaves potential for the electron beam to scatter due to an $\sim$ 3 cm air gap between the beryllium window and the target[23]. Adjustment of the target height did not need to be corrected for the purposes of this research, as previous work found this to mainly affect the focal spot size and image resolution[23], which are not beam properties we are concerned with. The linac was operated in electron mode, in which the primary target was retracted, and manually selecting the carousel port housing the low-Z target. Manual selection is achieved by accessing the carousel-mode/BMAG board in the linac cabinet. A three-way switch in the gantry stand allows the carousel to be manually operated, and the port is then chosen by a rotary dial/potentiometer located on the same board. An indicator shows the current port in the accessible position at the front of the linac, the port directly opposing will be in the beam-line.

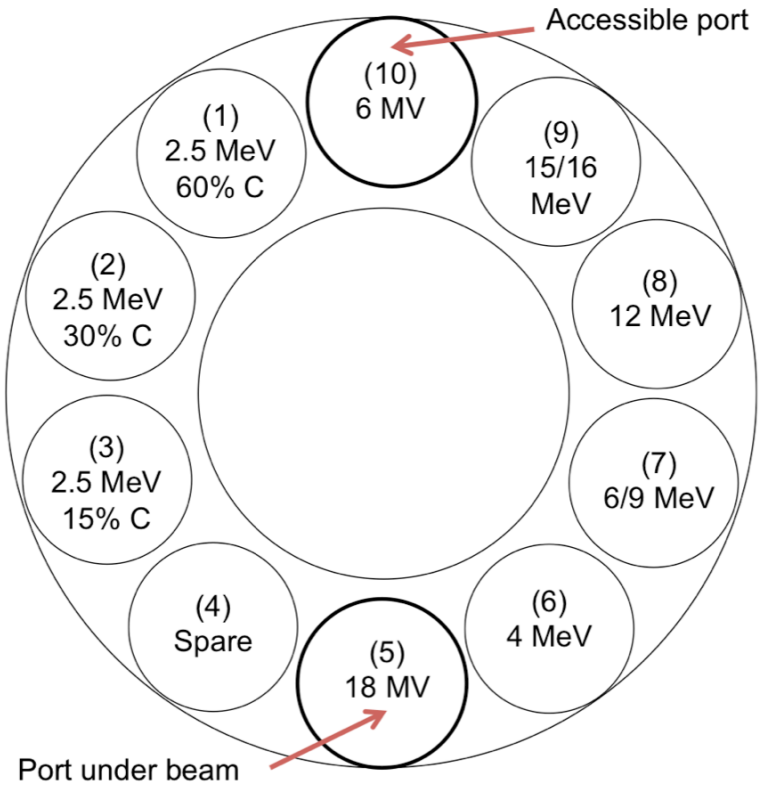

Figure 3.4: Schematic of carousel within the 2100 C. The ports and their contents are labeled.

The low-Z targets were inserted into the 1st, 2nd and 3rd spare ports, leaving the 4th empty. Brass caps originally covered the spares, but these were removed to place the targets.

3.4.1 Beam Energy Determination

Before any beam measurement of beam-line data could be made, the linac had to be tuned to the same energies used for the low-Z simulations, 2.5 and 4 MeV. Simulations of a standard 2100EX beam-line with a 4 MeV tantalum electron scattering foil were run through BEAMnrc with source energies of 2.5 and 4 MeV. The resulting phase spaces

were then run through DOSXYZnrc to create reference PDD curves that correlate with the source energies of 2.5 and 4 MeV.

The 2100C did not have a 4 MeV program board equipped at the commencement of this research, thus a dedicated 4 MeV research board was installed to allow operation within this energy range. To tune the beam energy down from the nominal operating point for a 4 MeV beam to a 2.5 MeV beam, the bending magnet shunt current was adjusted to achieve lower energies. The bending magnet current was adjusted on the BMAG board within the linac cabinet. By adjusting the bending magnet current, the mean energy of the exiting electrons can be tuned to a particular energy selection. A slit within the bending magnet of the linac stops electrons not meeting the energy selection.

The linac was first tuned to 4 MeV. The dose servos were turned off for the duration of the experiment, as they had undesired effects during tuning. The beam tuning procedure developed during previous research was initially followed as a guide during the beam tuning process[27]. Three parameters were manipulated to achieve the desired energy setting: the gun High Voltage (HV), the grid voltage, and the pulse forming network voltage (PFNV). In previous research, only two of these parameters were manipulated: the gun HV and the grid voltage. As the 2100C is an older machine than the 2100EX, the method had to be adjusted, since in the 2100C, manipulating the RF driver reaches a negligible effect before beam settings can be achieved, thus limiting the effectiveness of manipulating the grid voltage. Corse setting of the gun HV and grid voltage was done on the gun deck of the linac, after which fine-tuning of the grid

voltage could be performed using the 'gun-I' potentiometer on the 4 MeV board in the console. On the 2100C, the main parameter used to fine-tune the beam was the PFNV, which determines the klystron pulse frequency and amplitude. The steps used during the beam tuning process were as follows: first, the bending magnet current was set to an appropriate range, a PDD scan was taken to determine whether the energy selection value was close to that of the desired energy, if not the current was adjusted again, if found to be close, the rep rate was fine tuned by adjusting the PFNV set points on the 4 MeV board outside the room. After each adjustment of the parameters, a PDD scan was preformed to quantify the changes. This process is visualized in Figure 3.5. Once the PDD was matched to the MC simulated results, it was determined that the desired beam energy was reached and the low-Z targets were manually moved into the beam-line to record PDDs of the low-Z beams.

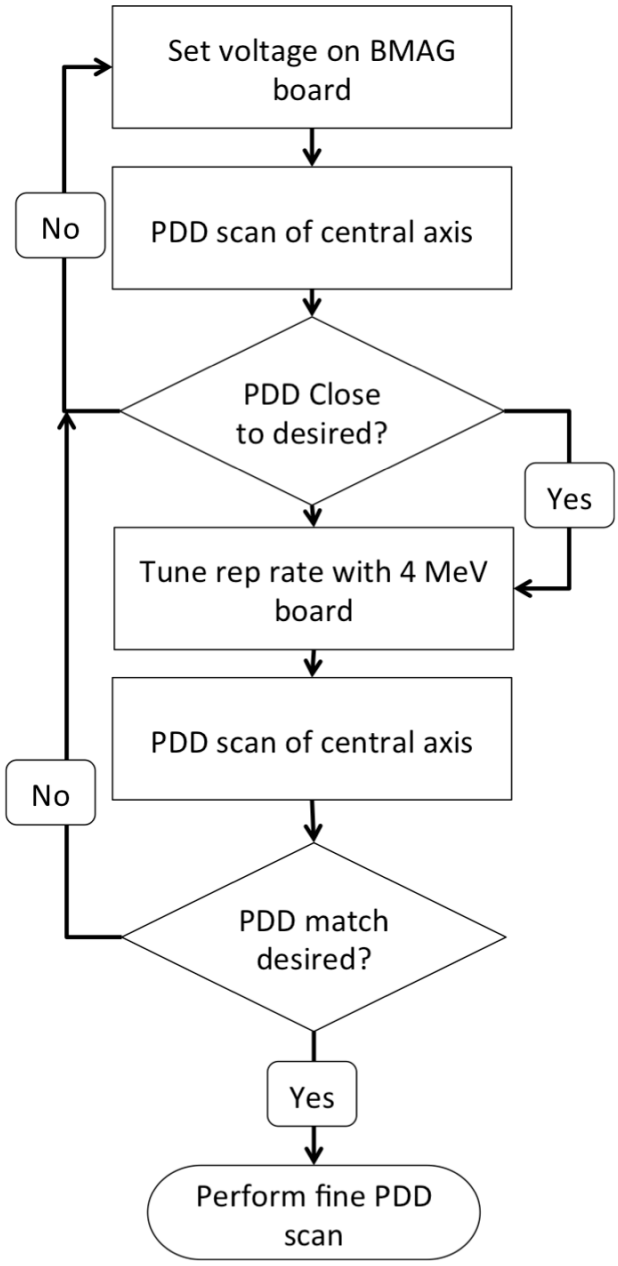

Figure 3.5: Flow chart of beam tuning process.

The 4 MeV BMAG board is originally configured to operate under a limited gun HV range (~ 9.1 – 9.3 V) thus it had to be modified to be able to achieve the second energy setting of 2.5 MeV. During previous research[27], the 4 MeV BMAG board of a Varian 2100EX was modified to allow lower energies, and these modifications were used

on the Varian 2100C machine used in our experiments. The changes consisted of adding resistors to the 10 kΩ programming and interlock potentiometers. These changes allowed the BMAG interlock to be removed when lower energies were desired, and the change to programming allowed a larger gun HV range of operation. After these modifications, the tuning of the 2.5 MeV beam followed the same procedure as the 4 MeV beam. The dose rate used for each beam was ~400 MU/min.

3.4.2 Beam Measurements

To measure the beam-line output and quantify the data, a 50 x 50 x 50 cm^3 scanning water tank (Blue Phantom, IBA Dosimetry, Schwarzenbruck, Germany) was used. An electron field diode (EFD) (EFD 3G, IBA, Schwarzenbruck, Germany) that is a pSi semiconductor that provides direct electron depth dose was used, as discussed in chapter 2. The active volume of the diode has a diameter of 2 mm, a thickness of 0.06 mm, and an effective measurement point of < 0.9 mm from the top of the detector. The diode was vertically positioned in the holder. The water surface of the tank was set at 90 cm SSD.

The tank was controlled in room by an external pendent that fed into a common control unit to which the EFD detector was also connected. Ethernet was used to connect this control unit, via a USB converter, to a laptop outside the bunker. Using the laptop, the tank could be controlled via the program Omnipro-Accept (IBA, Schwarzenbruck, Germany). This software can be used to set up various PDD and profile collections.

The set up of the linac matched that used for the MC simulations, including the 10 x 10 cm^2 field size set by the jaws. The measurements were recorded in 0.2 mm intervals, and matched to the MC PDD curves of known energy and low-Z beams. After initial collection of the PDD, data was transferred into Excel and normalized to the maximum reading before being compared to MC data. All carbon beam variations of 2.5 and 4 MeV were measured separately.

CHAPTER 4 RESULTS AND DISCUSSION

4.1 TARGET DESIGN

4.1.1 Fluence Spectra

Figure 4.1 displays the cumulative spectral results for carbon targets of 15, 30, 60% CSDA thickness at 2.5 MeV electron mode, and a 100% CSDA thickness at 2.35 MV photon beam. The 2.35 MV data was gathered during previous research and is shown as a comparison for 100% R_{CSDA} of carbon[27]. The combined electron/photon spectra show two distinct peaks in differing energy ranges, a low energy peak and a mid to high energy peak. This plot does not deliver much information of the individual spectra; it only serves to provide a view of the combined spectra.

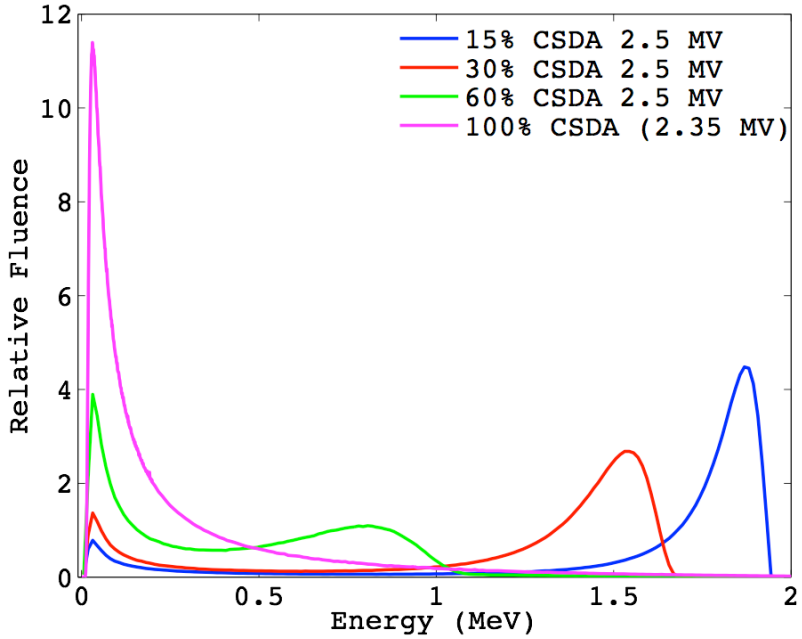

Figure 4.1: Calculated spectral distribution for various %CSDA of carbon targets in a 2.5 MeV electron beam-line. Spectra are captured upon the exit of the linac head, including electron as well as photon data, and each is normalized by their own area.

In Figure 4.1 it can be seen that the relative fluence spectra of the thinner targets vastly differs from that of the 100% CSDA carbon target and nominal 6 MV beam. As the thickness of the target is decreased, a second fluence peak appears within the higher energy range, and progressively increases in both relative fluence and energy as the low energy fluence peak decreases.

The majority of the particles in the 100% R_{CSDA} spectra are below 250 keV, and the initial peaks of the 12, 30, and 60% R_{CSDA} largely falloff by this point. The high energy peaks displayed in the spectral data for 60, 30, and 15% R_{CSDA}, occur around 0.8, 1.54, and 1.87 MeV, respectively. It is known that the 100% R_{CSDA} and nominal 6 MV are composed entirely of photon contributions since both targets are designed to be thicker than the range of electrons of their respective energies. Hence, the high energy peaks within 60, 30, and 15% R_{CSDA} are due to primary and secondary electrons escaping through the target with a progressively increasing fluence. This was confirmed by analyzing the photon and electron fluence contributions individually through Monte Carlo simulations. Figure 4.2 shows the full spectral distribution for a 2.5 MeV electron beam bombarding a carbon target of thickness 30% R_{CSDA} in order to show contributions from all particle types (a), along with the photon contribution alone (b), and the electron contribution alone (c). These fluence spectra show that the first fluence peak is due solely to photon contributions, and the secondary peak due to electron contributions. The mean of the photon spectrum is 287 keV and the peak at 31.2 keV, while the electron spectrum has a mean of 1.42 MeV and the peak occurring at 1.54 MeV.

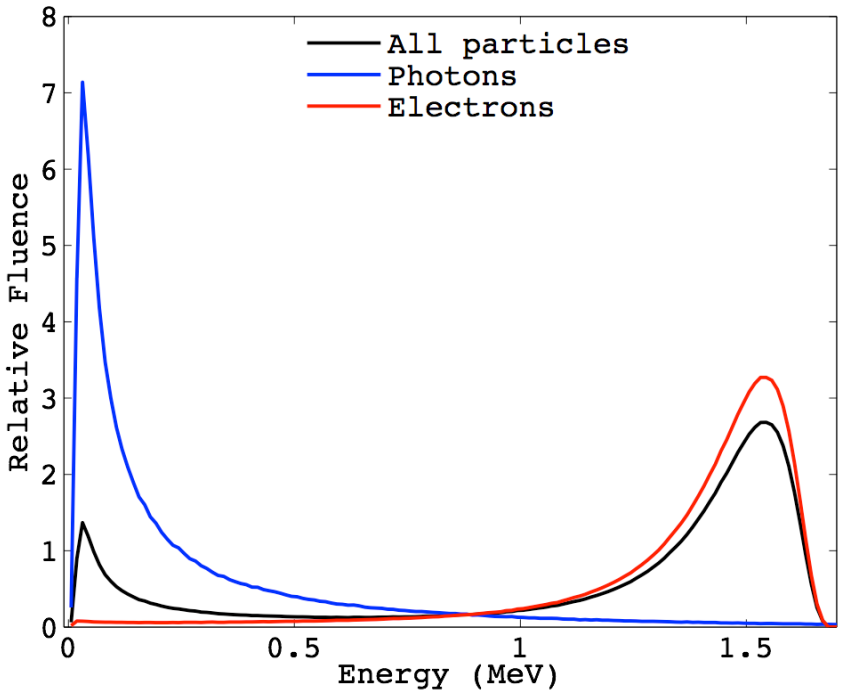

Figure 4.2: Decomposition of 30% R_{CSDA} carbon target spectra. Spectra are captured upon the exit of the linac head, and each is normalized by their own area.

The final fluence spectra comparisons between all target material results are shown in Figure 4.3 – Figure 4.6. In (b) and (c) of each figure, the spectra are normalized in such a way that each area under the curve is equal to 1.0, thus the total fluence for each curve is equivalent. Figure 4.3 features all fluence spectra for 15% R_{CSDA} targets. At 15% CSDA thickness, the electron fluence dominates the spectra with an energy range of 1.5 to 1.96 MeV, while the photon fluence remains prevalent below 250 keV. Beryllium produces the highest electron fluence, followed by carbon, aluminum, and copper. Each peak in the electron fluence is centered on the nominal energy for the 2.5 MeV incident beams. The nominal energy ranges from 1.86 – 1.88 MeV for each material, with Cu being the low range and Be representing the uppermost range. The ordering of the electron fluence for each material does not stem from the respective

collisional stopping power of each material (see Figure 4.4). If stopping power were relevant carbon and aluminum would show a more significant contribution. There is a minor variation in the electron fluence peaks, which is likely due to secondary electron contribution. A similar trend appears in the photon spectra. Be and C produces soft beams with not much self-absorption of the low energy photons by the target material. Their spectral similarity stems from the closeness of their atomic numbers: Z = 4 for Be and Z = 6 for C. As Z increases, so too does the prevalence of photoelectric interactions, and, thus, self-absorption of the low energy photons within the target. This is evidenced by in the Cu spectra and slightly within Al.

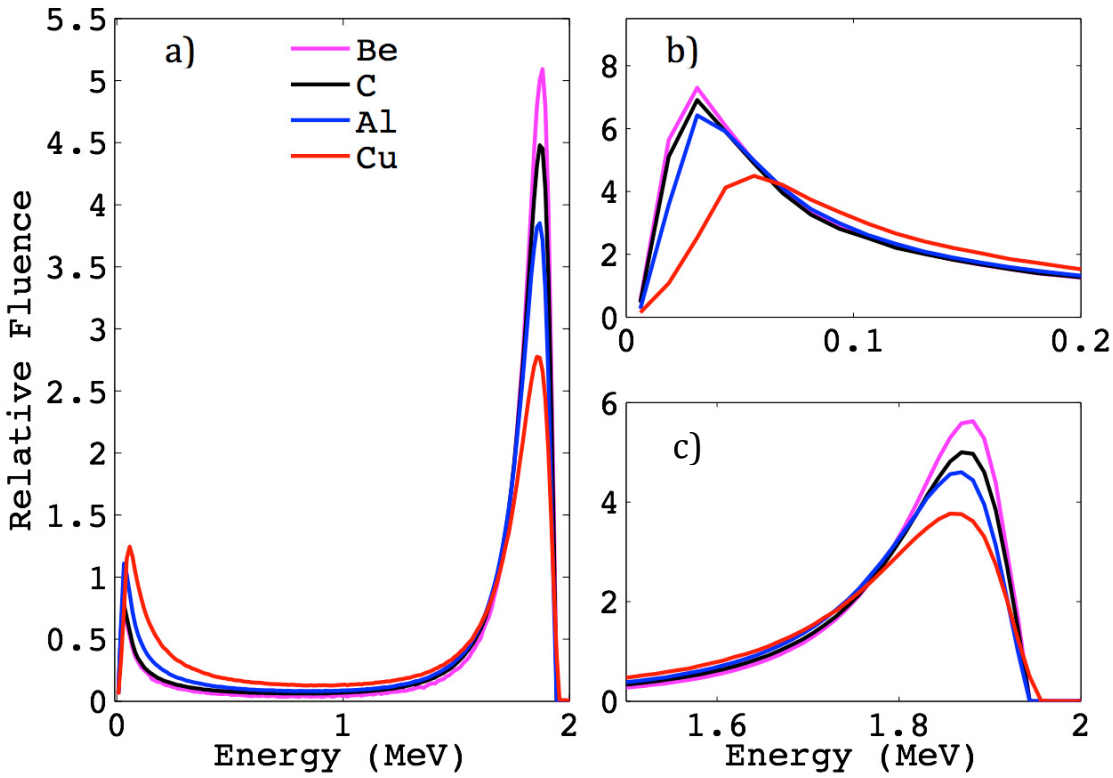

Figure 4.3: Spectral distribution for all target materials in a 2.5 MeV electron beam-line and 15% CSDA thickness. Spectra are captured upon the exit of the linac head, and each is normalized by their own area. A) relative fluence of all particles, B) relative photon fluence, C) relative electron fluence.

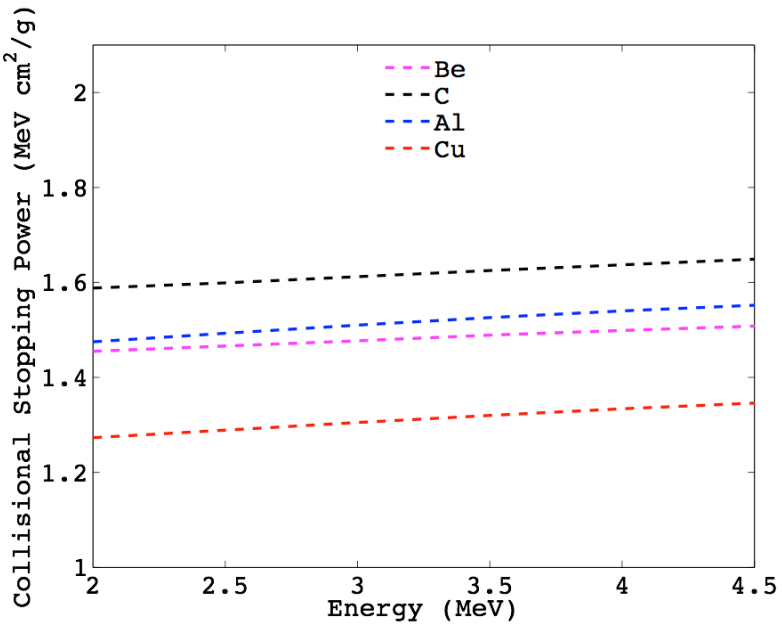

Figure 4.4: Collisional stopping power vs. Energy for each target material.

Figure 4.5 shows the spectral distributions for 30% R_{CSDA} of all target materials of interest. Between the 30% and 15% R_{CSDA}, the photon fluence below 200 keV has increased 1.5% for carbon and decreased by 3.1% for copper, while the electron fluence peak followed a similar trend (carbon increasing by 6.1% and copper decreasing by 5.4%). The entire electron energy range shifted from 1.6 – 1.9 to 1.2 – 1.63 MeV. The photon peak of copper shifted from 56 keV for 15% R_{CSDA} to 69 keV for 30% R_{CSDA}, whereas Be and C stayed at 31.2 keV and Al shifted from 31.2 to 35 keV. Thicker targets produce harder beams within the low energy photon spectra for higher Z materials, because there are more bremsstrahlung events from primary and secondary electrons, therefore, more photon production resulting in decreasing electron fluence. As copper is the highest Z material, the probability of hard collisions increases due to an increased interaction cross-section. These interactions produce photons of a higher energy. More

kinetic energy is lost in higher Z materials, shifting the electron peaks. Be and C peak at 1.54 MeV, Al peaks at 1.51 MeV and Cu peaks at 1.48 MeV.

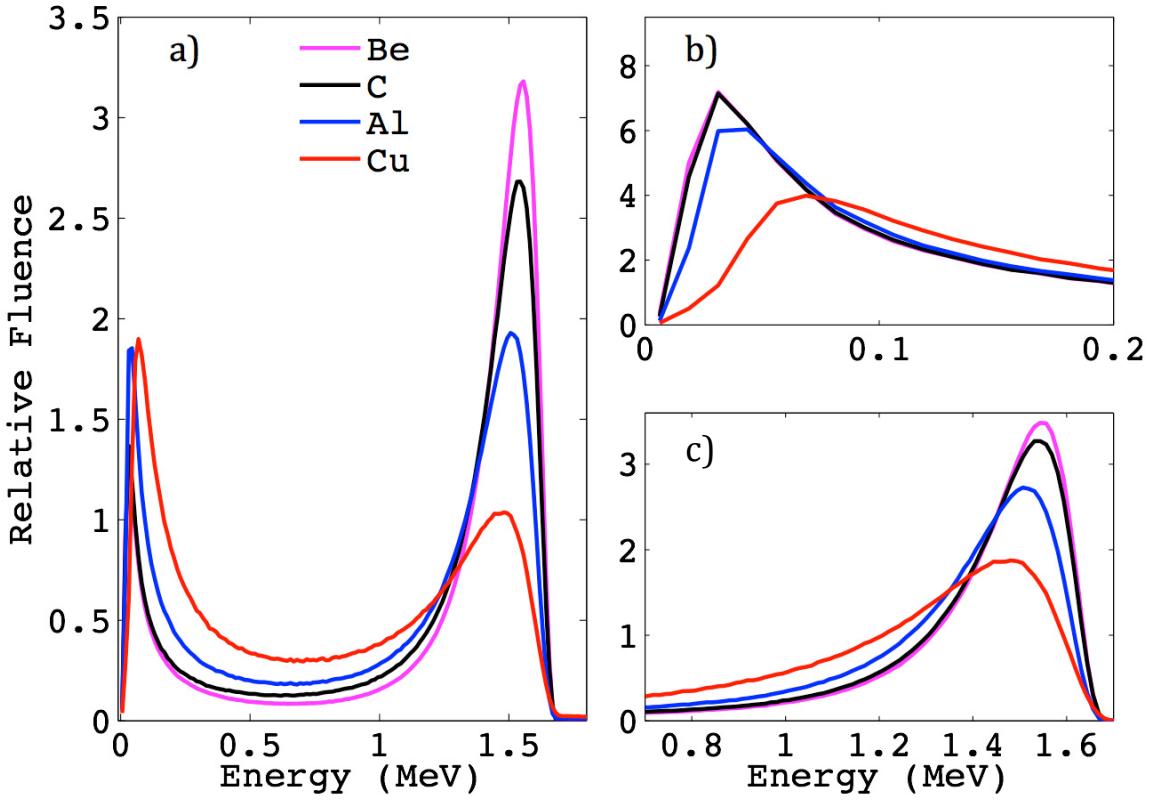

Figure 4.5: Spectral distribution for all target materials in a 2.5 MeV electron beam-line and 30% CSDA thickness. Spectra are captured upon the exit of the linac head, and each is normalized by their own area. A) relative fluence of all particles, B) relative photon fluence, C) relative electron fluence.

Finally, Figure 4.6 shows the spectral distribution for the various target materials with a R_{CSDA} of 60%. The photon peaks occur at approximately 31, 31, 44 and 94 keV for beryllium, carbon, aluminum and copper, respectively. The energy of electrons have been greatly reduced to between 0.5 – 1.08 MeV. In the higher-Z materials, aluminum and copper, the electron contribution to the overall fluence is minimal. Significant loss in kinetic energy shifts the electron fluence peaks to approximately 85.6, 80.6, 70.6 and 64.4 keV for Be, C, Al and Cu, respectively.

Figure 4.7 shows a comparison of the 60% R_{CSDA} spectra for carbon and copper, respectively. Carbon and copper were chosen as representative elements as it was found that carbon and beryllium follow the same trend, while copper and aluminum follow the same trend although coppers results are exaggerated. It is evident that the copper spectrum has less of an electron component than that of the carbon (indicated by the degree of noise evident in the curve), signifying a diminished number of electrons leaving this target as opposed to carbon. In higher atomic number materials of this target thickness, and energy, a significant component of primary and secondary electrons within the target lose the majority of their energy to bremsstrahlung, and do not contribute to the beam exiting the linac. The electron contribution can be seen in the overall fluence spectra as a slight increase between 0.5 and 1 MeV that rises above the photon spectra before overlapping it again at 1 MeV (see Figure 4.7). Each spectra component is normalized by its own area.

Analysis of these spectra indicates that beryllium or carbon will be the material of choice for our target. These materials have consistent low energy photon fluence peaks, and defined electron energy peaks, of higher relative fluence, that vary with target thickness. The variable energy of the electron contribution for each target thickness will allow for beams of varying penetration ability. Although a definite choice of material cannot be made until the PDD curves are analyzed. Electrons within the presented energy ranges will significantly contribute to surface dose. Considering that the practical range of electrons can be estimated as ½ the energy, the furthest these electrons will travel within the tissue is < 1 cm.

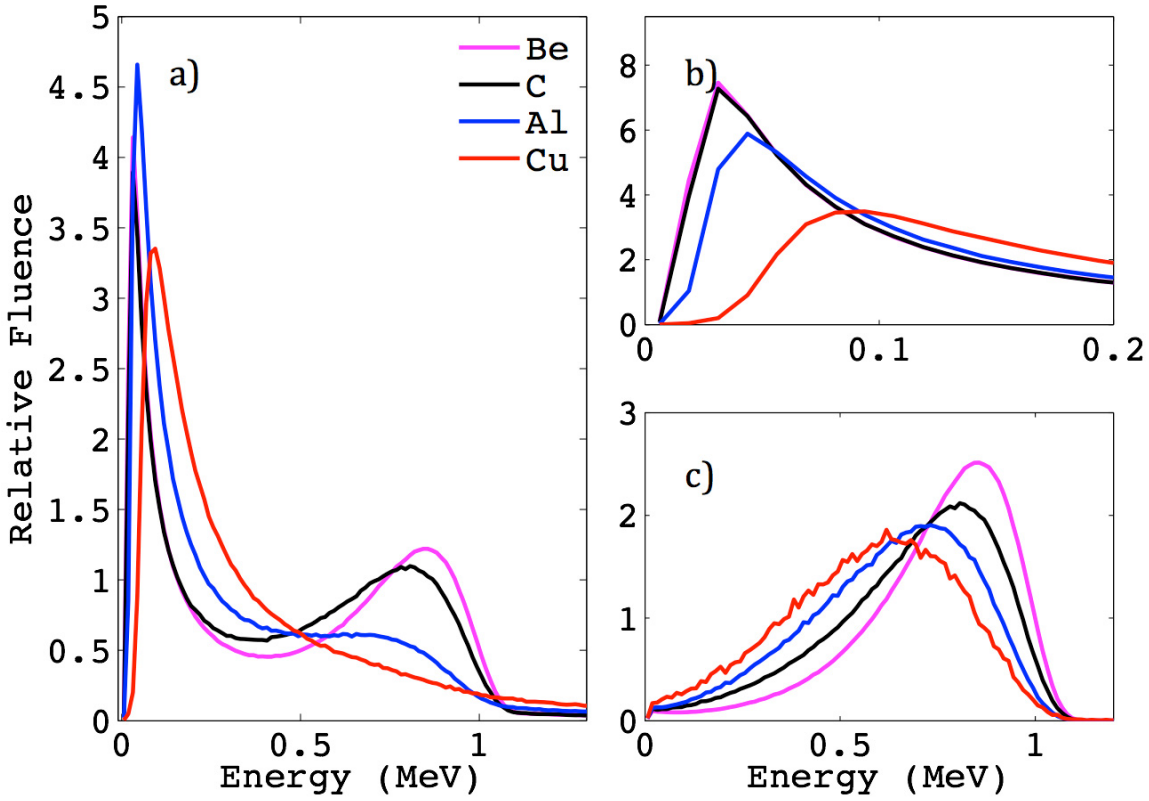

Figure 4.6: Spectral distribution for all target materials in a 2.5 MeV electron beam-line and 60% CSDA thickness. Spectra are captured upon the exit of the linac head, and each is normalized by their own area. A) relative fluence of all particles, B) relative photon fluence, C) relative electron fluence.

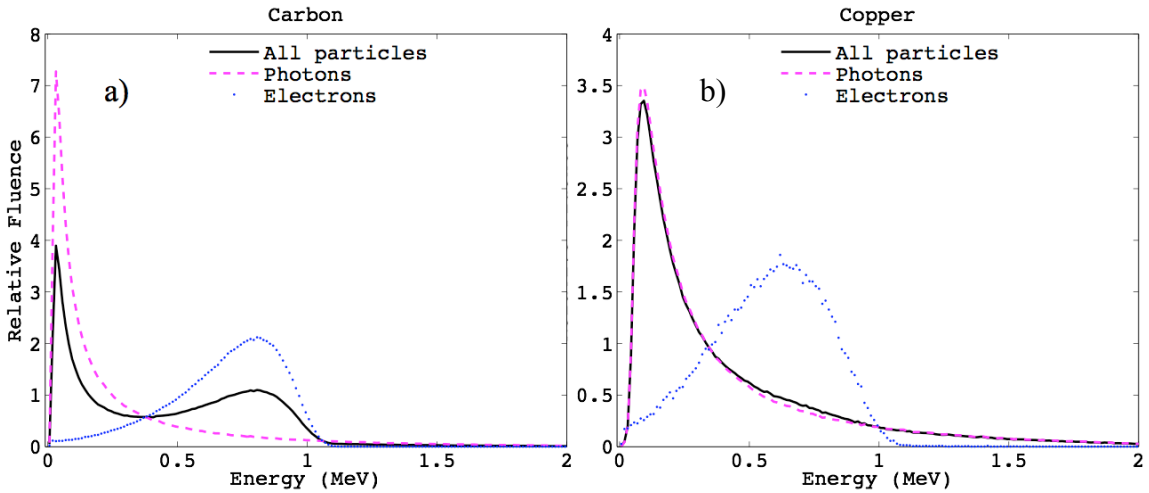

Figure 4.7: Comparison of fluence spectra for 60% R_{CSDA} of a) carbon, and b) copper. In each spectra the overall, photon only and electron only fluence are shown.

Table 4-1: Radiological parameters for each material of interest at 2.5 and 4 MeV.

Target Material & Energy (MeV)		Radiation Yield	Stopping Power (MeV·cm^2/g)	Collisional Stopping Power (MeV·cm^2/g)	Radiative Stopping Power (MeV·cm^2/g)	CSDA (g/cm^2)
Be	**2.5**	5.8x10-3	1.484	1.47	1.8x10-2	1.57
	4	9.8x10-3	1.531	1.5	3.2x10-2	2.56
C	**2.5**	8.5x10-3	1.628	1.6	2.9x10-2	1.43
	4	1.4x10-2	1.688	1.64	5.0x10-2	2.34
Al	**2.5**	1.81x10-2	1.549	1.49	5.6x10-2	1.55
	4	2.92x10-2	1.637	1.54	9.7x10-2	2.49
Cu	**2.5**	4.3x10-2	1.405	1.29	1.2x10-1	1.75
	4	6.7x10-2	1.53	1.33	2.0x10-1	2.77

4.1.2 Dose Distribution Within a Water Phantom

The MC calculated PDD curves for each material and R_{CSDA} are shown in Figure 4.8 – Figure 4.11. Inspection of each figure indicates similar PDD curves for 15% and 30% R_{CSDA}, with 60% R_{CSDA} showing differences in photon contribution between each target material. In each material, d_{max} occurs at 0.075, 0.225, and 0.325 cm for 60, 30 and 15% R_{CSDA}, respectively, and the surface dose ranges from 83 – 88, 64 – 70, 62 – 66, for 60, 30 and 15% $R_{CSDA,}$ respectively. The most notable variation between the PDDs is bremsstrahlung radiation contribution, which appears to increase with atomic number of the material. The uncertainties shown on the PDD curves were determined within DOSXYZnrc.

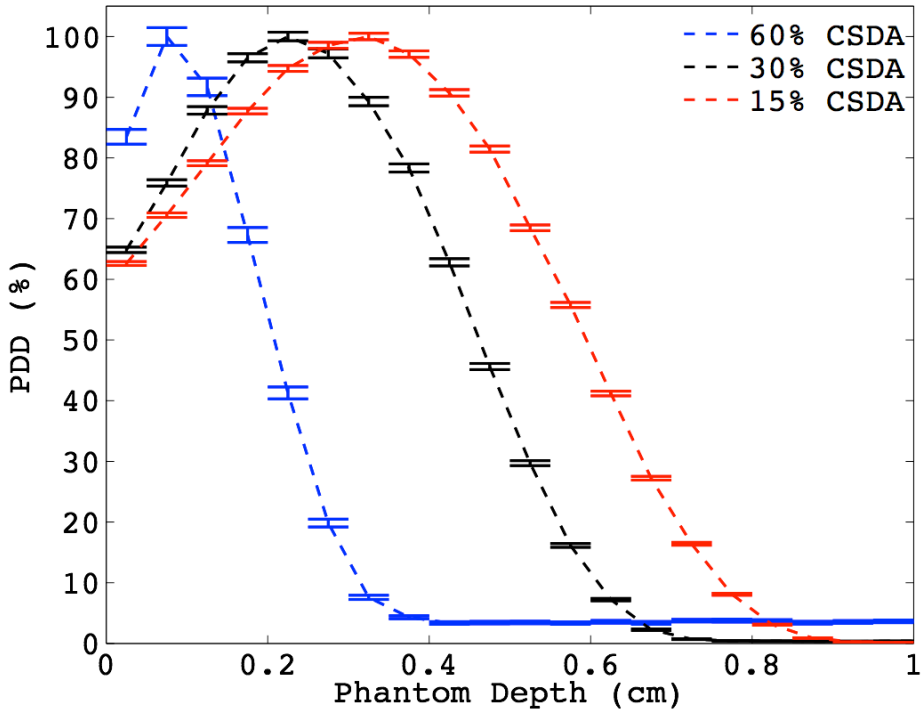

Figure 4.8: Monte Carlo calculated PDD curves for beryllium targets at 15, 30, 60% R_{CSDA} and 2.5 MeV. Each curve is normalized to its respective D_{max}.

Figure 4.8 shows the PDDs for various beryllium targets. Only 60 % R_{CSDA} has a bremsstrahlung tail, which sits at approximately 3.5% dose. Carbon is featured in Figure 4.9. The characteristics of carbon's PDD curves match beryllium within 1-2% for surface dose and bremsstrahlung contribution.

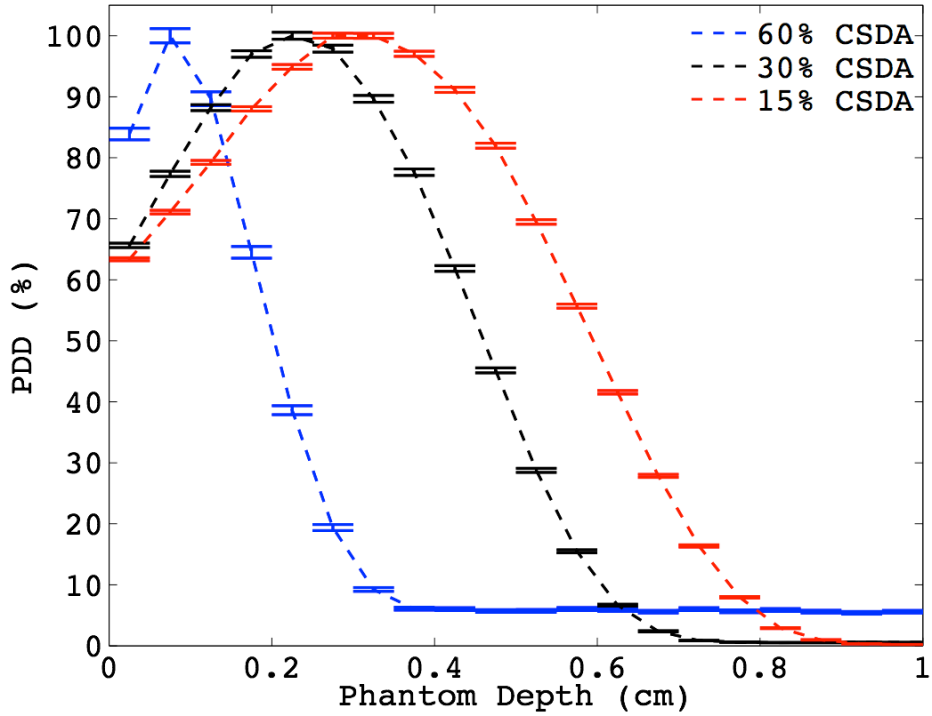

Figure 4.9: Monte Carlo calculated PDD curves for carbon targets at 15, 30, 60% R_{CSDA} and 2.5 MeV. Each curve is normalized to its respective D_{max}.

Aluminum and copper present a drastically increased bremsstrahlung contribution for 60% R_{CSDA} compared to the lower Z counterparts, with Al and Cu at 20% and 75%, respectively, compared to C and Be's respective, 5.7% and 3.5%. This result was predicted by the fluence spectra discussed in the previous section. As the low-Z targets increase in thickness and atomic number, the photon fluence increases and will contribute to a larger portion of dose distribution. This is especially noticeable in Figure 4.11 as the resulting PDD is dominated by the photon contribution, so much so that the electron contribution is indistinguishable within the combined PDDs unlike all other PDDs presented in this work.

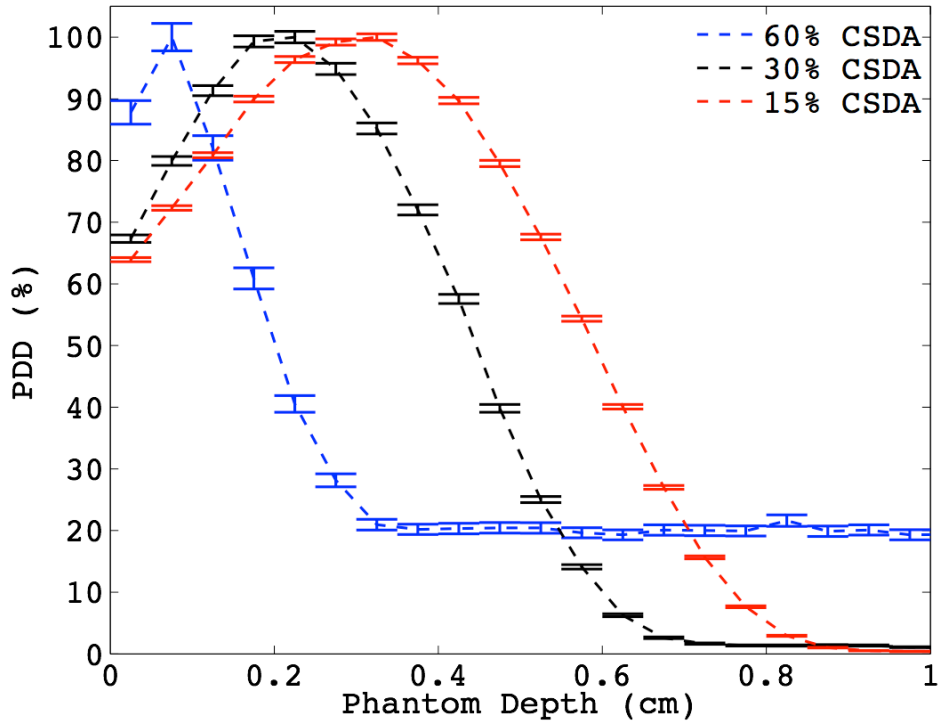

Figure 4.10: Monte Carlo calculated PDD curves for aluminum targets at 15, 30, 60% R_{CSDA} and 2.5 MeV. Each curve is normalized to its respective D_{max}.

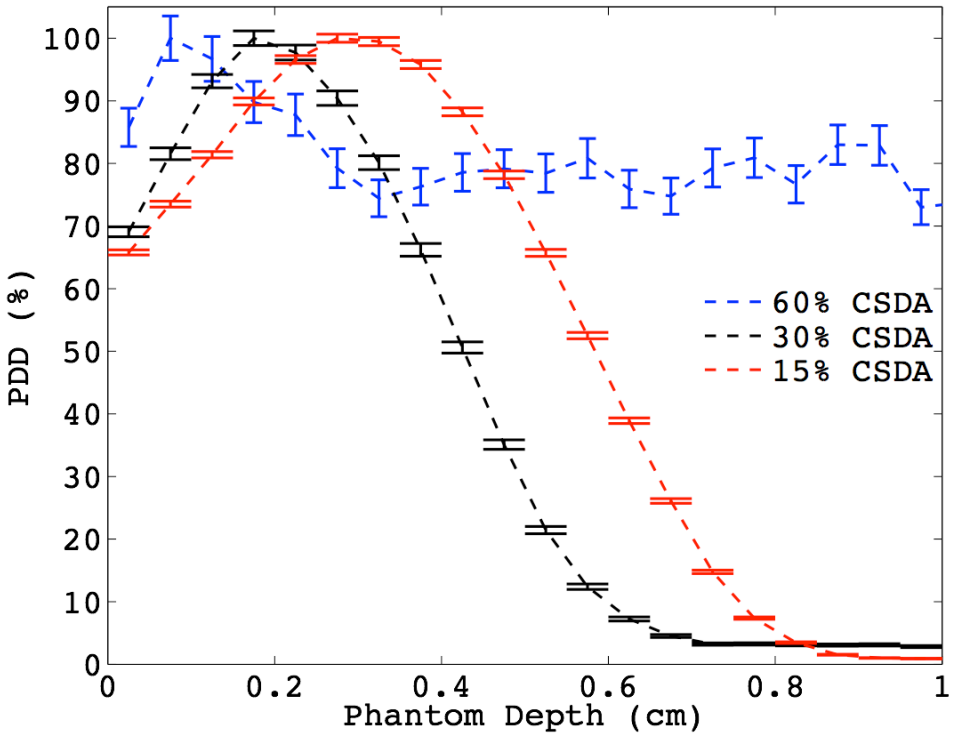

Figure 4.11: Monte Carlo calculated PDD curves for copper targets at 15, 30, 60% R_{CSDA} and 2.5 MeV. Each curve is normalized to its respective D_{max}.

The proportional contribution of the 60% R_{CSDA} copper beam, in the summation shown in Figure 4.12, can be determined by plotting separate electron and photon PDDs and weighting them relative to the D_{max} of the combined PDD. The result of this is shown in Figure 4.12, and shows that after the superficial dose spike caused by low energy electrons, the dose falloff mirrors that of the photon PDD. This will also be true of the lower atomic number materials of Be, C and Al.

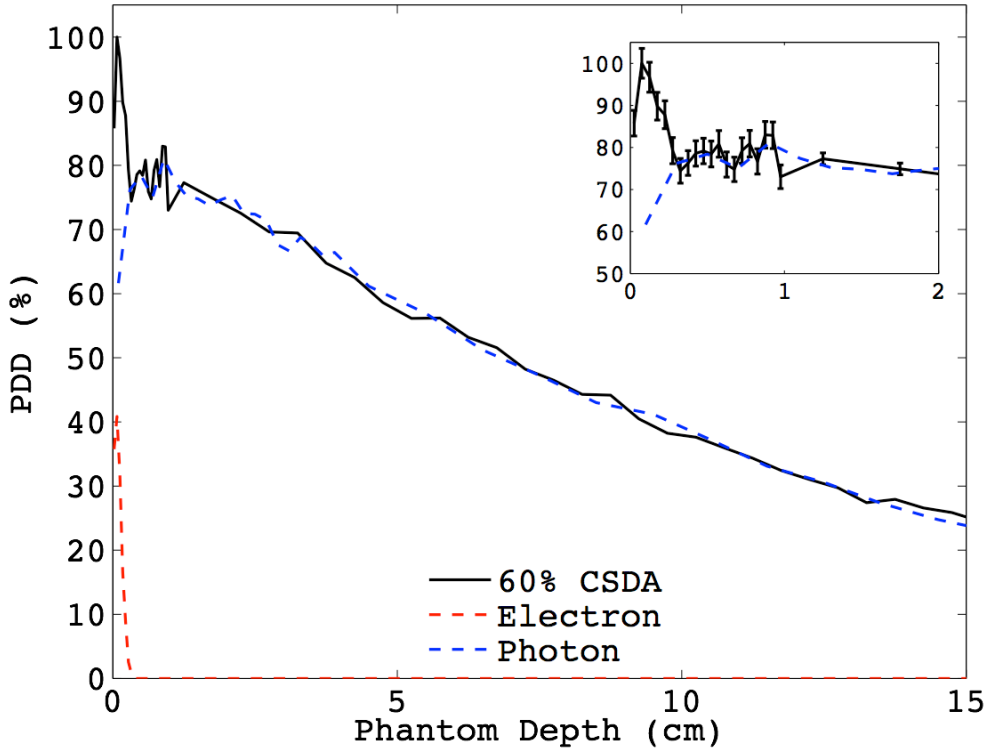

Figure 4.12: Monte Carlo calculated PDD curve for copper target at 60% R_{CSDA} and 2.5 MeV is shown in black. The MC calculated electron (red) and photon (blue) PDD curves are overlaid on top of the combined PDD. Each curve is normalized to the D_{max} of the combined PDD. The insert shows the associated error with the combined PDD.

Figure 4.13 shows the electron and photon contributions for 60% R_{CSDA} carbon; the differences between it and copper are remarkable. The photon PDD has a D_{max} of ~

7% and falls off with the combined PDD. The 60% R_{CSDA} PDDs are the only curves with a significant photon contribution.

Figure 4.14 shows component PDDs for 60 and 15% R_{CSDA} of carbon. In the former, it can be seen that the electron contribution is responsible for the majority of the superficial dose distribution with the photons contributing ~ 6% to D_{max}. In the latter, the electron contribution perfectly overlaps the combined PDD, and the photon contribution hovers at ~ 0 with no discernable peaks

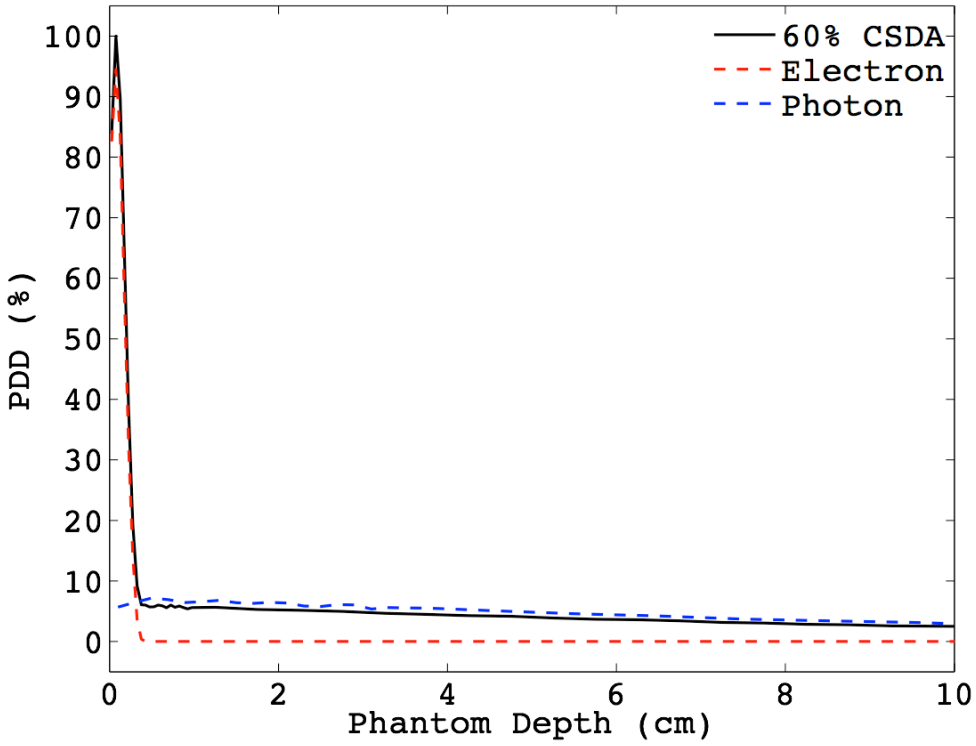

Figure 4.13: Monte Carlo calculated PDD curve for carbon target at 60% R_{CSDA} and 2.5 MeV is shown in black. The MC calculated electron (red) and photon (blue) PDD curves are overlaid on top of the combined PDD. Each curve is normalized to the D_{max} of the combined PDD.

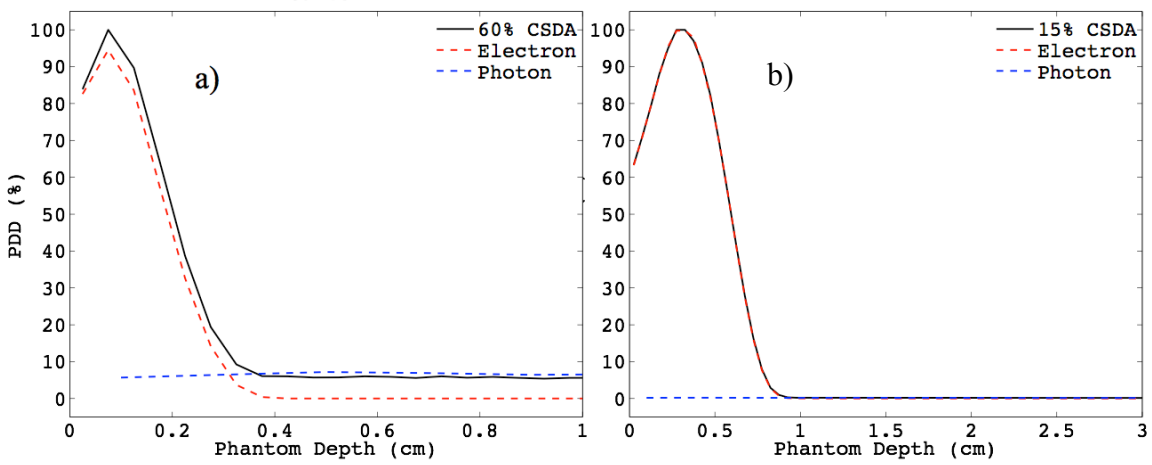

Figure 4.14: Monte Carlo calculated PDD curve for carbon target at a) 60% R_{CSDA} and b) 15% R_{CSDA} (black). The MC calculated electron (red) and photon (blue) PDD curves are overlaid on top of the combined PDD. Each curve is normalized to the D_{max} of their respective combined PDDs.

All four materials present a similar result. The d_{max} for all curves is within a margin of error of each other, and the effect of material on percent surface dose, D_S, is almost negligible with the max difference being ~ 4.3%. However, the bremsstrahlung tail at 60% R_{CSDA} is quite dependent on material and increases with Z. Therefore, it appears that the proposed target can be composed of a singular material, rather than a combination of materials given the PDD similarities.

A strong photon presence, such as that in 60 % R_{CSDA} copper, is not desired in our proposed target, since these beams will be added to a nominal 6 MV therapeutic beam. The therapeutic beam will be responsible for depositing dose at depth, with the low-Z beams serving solely to enhance the surface dose. Enhancement of dose beyond d_{max} (1.5 cm for 6 MV) is not needed. For this reason, aluminum and copper were eliminated as target choices. Another reason to exclude Al is due to its much lower heat capacity,

which increases risk of the target melting when placed in the path of a high-energy electron beam.

The PDD curves of beryllium and carbon are very similar, the only difference being the photon contribution, which is ~2% higher in carbon. With negligible dosimetric differences, the choice of target material was made based on physical and economical properties. Beryllium has a low neutron activation energy, which could have an effect on patient dose if used, it is also a known carcinogenic material and thus difficult and dangerous to machine. However, carbon is not carcinogenic, inexpensive, and is very easy to machine. Carbon was the material of choice.

4.2 Addition of 6MV Therapeutic Beam

To determine whether the proposed low-Z beams would be effective for surface dose enhancement they were added to a nominal 6 MV beam. To achieve this, a 6 MV beam was simulated. The resulting 6 MV Monte Carlo simulation is shown in Figure 4.15, with the associated error of the data displayed in the insert.

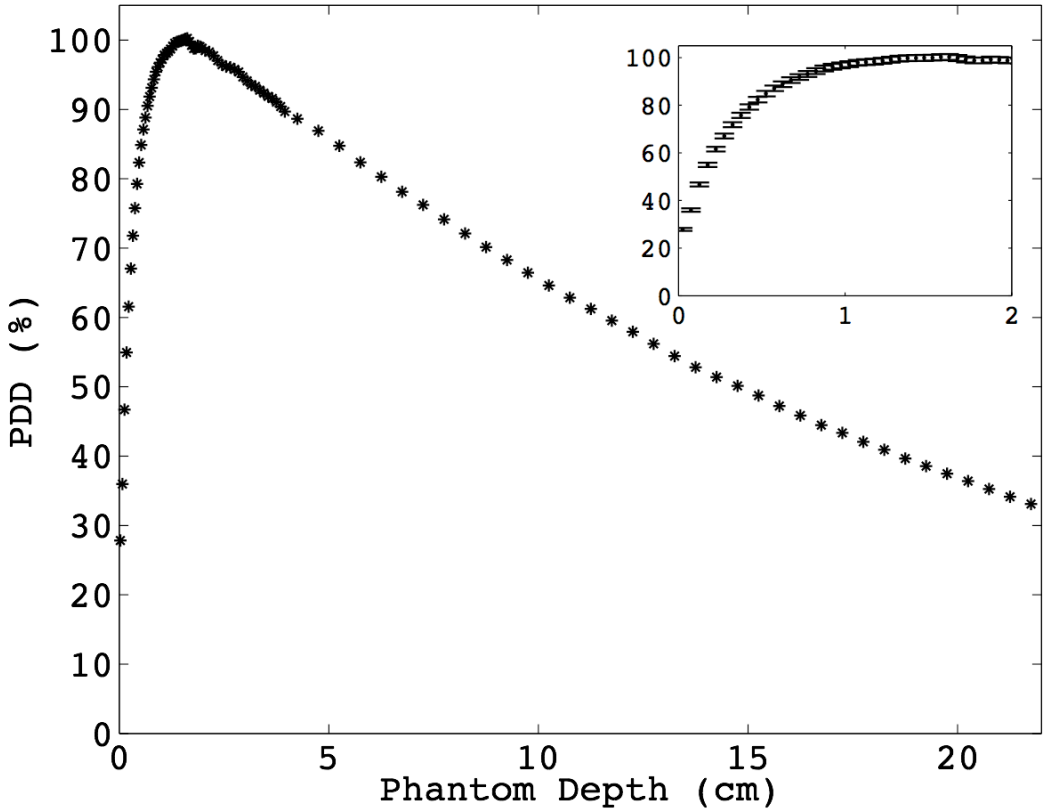

Figure 4.15: Monte Carlo calculated PDD curve for a nominal therapeutic 6 MV beam. The curve is normalized to D_{max}. The insert shows a close up of the first 2 cm of phantom depth, and includes the associated error of data.

Each beam's PDD was normalized to its respective D_{max}. Various combinations of all 2.5 MeV and all 4 MeV PDDs were made, with two being selected to display herein. The two beam summations shown used combinations of 60, 30, 15% R_{CSDA} at 2.5 MeV and 60% R_{CSDA} at 4 MeV.

The goal of the first summation was to produce the highest dose as close to the surface as possible (see Figure 4.16). A close up of the first 1.5 cm is shown in Figure 4.17, including the carbon beam PDDs of R_{CSDA} thickness to indicate how they affect the beam summation when manipulated. The relative weightings in this summation were:

98% of 6 MV, 40% of 60% R_{CSDA} (2.5 MeV), 7% of 30% R_{CSDA} (2.5 MeV), 14% of 15% R_{CSDA} (2.5 MeV), and 8% of 30% R_{CSDA} at 4 MeV. The percentages are relative to the contribution of each beam. Using this combination, the surface dose was increased to 86%, with two slight peaks occurring at 107.5% (0.175 cm) and 105.9% (0.475 cm), before the beam summation merges with the depth dose and falloff of the therapeutic beam at ~1.37 cm depth.

The goal of the second beam summation was to achieve D_{max} between the surface and 1.5 cm (d_{max} of 6 MV). This summation used the following relative weightings: 100% 6 MV, 9% 60% R_{CSDA} (2.5 MeV), 5% 30% R_{CSDA} (2.5 MeV), 5% 15% R_{CSDA} (2.5 MeV), and 9% 30% R_{CSDA} at 4 MeV. Figure 4.18 shows the overall PDD of the combined beam, whereas Figure 4.19 shows the close up of the first 1.5 cm. This beam summation resulted in a combined beam with surface dose of 49.5%, which gradually increases to 100% dose at 0.575 cm, and peaks at 0.875 cm (101%) before merging with the depth dose and falloff of the therapeutic beam at ~1.37 cm depth.

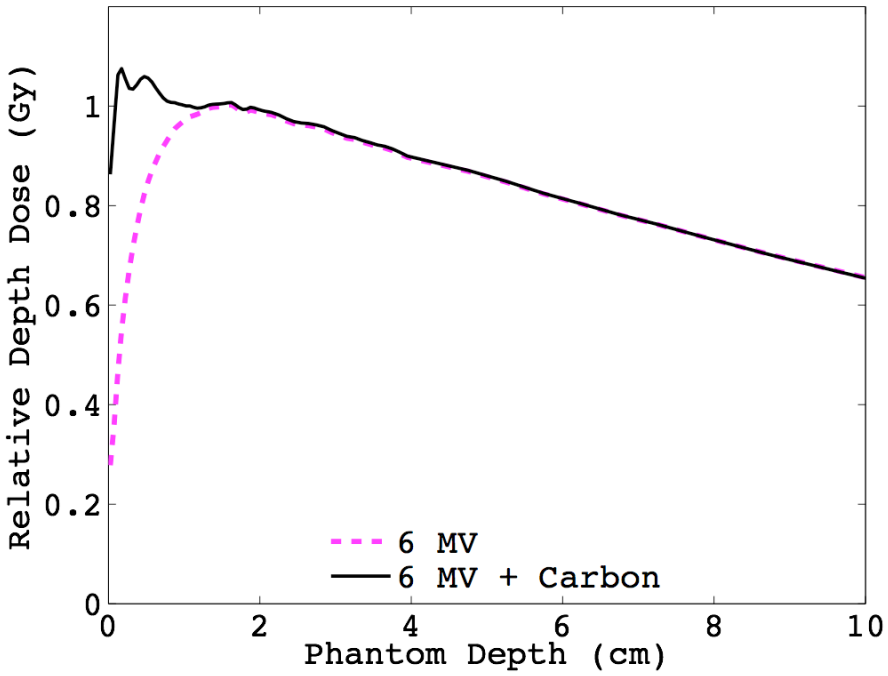

Figure 4.16: Monte Carlo calculated PDD curve for the addition of a nominal therapeutic 6 MV beam with 60% R_{CSDA} (2.5 MeV), 30% R_{CSDA} (2.5 MeV), 15% R_{CSDA} (2.5 MeV), and 30% R_{CSDA} (4 MeV) carbon beams. The curve is normalized to D_{max}.

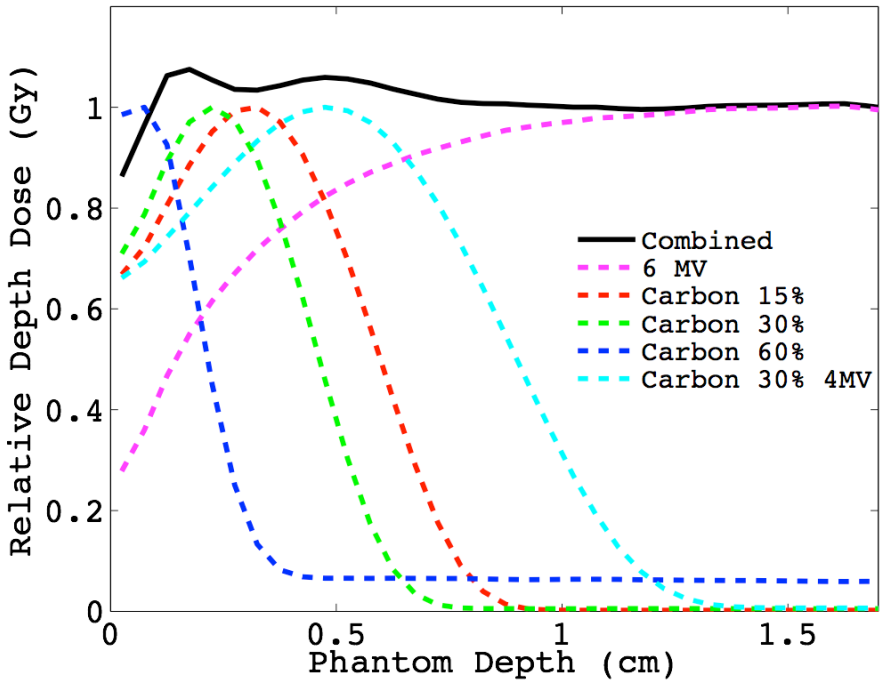

Figure 4.17: Close up of the first 1.5 cm of the previous figure. The carbon beams are overlaid to highlight each beam's contribution at depth. Each beam is normalized to their respective d_{max}.

These beam summations are just two examples that could be achieved using the proposed carbon beams in conjunction with a therapeutic 6 MV beam. These beams allow the surface dose to be specifically tailored and extend a uniform dose distribution from d_{max} to the patient's surface, or any depth required in between.

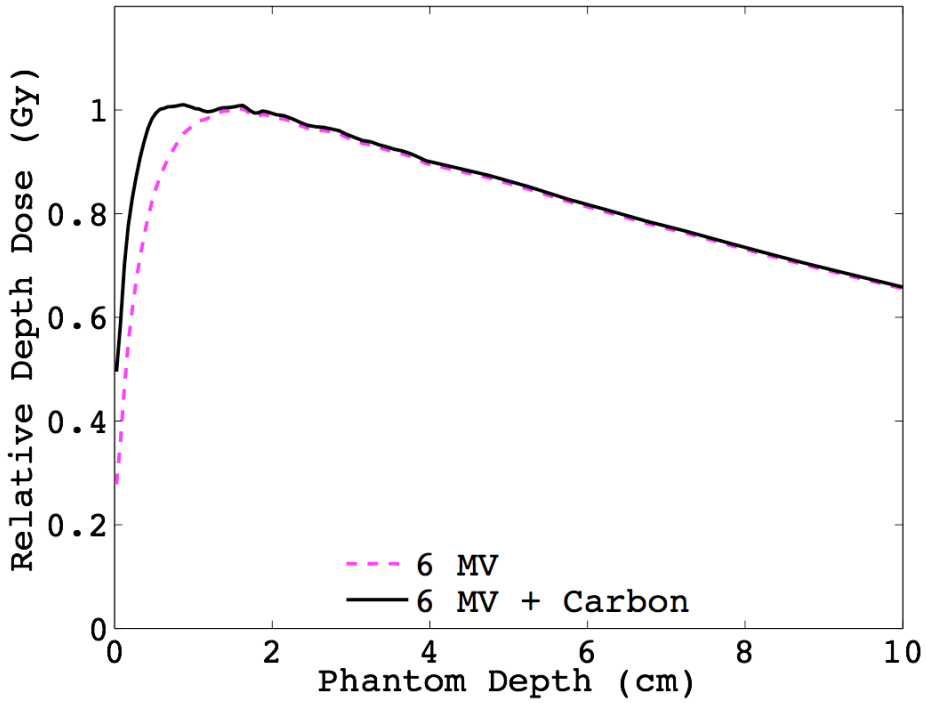

Figure 4.18: Monte Carlo calculated PDD curve for the addition of a nominal therapeutic 6 MV beam with 60% R_{CSDA} (2.5 MeV), 30% R_{CSDA} (2.5 MeV), 15% R_{CSDA} (2.5 MeV), and 30% R_{CSDA} (4 MeV) carbon beams. The curve is normalized to D_{max}.

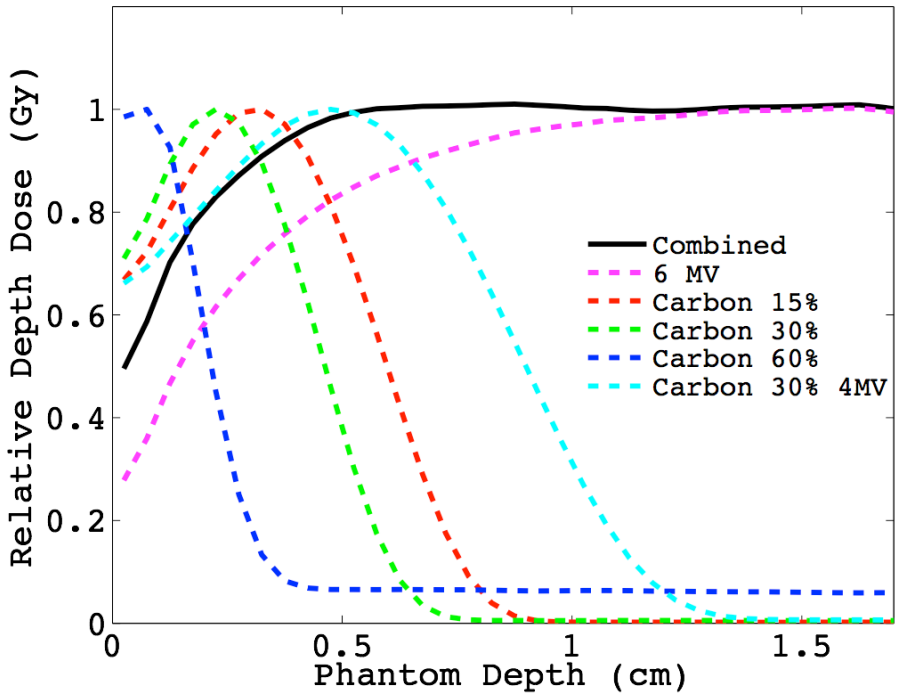

Figure 4.19: Close up of the first 1.5 cm of the previous figure. The carbon beams are overlaid to highlight each beam's contribution at depth. Each beam is normalized to their respective d_{max}.

4.3 Low-Z Target Beam Production

4.3.1 Beam Energy Determination

The first energy to be verified was 4 MeV, the results of which are shown in Figure 4.20. There is good agreement between the MC model and experimental data for tuning the beam energy to 4 MeV using the scattering foil for 4 MeV. The data vary by at most ±5% between the MC and experimental data and the mismatch occurs primarily in the build-up and falloff regions.

The experimental PDD for the 2.5 MeV beam was plotted against the MC data, and the result is shown in Figure 4.21. The maximum difference was found to be 3% in the falloff region.

Both experimental beam energies were found to match those used for the MC simulations using the 4 MeV scattering foil. Thus, the carbon targets could be inserted into the beam-line and each PDD verified with the correct energy of the incident electron beam.

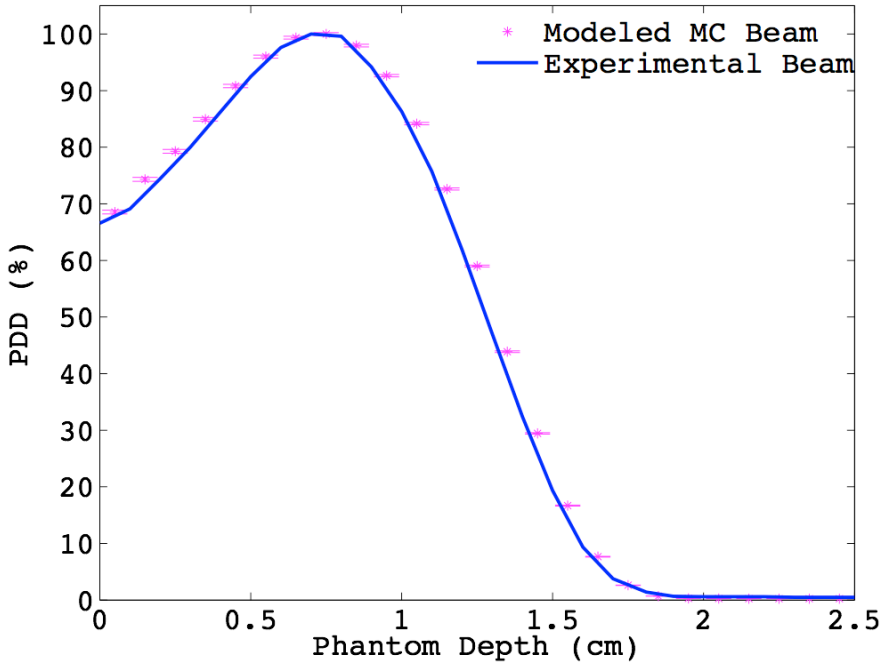

Figure 4.20: Verification of 4 MeV beam tuning. Both data sets are normalized to their respective D_{max}.

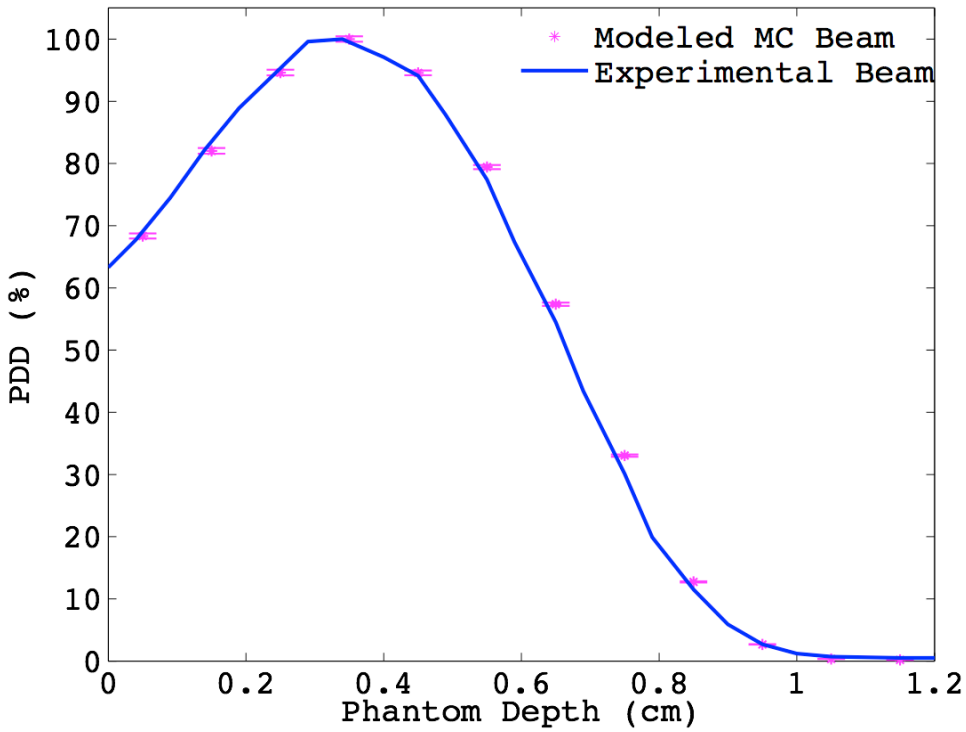

Figure 4.21: Verification of 2.5 MeV beam tuning. Both data sets are normalized to their respective D_{max}.

4.3.2 Beam Measurements

Moving the carbon targets into the beam-line and collecting PDD data, produced the results shown below.

Figure 4.22 shows the verification of 30% R_{CSDA} at 4 MeV. A maximum difference of 3.5% between the MC and experimental data was found. The mismatch, again, occurs primarily at the build-up and falloff regions.

The verification of 60 $R_{\%CSDA}$ at 4 MeV is shown in Figure 4.23. The two curves were found to vary by ±3%. However, the bremsstrahlung tail differs by 2.5% dose. The verification of the 4 MeV carbon beams proved that these experimental beams are achievable in practice.

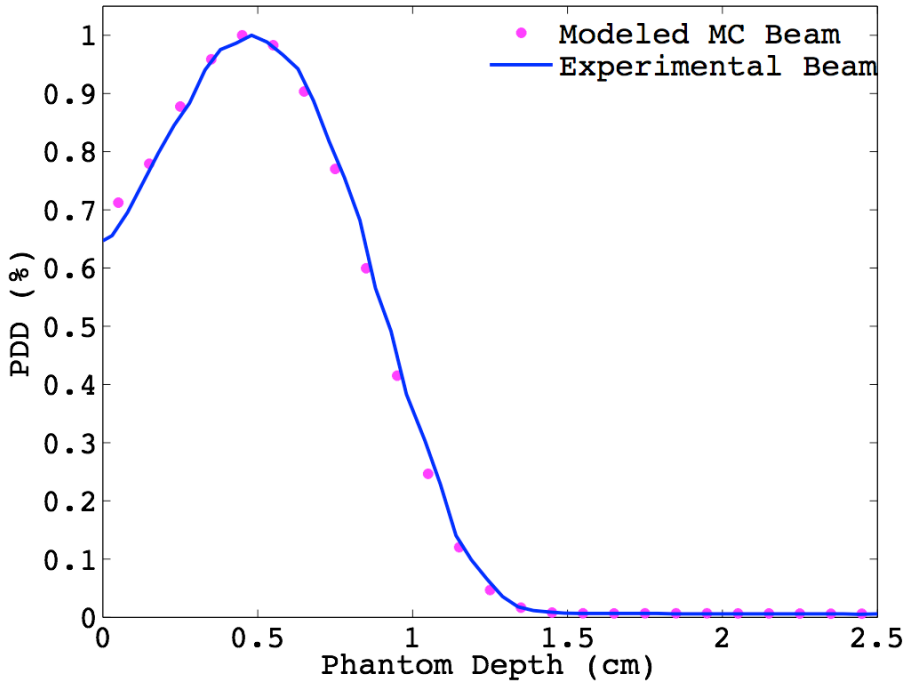

Figure 4.22: Verification of 30% R_{CSDA} at 4 MeV. Both data sets are normalized to their respective D_{max}.

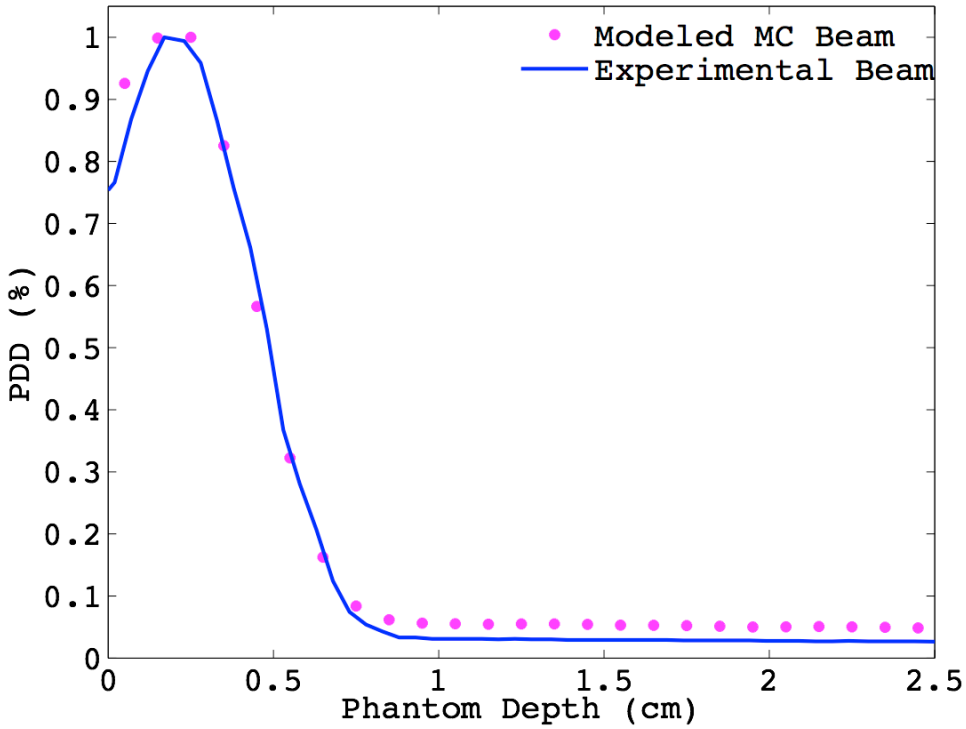

Figure 4.23: Verification of 60 $R_{\%CSDA}$ at 4 MeV. Both data sets are normalized to their respective D_{max}.

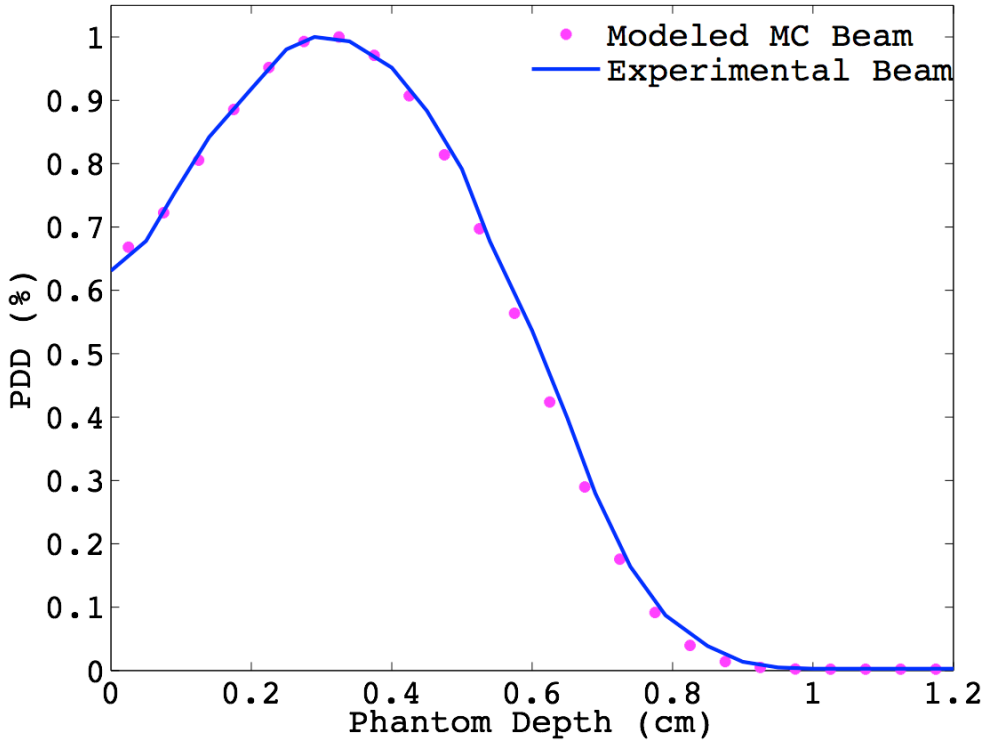

Figure 4.24: Verification of 15 $R_{\%CSDA}$ at 2.5 MeV. Both data sets are normalized to their respective D_{max}.

The verification of 15 $R_{\%CSDA}$ at 2.5 MeV is shown in Figure 4.24. The falloff region varies by 4.5% at the worst point, though the build up region is within ±1%. The bremsstrahlung tail differs by 0.08%

Figure 4.25 shows the verification of 30 $R_{\%CSDA}$ at 2.5 MeV. Again, the curves show good agreement. The build up region has a maximum difference of 3%, d_{max} agrees well with a difference of ±0.5%, the falloff region shows the most variation with a max of 5.6%, and the bremsstrahlung tail differs by 0.06%.

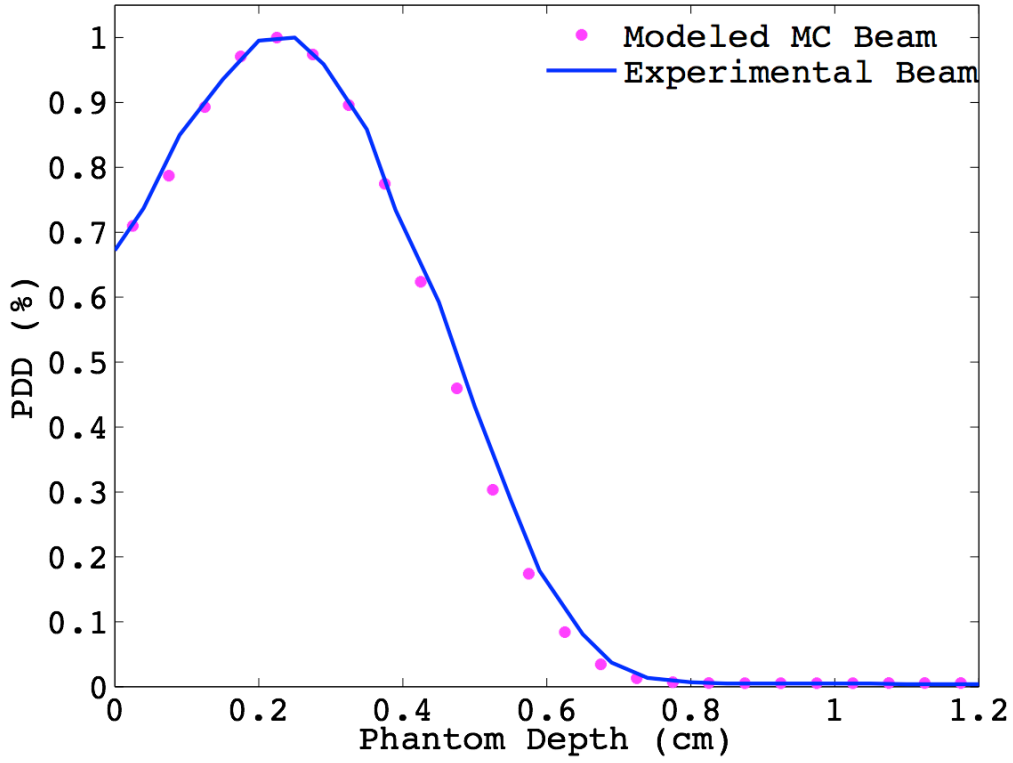

Figure 4.25: Verification of 30 $R_{\%CSDA}$ at 2.5 MeV. Both data sets are normalized to their respective D_{max}.

The verification of 60 $R_{\%CSDA}$ at 2.5 MeV is displayed in Figure 4.26. The build-up region varies by ~2%, the falloff region varies by ±3%, and the bremsstrahlung tail has a

consistent difference of 4%. The disagreement of the bremsstrahlung tails follows the same pattern as the 60 $R_{\%CSDA}$ at 4 MeV PDD.

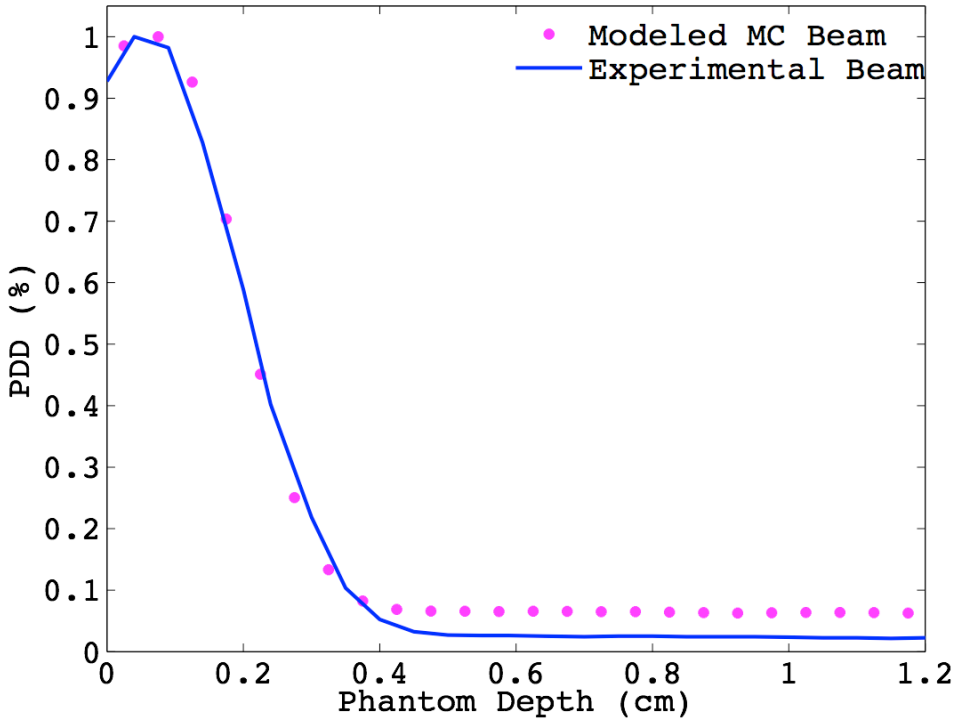

Figure 4.26: Verification of 60 $R_{\%CSDA}$ at 2.5 MeV. Both data sets are normalized to their respective D_{max}.

The verification of the 2.5 MeV carbon beams proved that these experimental beams are achievable in practice. However, there appears to be a discrepancy between the bremsstrahlung tails of the MC and experimental PDDs. The MC PDD was broken down into its photon and electron components (see Figure 4.27) and compared with the experimental data. It was found that the bremsstrahlung tail in the MC data was a match to the photon component of the collected phase-space. The photons were also found to supplement the build-up and falloff regions since the electron PDD did not converge with the full particle PDD.

It is concluded that the difference in the bremsstrahlung tail between the MC and experimental data, must lie in the experimental setup or procedure. Beam tuning is not precise, which affects the agreement of the electron component, and the detector used may not have been adequate for detecting very low energy photon beam (<200 keV). There is a known over response to low energy photons (< 150 keV) in silicon diodes, due to increasing photoelectric interactions. Although, the 60% R_{CSDA} plots show the experimental bremsstrahlung tail to be lower than the MC predicted value. The exact cause of this is unknown and would need to be investigated thoroughly with sufficient measurement of the photon tail using multiple collection methods.

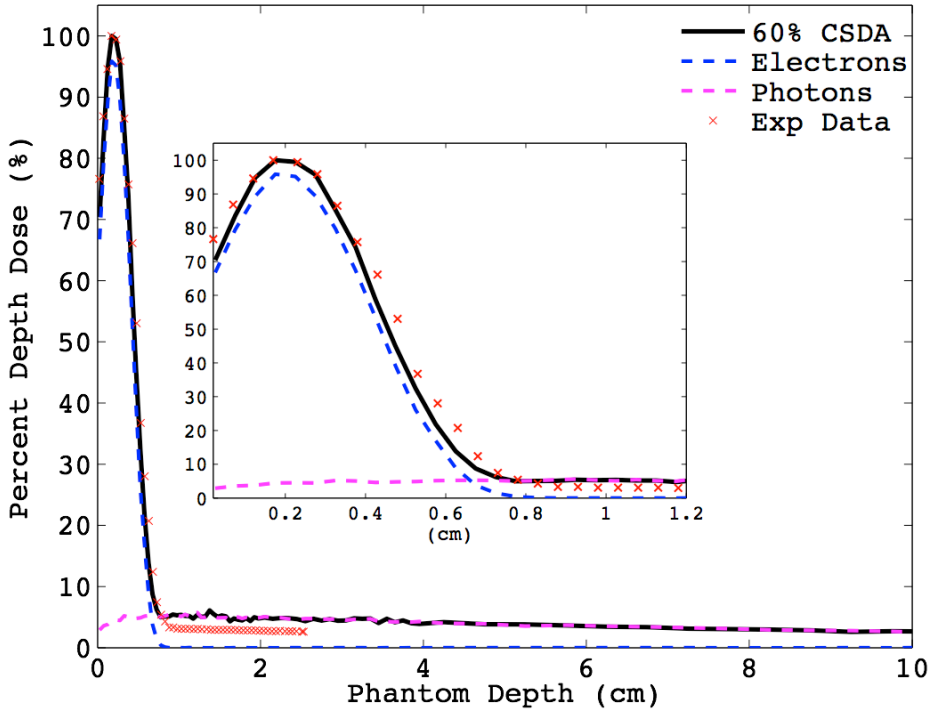

Figure 4.27: Overlay of electron (blue) and photon (magenta) PDDs of 60 $R_{\%CSDA}$ at 4 MeV onto the full particle PDD (black). The experimental data is included for comparison (red). The insert shows a close up of the first 1.2 cm depth.

CHAPTER 5 CONCLUSIONS

5.1 SUMMARY OF WORK

5.1.1 Monte Carlo Simulations

This work has shown, through Monte Carlo simulation, that carbon is the material of choice most suited for manufacturing a low-Z target for radiation therapy applications with the intent of enhancing surface dose. Among the four materials investigated, fluence spectra show that carbon and beryllium have the highest relative low energy electron fluence of the materials investigated. Beryllium isn't an optimal target to work with due to its expense, low neutron activation energy, and machining issues due to its carcinogenic nature. Through analysis of PDD curves for each material, it was discovered that for all four elements, the targets manufactured at 15% and 30% R_{CSDA} thickness, produced beams of similar properties; and all beams had comparable d_{max} for 60% R_{CSDA} thickness. However, aluminum and copper exhibited significant bremsstrahlung photon production at 60% R_{CSDA} with 20% and 80% contributions, respectively. For all the above reasons, beryllium, aluminum, and copper were eliminated for consideration as a low-Z therapy target material.

Using MC simulations, it was found through a combination of low-Z carbon beams and a therapeutic 6 MV beam, that we could tailor the surface dose and place the maximum dose at any depth from surface to d_{max}. This can be accomplished without

the aid of any external modifier placed within the beam path. These beams possess the versatility suitable to be used for surface dose enhancement.

5.1.2 Beam Tuning

Through this work, it was shown that a Varian 2100C linac could be detuned to produce beams close to 4 and 2.5 MeV, with the aid of a modified BMAG board. Placing manufactured carbon targets matching those used in the original MC simulations into the linac, produced beams with similar characteristics as the simulated results. This included d_{max} location, bremsstrahlung contribution, and in some cases, surface dose. The tuning of the machine was performed to generate beams that match as closely as possible to simulation, though this is a tedious task and the energy may not have been set to be 100% congruent with the simulation. We were able to match the beams within 5% and 3% within the build-up and falloff regions for the 4 MeV and 2.5 MeV beams, respectively, the d_{max} positions were found to match 100%. The variations between the modeled and experimental data may be the result of this discrepancy, as well as errors within the experimental setup.

5.2 Future Work

This work represents the initial stages of a project aimed at introducing low-Z targets as a standard addition to future linear accelerator technology and for use in modern treatment planning systems. Much work remains before we see these targets introduced in the clinical setting. Below are suggestions for future work.

5.2.1 Patient Simulation

Some preliminary steps have been taken to simulate a patient treatment using the proposed carbon beams to enhance surface dose in a breast chest wall patient (Figure 5.1). The result would be compared to that achieved in the original treatment plan which would have used bolus. The carbon beams would have to be used *en face* as the tangential pair typically used to treat chest wall will not produce the desired results with these novel beams. The therapeutic beam will still be delivered in this manner to supplement the carbon beams.

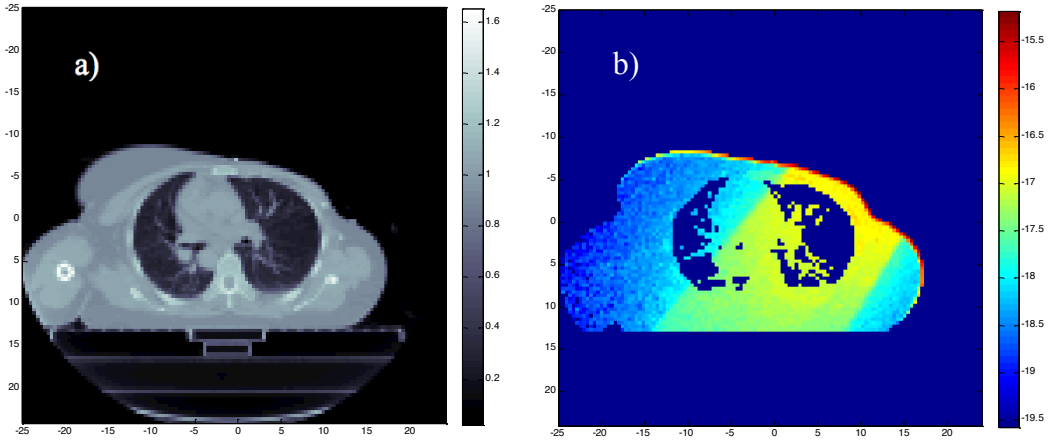

Figure 5.1: A) input of patient CT DICOM image into MATLAB. B) Simulated patient irradiated with 30% R_{CSDA} beam, log scaled. The color bar does not represent dose.

5.2.2 Simulation on TrueBeam System

Since this work is meant to be used with a system that has an in air target, these simulations should be repeated using a TrueBeam model, to determine any differences in the results when the target is ported over to the TrueBeam system. This program has

been validated and is a viable research tool. TrueBeam offers much to this research as it features a waveguide with a continuous energy switch, which allows electrons with a significantly reduced energy to exit the waveguide. TrueBeam machines are currently being produced with a 2.5 MV target slot to be used for cone beam imaging.

5.2.3 Development of Optimization Algorithm

Combination of the carbon beams with the 6 MV therapeutic beam was performed by hand in this work. They were not modelled on specific patient geometries, thus much work needs to be completed to automate this summation process and determine the effect on specific patient models which include inhomogeneties. For these beams to be clinically feasible, an algorithm must be developed which will determine the optimal beam configuration and combination for each patient and dose criteria.

5.2.4 Geometric Target Design

The targets used in this research were cylindrical discs but in clinical practice this setup will not be feasible. A target design must be made which allows minute adjustments in the target arm to bring a new target thickness into the beam-line. This may take the form of a slope, or step-function. Simulations will have to be done to determine whether having differing target thicknesses on either side of the incident beam will affect beam characteristics and outcome.

5.2.5 Integration with TrueBeam Hardware

Once simulations are completed with VirtuaLinac, targets should be placed into the TrueBeam target arm, and experimental scans taken of the beams. This will allow evaluation of the accuracy of the simulations. On the current generation of TrueBeam, minute positioning of the target arm cannot be controlled.

5.2.6 Integration of Low-Z Beams to Treatment Planning Software

To test treatment plans designed using the proposed carbon beams, an algorithm must be developed that integrates into the clinical treatment planning software. To do this the beams must be characterized, measured and calibrated to allow the program to use the beams and produce functional treatment plans.

BIBLIOGRAPHY

[1] S. Canada, "Canadian Cancer Statistics Special topic : Skin cancers," (2014).

[2] S. Levitt, J. Purdy, C. Perez, and S. Vijayakumar, *Technical basis of radiation therapy*, 4th ed. (Springer, Berlin, 2012).

[3] M. Nakano, R.F. Hill, M. Whitaker, J.H. Kim, and Z. Kuncic, "A study of surface dosimetry for breast cancer radiotherapy treatments using Gafchromic EBT2 film.," J. Appl. Clin. Med. Phys. **13**(3), 3727 (2012).

[4] L.J. Pierce *et al.*, "Postmastectomy Radiotherapy of the Chest Wall: Dosimetric Comparison of Common Techniques," **52**(5), 1220–1230 (2002).

[5] R.J. Kudchadker, J. A. Antolak, W.H. Morrison, P.F. Wong, and K.R. Hogstrom, "Utilization of custom electron bolus in head and neck radiotherapy.," J. Appl. Clin. Med. Phys. **4**(4), 321–33 (2003).

[6] E.E. Klein, M. Michalet-Lorenz, and M.E. Taylor, "Use of a Lucite beam spoiler for high-energy breast irradiation," Med. Dosim. **20**(2), 89–94 (1995).

[7] E. Lief, T. LoSasso, M. Hunt, L. Hong, and H. Amols, "XRT of large intact breasts using mixed energy beams and/or a beam spoiler," in *Proc. 22nd Annu. Int. Conf. IEEE Eng. Med. Biol. Soc. (Cat. No.00CH37143)*(Ieee, 2000), pp. 3257–3259.

[8] J.S. Li, S. McNeeley, K. Paskalev, M. Ding, W. Xiong, and C.M. Ma, "The Effect of Beam Spoiler for Breast Treatment - A Monte Carlo Study," in *Proc. AAPM 45th Annu. Meet.*(San Diego, CA, 2003), p. 1513.

[9] J. Li, L. Jin, W. Xiong, and C.M. Ma, "SU-FF-T-276: Is It Still Necessary to Use a Beam Spoiler for Breast Radiation?," Med. Phys. **34**(6), 2465 (2007).

[10] R. Manger, A. Paxton, and L. Cervino, “SU-E-T-437: Dosimetric Assessment of Brass Mesh Bolus for Postmastectomy Chest Wall Irradiation,” Med. Phys. **41**(6), 326–326 (2014).

[11] E. Healy *et al.*, “Skin dose effects of postmastectomy chest wall radiation therapy using brass mesh as an alternative to tissue equivalent bolus.,” Pract. Radiat. Oncol. **3**(2), e45–53 (2013).

[12] S. Utsunomiya, O.L. Pechenaya Green, and E. Klein, “SU-GG-T-337 Surface-Dose Enhancement Characteristics of Brass Mesh for Breast Cancer Treatments,” in *Proc. AAPM 52nd Annu. Meet.*(Philadelphia, PA, 2010), p. 3263.

[13] J. Benoit, A.F. Pruitt, and D.E. Thrall, “Effect of Wetness Level on the Suitability of Wet Gauze As a Substitute for Superflab ® As a Bolus Material for Use With 6 Mv Photons,” Vet. Radiol. Ultrasound **50**(5), 555–559 (2009).

[14] V. Vyas *et al.*, “On bolus for megavoltage photon and electron radiation therapy.,” Med. Dosim. 1–6 (2013).

[15] S.H. Hsu, P.L. Roberson, Y. Chen, R.B. Marsh, L.J. Pierce, and J.M. Moran, “Assessment of skin dose for breast chest wall radiotherapy as a function of bolus material.,” Phys. Med. Biol. **53**(10), 2593–606 (2008).

[16] S.W. Hadley, R. Kelly, and K. Lam, “Effects of immobilization mask material on surface dose,” J. Appl. Clin. Med. Phys. **6**(1), 1–7 (2005).

[17] Y. Khan *et al.*, “Clinical and Dosimetric Implications of Air Gaps between Bolus and Skin Surface during Radiation Therapy,” **2013**(September), 1251–1255 (2013).

[18] M. Sroka, J. Reguła, and W. Łobodziec, “The influence of the bolus-surface distance on the dose distribution in the build-up region,” Reports Pract. Oncol. … 161–164 (2010).

[19] Y. Khan *et al.*, “Clinical and Dosimetric Implications of Air Gaps between Bolus and Skin Surface during Radiation Therapy,” J. Cancer Ther. **2013**(September), 1251–1255 (2013).

[20] B.G. Clarke, “Report from the Ontario Radiation Incident and Safety Committee (RISC),” InterACTIONS **59**(3), 81–85 (2013).

[21] J.L. Robar, “Generation and modelling of megavoltage photon beams for contrast-enhanced radiation therapy.,” Phys. Med. Biol. **51**(21), 5487–504 (2006).

[22] J.L. Robar, S.A. Riccio, and M.A. Martin, “Tumour dose enhancement using modified megavoltage photon beams and contrast media,” Phys. Med. Biol. **47**(14), 2433–2449 (2002).

[23] E.J. Orton and J.L. Robar, “Megavoltage image contrast with low-atomic number target materials and amorphous silicon electronic portal imagers.,” Phys. Med. Biol. **54**(5), 1275–89 (2009).

[24] Varian Medical Systems Inc., *TrueBeam 1.6 Administration* (2012).

[25] O.Z. Ostapiak, P.F. O’Brien, and B.A. Faddegon, “Megavoltage imaging with low Z targets: implementation and characterization of an investigational system.,” Med. Phys. **25**(10), 1910–8 (1998).

[26] A. Tsechanski, A.F. Bielajew, S. Faermann, and Y. Krutman, “A thin target approach for portal imaging in medical accelerators.,” Phys. Med. Biol. **43**(8), 2221–36 (1998).

[27] D. Parsons and J.L. Robar, “Beam generation and planar imaging at energies below 2.40 MeV with carbon and aluminum linear accelerator targets.,” Med. Phys. **39**(7), 4568–78 (2012).

[28] F.H. Attix, *Introduction to Radiological Physics and Radiation Dosimetry* (John Wiley & Sons Inc., New York, New York, 1986).

[29] E.B. Podgorsak and K. Kainz, *Radiation Oncology Physics: A Handbook for Teachers and Students* (International Atomic Energy Agency, Vienna, Austria, 2006).

[30] M.J. Berger, J.S. Coursey, and M.A. Zucker, *Stopping-power and range tables for electrons, protons, and helium ions*, Natl. Inst. Stand. Technol. (2000).

[31] E. Podgorsak, *Radiation physics for the medical physicist* (2005).

[32] C.J. Karzmark and R.J. Morton, *A Primer on Theory and Operation of Linear Accelerators in Radiation Therapy* (Medical Physics Publishing, 1997).

[33] I. Kawrakow, E. Mainegra-Hing, D.W.O. Rogers, F. Tessier, and B.R.B. Walters, *The EGSnrc code system: Monte Carlo simulation of electron and photon transport NRCC Report PIRS-701* (Ottawa, 2011).

[34] D. Rogers, B. Walters, and I. Kawrakow, “BEAMnrc users manual,” NRC Rep. PIRS (2013).

[35] B. Walters, I. Kawrakow, and D. Rogers, “DOSXYZnrc users manual,” NRC Rep. PIRS (2013).

[36] D.W.O. Rogers, “Fifty years of Monte Carlo simulations for medical physics.,” Phys. Med. Biol. **51**(13), R287–301 (2006).

[37] C.M. Ma and D.W.O. Rogers, *BEAMdp users manual NRCC Report PIRS-0509* (Ottawa, 2009).

[38] D.W.O. Rogers, “BEAM: A Monte Carlo code to simulate radiotherapy treatment units,” Med. Phys. **22**(5), 503 (1995).

[39] B.R.B. Walters, I. Kawrakow, and D.W.O. Rogers, “History by history statistical estimators in the BEAM code system,” Med. Phys. **29**(12), 2745 (2002).

APPENDIX

December 1st, 2014

InterACTIONS, The Canadian Medical Physics Newsletter
COMP/CCPM Office
P.O. Box 72024
Kanato North RPO
Ottawa, ON
K2K 2P4
Canada

I am preparing my masters thesis for submission to the Faculty of Graduate Studies at Dalhousie University, Halifax, Nova Scotia, Canada. I am seeking your permission to include a figure from the following paper within a chapter of the thesis:

Brenda G. Clark, "Report from the Ontario Radiation Incident and Safety Committee (RISC)", InterACTIONS, **59**(3), 81, 84, 93 (2013).

Canadian graduate theses are reproduced by the Library and Archives of Canada (formerly National Library of Canada) through a non-exclusive, world-wide license to reproduce, loan, distribute, or sell theses. I am also seeking your permission for the material described above to be reproduced and distributed by the LAC(NLC). Further details about the LAC(NLC) thesis program are available on the LAC(NLC) website (www.nlc-bnc.ca).

Full publication details and a copy of this permission letter will be included in the thesis.

Yours sincerely,

Cathryn A. M. Parsons

Permission is granted for:

a) the inclusion of the material described above in your thesis.

b) for the material described above to be included in the copy of your thesis that is sent to the Library and Archives of Canada (formerly National Library of Canada) for reproduction and distribution.

Name: Christopher G. Thomas Title: Editor, InterACTIONS

Signature: _____ Date: December 1st, 2014

December 1st, 2014

James Robar,
Dalhousie University,
5820 University Ave
Halifax, NS, B3H 1V7
Canada

I am preparing my masters thesis for submission to the Faculty of Graduate Studies at Dalhousie University, Halifax, Nova Scotia, Canada. I am seeking your permission to include a figure from the following papers within a chapter of the thesis:

J.L. Robar, "Generation and modelling of megavoltage photon beams for contrast-enhanced radiation therapy.," Phys. Med. Biol. **51**(21), 5487–504 (2006).

D. Parsons and J.L. Robar, "Beam generation and planar imaging at energies below 2.40 MeV with carbon and aluminum linear accelerator targets.," Med. Phys. **39**(7), 4568–78 (2012).

E.J. Orton and J.L. Robar, "Megavoltage image contrast with low-atomic number target materials and amorphous silicon electronic portal imagers.," Phys. Med. Biol. **54**(5), 1275–89 (2009).

Canadian graduate theses are reproduced by the Library and Archives of Canada (formerly National Library of Canada) through a non-exclusive, world-wide license to reproduce, loan, distribute, or sell theses. I am also seeking your permission for the material described above to be reproduced and distributed by the LAC(NLC). Further details about the LAC(NLC) thesis program are available on the LAC(NLC) website (www.nlc-bnc.ca).

Full publication details and a copy of this permission letter will be included in the thesis.

Yours sincerely,

Cathryn A. M. Parsons

Permission is granted for:

a) the inclusion of the material described above in your thesis.

b) for the material described above to be included in the copy of your thesis that is sent to the Library and Archives of Canada (formerly National Library of Canada) for reproduction and distribution.

Name: James Robar, PhD Title: _____

Signature: _____ Date: December 1st, 2014